

Electrical interaction between
atmospheric volcanic ash and aircraft
in flight: mechanisms and application
for hazard detection.

Bryce Andrew Malton, BSc Hons.

This thesis is submitted in fulfillment of the requirements for the MSc. by
Research degree in Environmental Science at the University of
Lancaster.

January 2015

Electrical interaction between atmospheric volcanic ash and aircraft inflight: mechanisms and application

Bryce Andrew Malton, BSc Hons.

This thesis is submitted in fulfillment of the requirements for the MSc. by Research degree in Environmental Science at the University of Lancaster

January 2015

Abstract

The charging of aircraft surfaces in flight by ice and other particulates has been studied since the 1940's, and volcanic ash suspended within dispersed plumes has been a hazard to aviation since the advent of commercial jet airliners in the 1960s. This study examines the interaction of volcanic ash particles with metallic surfaces likely to be found on an aircraft, and its ability to charge those surfaces by impact. We do this by directing a high-pressure jet of mixed air and volcanic ash, sieved to $<63 \mu\text{m}$ dia., at fixed 50 mm x 50 mm target. The charging is quantified as the charge generated on the target surface per unit mass of particulate impacted. By testing volcanic ash alongside a control material (Ballotini™) which is not expected to fracture the study provides evidence that fracto-emission is the dominant charging process. It is demonstrated that volcanic ash impacting a metallic target at mass delivery rates of approximately 5 mg s^{-1} can generate charge to mass ratios of 0.5 to 0.8 C kg^{-1} at impact speeds in the range of 60 to 70 ms^{-1} . It is also found that the charging behaviour is non-linear with respect to velocity of impact and that charging behaviour varies dependant upon the materials of the particle and the impacting surface. The study includes the investigation of two types of volcanic ash, sand and some qualitative work to investigate the impact of ice on the targets. From this we conclude that the measurement of particulate mass concentration is possible, and discrimination of particulate type is possible by exposing multiple target materials in parallel. We therefore hypothesise that the observed behaviours could form the basis for an on-board volcanic ash detection sensor system for pilot warning and guidance.

Keywords;

Volcanic ash, fracto-emission, charging, particles, aircraft.

Table of Contents

Abstract	2
Table of Contents	4
Table of Figures	8
Table of Tables.....	16
Preface	18
Declaration	18
1 Introduction.....	19
2 Method.....	33
2.1 Principle of the Experimental Setup.....	33
2.2 Experimental Equipment.....	34
2.2.1 The High Pressure Air Supply	34
2.2.2 The Particulate Sample Feed System.....	37
2.2.3 The metallic target.....	41
2.2.4 The electrical signal sensing system.....	42
2.2.5 The target enclosure and equipment mountings.....	43
2.2.6 The earthing and shielding system.....	44
2.2.7 The ice cloud generation box.....	46
2.3 Experimental Procedure.....	47
2.4 Data post processing.....	51
2.5 Airflow Speed Calibration.....	53
2.5.1 Output processing, limits of sensor performance and calibration.....	55

2.6	Sample feeder draw-wire system calibration.	57
3	Results.....	58
3.1	Airflow Velocity Calibration	59
3.1.1	Accuracy of the sensor.....	59
3.1.2	Measured pressures at the target face.....	60
3.1.3	Converting the target face pressures to airflow velocity.....	61
3.1.4	The airflow velocity distribution across the target.....	63
3.2	Sample feeder draw-wire system speed calibration, and mass delivery system accuracy.	65
3.3	Charge to mass ratio of Eyjafjallajökull ash impacting the metallic targets at varying velocity (Q_{Mv}).....	65
3.4	Charge to mass ratio of Eyjafjallajökull ash impacting the aluminium target (Q_{Mc}) at constant velocity of 61 ms^{-1} (50Psi high-speed flow pressure) – experimental controls.....	68
3.4.1	Applying the control data to the results shown in 3.3.....	69
3.5	Charge to mass ratio of Eyjafjallajökull ash impacting the metallic targets at constant velocity but varying mass rates (Q_{Mr}).....	73
3.6	Charge to mass ratio of Eyjafjallajökull ash leaving the side feeder tube at varying velocities (Q_{Mf}).....	76
3.7	Charge to mass ratio of Ballotini™, sand, and Sakurajima ash impacting the metallic targets at varying velocity (Q_{Mv}).	80
3.8	The impact of ice on an aluminium target.....	82
3.9	The particulate grain size distribution	85
4	Discussion	87
4.1.1	The products of the impact.....	92

4.1.2	The effect of the material pairing.....	92
4.1.3	The effect of velocity of impact.....	93
4.1.4	The effect of particle surface charge limits.....	94
4.2	The particle lofting and high-speed flow transport.....	97
4.3	The impact at the target face.....	100
4.4	The analysis of the impact of ice.....	104
5	Conclusions and suggestions for further work.....	106
6	Appendix.....	110
A.	Revision 1 high-pressure air nozzle parts, assembly and description.....	110
B.	Revision 2 high-pressure air nozzle parts, assembly and description.....	113
C.	Revision 3 high-pressure air nozzle parts, assembly and description.....	117
D.	Revision 4 high pressure air upper nozzle parts.....	119
E.	Revision 2 side feeder tube assembly – sample cartridge detail.....	121
F.	Revision 2 side feeder tube assembly – feeder tube detail.....	123
G.	Revision 2 side feeder tube assembly – draw wire system.....	125
H.	Revision 1 Wiring and Earthing Diagram.....	126
I.	Revision 2 wiring and earthing diagram.....	127
J.	Revision 1 target enclosure detail.....	128
K.	Revision 2 target enclosure detail.....	129
L.	Table of pressure sensor outputs with corresponding inlet pressure expressed as airspeed, calculated from the manufacturer transform function (Freescale Semiconductor, 2012).....	130
M.	Results of the timed calibration tests of the sample draw-wire system.....	132

N. Theoretical maximum charge held per mg of particulate.....	137
O. The modelled effect on maximum charge capacity of a mixed grain size particulate.....	140
7 References	142

Table of Figures

Figure 1 - Diagram of the damage mechanisms to a jet engine due to volcanic ash ingestion – image courtesy of J. Renvier, SVP System Engineering, Snecma (Renvier, 2010).	20
Figure 2 - Erosion to the leading edges of turbine blades from the NASA DC8 engine (Grindle et al., 2003).	20
Figure 3 - Melted and re-solidified ash deposit in the combustion exit of the engines of BA009 - photo courtesy of Eric Moody as shown in Dillow (2010).....	20
Figure 4 - Blocked cooling holes and blistered turbine aerofoil surfaces due to overheating (Grindle et al., 2003).....	21
Figure 5 - VA deposited on an air conditioning heat exchanger filter from the NASA DC8 - magnification x150 (Grindle et al., 2003).	21
Figure 6 - A photograph of an ash plume from Mt. Etna mixing with local mid-level cloud – arrow indicates plume layer (Malton, 2013).....	23
Figure 7 - General arrangement of the F35 JSF gas path monitoring system, after Powrie and Novis (2006) (IDMS - Ingested Debris Monitoring System; EDMS - Exhaust Debris Monitoring System; SCU - Signal Conditioner Unit; 3BSM – 3 Bearing Swivel Module; STOVL - Short Take-Off and Vertical Landing; CTOL - Conventional Take-Off and Landing; CV – Carrier Variant).....	27
Figure 8 – A scanning electron microscope image of ash from Mount Redoubt eruption of 2009 (Izbekov and Shipman, 2009).	31
Figure 9 - A scanning electron microscope image of ash from the Eyjafjalljökull eruption of 2010 (Gislason et al., 2011).	31
Figure 10 - An overview of the evolved test equipment configuration with the main components arrowed.....	35
Figure 11 - General arrangement of the revision 3 high pressure air nozzle showing predicted air entrainment path.	36
Figure 12 - The final revision 5 high-pressure nozzle.	37

Figure 13 - General overview of the revision 2 sample feeder system with the wall of the side feeder tube removed at the lofting point to show the cartridge crossing.	38
Figure 14 - Detail of volcanic ash particulate sample loaded into a cartridge.	39
Figure 15 - Overview of the side feeder tube with sample cartridge installed - Note the feeder tube wall has been removed to expose the cartridge in place.	39
Figure 16 - Detail cutaway view of the sample cartridge inner passing through the side feeder tube - note the tube wall has been removed to show the cartridge in place.....	39
Figure 17 - Overview of the draw-wire mechanism in place and connected to the sample cartridge (at rear of photo).....	40
Figure 18 - The side feeder tube inlet filters.....	41
Figure 19 - Revision 5 side feeder tube assembly mounted in the base of the target enclosure.....	41
Figure 20 - An example target.....	42
Figure 21 - An overview of the test equipment with the shielding box complete.....	45
Figure 22 - An overview of the test equipment with the front panel removed and the extraction hose fitted.	45
Figure 23 - Overview of the ice cloud generation compartment.....	46
Figure 24. - The ice cloud generation compartment installed on the target enclosure frame.	46
Figure 25 - An internal view of the ice cloud box showing the gauze dry ice trays. ...	46
Figure 26 – Scanning electron microscope image of Ballotini TM - image courtesy of The Univeristy of Aukland (2014).....	48
Figure 27 – Scanning electron microscope of 150 μ m Ballotini TM image retrieved from Campo-Deano et al. (2012).	48

Figure 28 - An example of an unsmoothed signal and the same signal smoothed using 35-point box centre point algorithm.	51
Figure 29 - An example of data selection for processing. The signal area is considered stable sample delivery conditions and the zero signal area is used for offset adjustments.	52
Figure 30 - PSG Associates relative pressure sensor PCB installed in enclosure.	53
Figure 31 - The airspeed calibration target showing the drill pattern to accept the pitot probe.	54
Figure 32 - The pitot probe and calibration target installed in the test enclosure.	54
Figure 33 - A detail view of the pitot probe installed and projecting through the target.	54
Figure 34 - Comparison between the theoretical output of the PSG airspeed sensor as calculated by the transfer function (Freescale Semiconductor, 2012) and the actual output as tested using a pitot / static test set.	59
Figure 35 - A sample output signal from the PSG pressure sensor during an airspeed calibration test. The recording has been smoothed to remove high frequency noise.	60
Figure 36 - Histogram of the recorded data from the PSG pressure sensor showing the data spread at three high pressure air supply values. Data points are binned at 0.011V intervals; each dataset has 45 bins and 9000 data points. The data sets were collected at 40, 55 and 70 psig,	61
Figure 37 - Calibration curves for airflow velocity vs. high-pressure air supply pressure.	62
Figure 38 - Airflow velocity contour on the target face (High-speed flow pressure 40psig) overlain on an image of the aluminium target. The erosion zone of the target can be seen as a darker central area.	64
Figure 39 - Airflow velocity contour on the target face (High-speed flow pressure 70psig) overlain on an image of the aluminium target. The erosion zone of the target can be seen as a darker central area.	64

Figure 40 – Graph of cartridge pull distance vs. time for the sample drawer wire drive system at various motor drive voltages.	65
Figure 41 - The charge to mass ratio for E15 ash impacting an aluminium target (Q_{MvAl}) at varying velocities. The “best fit” curve is shown dashed.	66
Figure 42 - The charge to mass ratio for E15 ash impacting a Brass target (Q_{MvBr}) at varying velocities. The “best fit” curve is shown dashed	67
Figure 43 - The charge to mass ratio for E15 ash impacting a stainless steel target (Q_{MvSS}) at varying velocities. The “best fit” curve is shown dashed – NOTE that two points considered as outliers from experimental notes have been excluded from the best fit and are shown.	67
Figure 44 – Charge to Mass ratio (Q_{Mc}) of the 28 control tests, sorted by day number of the test sequence. The mean value is shown as a dotted line.	68
Figure 45 - The variation from the mean of the control test values of Charge to mass ratio Q_{Mv} , grouped by capture period.	69
Figure 46 - The charge to mass ratio for E15 ash impacting an aluminium target (Q_{MvAl}) with data points adjusted for control variation (error bars not shown for clarity).	71
Figure 47 - The charge to mass ratio for E15 ash impacting a brass target (Q_{MvBr}) with data points adjusted for control variation (error bars not shown for clarity).	71
Figure 48 - The charge to mass ratio for E15 ash impacting a stainless steel target (Q_{MvSS}) with data points adjusted for control variation (error bars not shown for clarity).	72
Figure 49 - The charge to mass ratio for E15 ash impacting an aluminium target (Q_{MrAl}) at varying mass delivery rates. The “best fit” curve is shown dashed.	73
Figure 50 - The charge to mass ratio for E15 ash impacting a brass target (Q_{MrBr}) at varying mass delivery rates. The “best fit” curve is shown dashed.	74
Figure 51 - The charge to mass ratio for E15 ash impacting a stainless steel target (Q_{MrSS}) at varying mass delivery rates. The “best fit” curve is shown dashed.	74

Figure 52 - The charge to mass ratio for E15 ash impacting an aluminium target at varying mass delivery rates (Q_{MrAl}) with data points adjusted for control variation (error bars not shown for clarity).	75
Figure 53 - The charge to mass ratio for E15 ash impacting a brass target at varying mass delivery rates (Q_{MrBr}) with data points adjusted for control variation (error bars not shown for clarity).	75
Figure 54 - The charge to mass ratio for E15 ash impacting a stainless steel target at varying mass delivery rates (Q_{MrSS}) with data points adjusted for control variation (error bars not shown for clarity).	76
Figure 55 - Charge to mass ratio results for the side feeder during the E15 / Aluminium target experimental group. The results are aligned by the high-speed airflow velocity value. The feed tube velocity is unknown and therefore no x-axis error is shown. The target Q_{MvAl} best fit curve is shown for reference.	77
Figure 56 - Charge to mass ratio results for the side feeder during the E15 / Brass target experimental group. The results are aligned by the high-speed airflow velocity value. The feed tube velocity is unknown and therefore no x-axis error is shown. The target Q_{MvBr} best fit curve is shown for reference.	78
Figure 57 - Charge to mass ratio results for the side feeder during the E15 / Stainless steel target experimental group. The results are aligned by the high-speed airflow velocity value. The feed tube velocity is unknown and therefore no x-axis error is shown. The target Q_{MvSS} best fit curve is shown for reference.	78
Figure 58 - Comparison of the best-fit curves of charge to mass ratio (Q_{MvAlf} , Q_{MvBrf} and Q_{MvSSf}) vs high speed airflow velocity.	79
Figure 59 – The charge to mass ratio Q_{Mv} for Ballotini™, Sand and SAK ash impacting targets – error bars omitted for clarity.	80
Figure 60 - Signal current traces for E15 ash, sand, and SAK ash impacting the aluminium target at 61.1 m s^{-1} (50 psig high-speed airflow pressure).	81
Figure 61 - The charge current signal for ice impacting an aluminium target – run #1.	82

Figure 62 - The charge current signal for ice impacting an aluminium target – run #2.	82
Figure 63 - The charge current signal for ice impacting an aluminium target – run #3.	82
Figure 64 - The charge current signal for ice impacting an aluminium target – run #4.	82
Figure 65 - The charge current signal for ice impacting an aluminium target – run #5.	83
Figure 66 - The charge current signal for ice impacting an aluminium target – run #6.	83
Figure 67 - The charge current signal for ice impacting an aluminium target – run #7.	83
Figure 68 - The charge current signal for ice impacting an aluminium target – run #8.	83
Figure 69 - View to the interior of the ice generation box taken from the water injection port after completion of tests.....	84
Figure 70 - View from above of the feeder tube impression in ice build up at the delivery end of the ice generation box.	84
Figure 71 - View of the interior of the ice generation box with the dry ice trays removed at the end of testing.....	85
Figure 72 - Grain size distribution for experimental particulates.	86
Figure 73 - Extract from John et al. (1980) showing anomalous charge values and polarity reversal for Sodium Chloride and Potassium biphthalate.....	88
Figure 74 – Cumulative experimental distributions of breakage probability of basalt particles versus normalized kinetic energy – image and text Aman et al. (2011).	94
Figure 75 - Calculated degree of broken bonds based on the model (array of curves left-hand side) and experimental determined kinetic energy, which is necessary	

to obtain a certain degree of broken bonds (array of curves right-hand side) after Froeschke et al. (2003).	94
Figure 76 - The effect of Reynolds number on turbulence behind a cylinder, image from Blevins (1977).	98
Figure 77 - An example of particle scavenging from the feeder cartridge. Evidence of scavenging from inside the cartridge is evident but the empty tube section is clean and bright.....	100
Figure 78 - The comparison of the adjusted best-fit line for the charge behaviour of E15 ash impacting the three metallic targets.	101
Figure 79 - Graph of charge held per grain size distribution band (C / band) pre and post breakage according to the suggested model.	103
Figure 80 - The comparison of the adjusted best-fit line for the charge behaviour of E15 ash impacting the three metallic targets at constant velocity but varying mass delivery rate.	103
Figure 81 - View of revision 1 nozzle assembly with feed cone in place.....	110
Figure 82 - View of revision 1 nozzle assembly from above with feed cone in place.	110
Figure 83 - View of the revision 1 jet pipe installation into the revision 1 target enclosure.....	110
Figure 84 - Revision 1 high-pressure air nozzle piece parts.	111
Figure 85 - Revision 1 high-pressure air nozzle general assembly.....	112
Figure 86 - A view of the revision 2 high-pressure nozzle arrangement.	113
Figure 87 - A view of the revision 2 high-speed nozzle arrangement with a prototype side feeder tube and cartridge installed.	113
Figure 88 - Revision 2 high-pressure nozzle piece parts.	114
Figure 89 - Revision 2 high-pressure air nozzle general assembly.....	115

Figure 90 - Revision 2 high-pressure air nozzle view from above showing the general arrangement of the side feeder tube installation.	116
Figure 91 - The revision 3 nozzle upper fitting.	117
Figure 92 - The revision 3 upper fitting with the mating entrainment shroud in place.	117
Figure 93 – Revision 3 high-pressure air nozzle upper section piece parts.	118
Figure 94 - View of the revision 4 high-pressure air nozzle with angled side feeder tube.	119
Figure 95 - The revision 4 high-speed airflow nozzle piece parts.	120
Figure 96 - Detail view of the sample cartridge inner and sleeve.	121
Figure 97 – Sample feed cartridge piece part drawing.	122
Figure 98 - View of a final revision 2 of particulate sample side feeder tube (Note angled cut off and plastic sleeve are later modifications).	123
Figure 99 - Revision 2 Side feeder tube detail drawing.	124
Figure 100 - The DC electric draw-wire motor with attached 50mm pulley.	125
Figure 101 – View showing the connection of the draw-wire to the particulate sample cartridge.	125
Figure 102 - The revision 1 enclosure and mounting frame (with revision 1 particle feed system in place).	128
Figure 103 - The revision 2 enclosure with square frustrum extraction contraction and honeycomb air inlet.	129
Figure 104 - View of the honeycomb inlet panel.	129

Table of Tables

Table 1 - The satellite systems and wavelength bands used for split window difference detection of VA (Malton, 2013).....	22
Table 2 - The matrix of target / particulate pairings, showing the number of individual runs per variable group.	49
Table 3 - Matrix of high-pressure air supply and cartridge drive ON and OFF timings.	50
Table 4 - Table of coefficients for the airspeed calibration curves shown in figure 37 and detailed in equation (1.5).....	62
Table 5 - The high-speed flow pressure setting / airflow speed calibrated results table. Mean airflow velocity is to 3 sf and errors are to 2 sf.	63
Table 6 - Coefficients of the Boltzman sigmoid equation best fit curves of QMv against airflow velocity shown in Figures 41 to 43 and Figures 46 to 48.....	72
Table 7 - Comparison of mean charge to mass values for Ballotini™ versus E15 ash for the tested airflow velocities.	81
Table 8 – Mean charge to mass values for particles impacting an aluminium target at 61 ms ⁻¹ , ordered by quantity.....	89
Table 9 - Mean charge to mass values for particles impacting an aluminium target at 66 ms ⁻¹ , ordered by quantity.....	89
Table 10 – The maximum theoretical charge per unit mass (C kg ⁻¹) that can be sustained under a range of surface charge limit assumptions.	95
Table 11 - Calculated maximum particle surface charges according to various theoretical surface charge limit assumptions.	96
Table 12 - Available Work function values for experimental materials – Note: the figure quoted for E15 ash is that of the closest equivalent known and that of the NASA JSC-1 Mars simulant.	99
Table 13 - Theoretical maximum charge per mg of dispersed E15 ash density 2800 kg m ⁻³	137

Table 14 - Theoretical maximum charge per mg of dispersed Sak ash with density 2800kgm ⁻³	138
Table 15 - Theoretical maximum charge per mg of dispersed Sand with density 2600 kg m ⁻³	139
Table 16 - A modelled example of the effect of breakage on the maximum charge capacity of a mixed grain size particulate. Data are for a particulate mass of 1 mg. The initial grain size distribution is as measured for E15 ash. The distribution after breakage has been based on reduced fraction above 10 µm dia. and increased <1 µm.....	140

Preface

I would like to acknowledge several people for their help and support during the period of this study. Firstly I would like to thank my supervisors, Dr Steve Lane and Dr Jennie Gilbert, for the ever open door, support and patience. Without them this would not be complete. Secondly I need to thank my wife Claire who has always been there to 'pick up the pieces' and support me when I thought things had gone terminally wrong. Thirdly I need to thank Phil Starbuck of PSG and Associates who very generously supplied me with dynamic pressures sensors, without which it would have been extremely difficult to characterize the airflow. Lastly I need to thank the various members of Lancaster Environment Centre who have helped me with equipment, training and materials.

Declaration

I declare that the work in this thesis was carried out in accordance with the regulations of Lancaster University. The work is original, except where indicated by special reference in the text, and no part of the thesis has been submitted for any other academic award. Any views expressed in the thesis are those of the author.

Signed: -----

Date:-----

1 Introduction

Since the inception of aviation the cornerstone method of avoiding hazards to flight, whether they be mountains or thunderstorms, has been 'see and avoid'. As aviation has developed and grown, so the hazards to flight have changed and expanded, and likewise the technologies to both see and avoid hazards have developed. Some of the hazards, such as high ground and buildings, are spatially fixed and can be easily understood and warned of by using GPS technology, however many are random and spatially and temporally variable, such as thunderstorms, ice loaded cloud or wind shear. On-board sensors such as lightning detection, weather radar and ice detection have increasingly been integrated into flight navigation systems to give pilots a single display of the hazards they face. Complex integrated sensor and data systems, such as the combined terrain avoidance and collision avoidance system T³CAS by ACSS (ACSS, 2014), are an example of the level of sophistication currently available, where on-board systems data, and data exchanged between aircraft, are synthesised to provide the hazard awareness and avoidance guidance to the flight crew.

It is self evident that any hazard must first be "seen" or detected, and one hazard that has so far been undetectable to on-board aircraft sensors is airborne dispersed volcanic ash (VA). Commercial jet aircraft have been encountering volcanic ash plumes since the early 1950's and the effects of these encounters are globally understood, to the point where the International Civil Aviation Organisation (ICAO) initiated the International Airways Volcano Watch (IAVW) and the Volcanic Ash Advisory Centres (VAAC) in 1987 and published an operational guidance manual, "Flight Safety and Volcanic Ash" (Doc 9974, ICAO 2012). The key effects, such as engine failure, system blockages and windshield damage, can critically endanger the safety of the aircraft and its occupants. VA can induce jet engine performance degradation, and eventual failure, in multiple ways (Figure 1): erosion of the close-tolerance aerofoils in the compressor and turbine section (Figure 2); blockage of the airflow path due to the melting and re-solidifying of volcanic glasses in the combustion area (Figure 3); and blockage of cooling passages in the engine (Figure 4). System blockages can affect a number of different flight functions: pitot / static systems which can result in the loss of airspeed information; avionics cooling systems which can result in the failure of navigation equipment; and air conditioning filter systems resulting in the loss of cabin pressure (Figure 5). Windshield damage

(erosion) caused by the abrasive nature of VA causes vision obstruction for the crew and can compromise the safe completion of the landing.

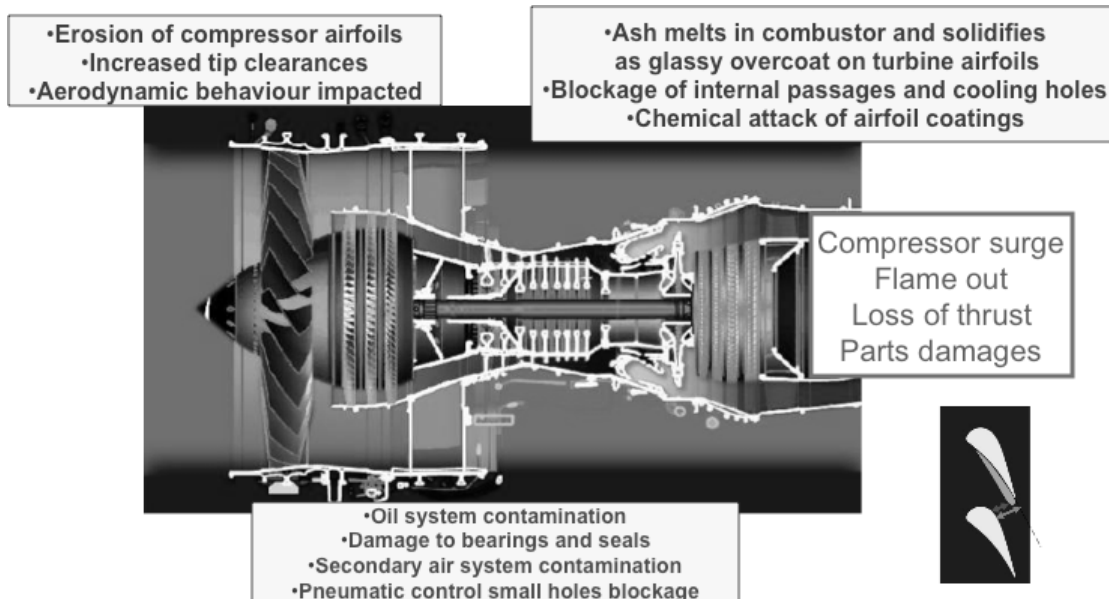


Figure 1 - Diagram of the damage mechanisms to a jet engine due to volcanic ash ingestion – image courtesy of J. Renvier, SVP System Engineering, Snecma (Renvier, 2010).

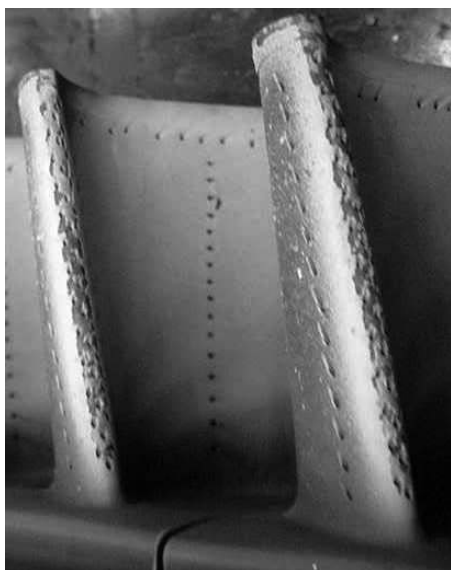


Figure 2 - Erosion to the leading edges of turbine blades from the NASA DC8 engine (Grindle et al., 2003).



Figure 3 - Melted and re-solidified ash deposit in the combustion exit of the engines of BA009 - photo courtesy of Eric Moody as shown in Dillow (2010).

Despite the initiation of the IAVW and the VAACs, whose responsibility it is to monitor, forecast, and disseminate eruption information to the aviation sector (that is, to be the ‘eyes’ of the flight crew), aircraft encounters with VA are on-going with a mean reported global encounter rate of 3 per year from 1980 to 2009 (Guffanti et al.,

2010). The encounter rate pre and post the initiation of the VAACs appears relatively constant (3.12 and 2.95 encounters per annum respectively). Indeed six of the nine most serious encounter events involving engine failures have occurred after the mechanisms to avoid encounters had been put in place (Guffanti et al., 2010). Two of those six encounters resulted in the failure of all engines where crashes were narrowly averted, such as KLM flight 867 (Neal et al., 1997), and a Gulfstream GII business jet (Guffanti et al., 2010).

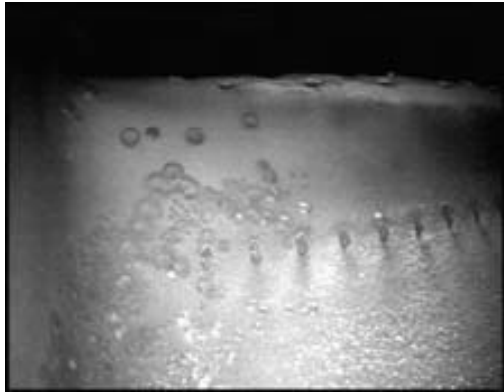


Figure 4 - Blocked cooling holes and blistered turbine aerofoil surfaces due to overheating (Grindle et al., 2003).

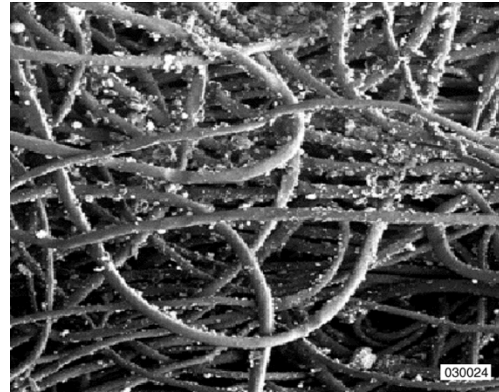


Figure 5 - VA deposited on an air conditioning heat exchanger filter from the NASA DC8 - magnification x150 (Grindle et al., 2003).

As the VAAC's role is to act as the 'eyes' of flight crews to alert them to hazardous airspace, then the technology used to detect the VA must be robust. The current hazard management methodology for VA depends largely upon satellite and Lidar (Light Detection and Ranging) remote sensing techniques, whereby VA plumes are remotely sensed and then designated as hazardous areas which flight crews avoid. Satellite techniques are based upon infrared wavelength weather satellites using data from two wavelength bands. This technique, known as the 'split window differencing technique', is based on the spectral bands shown in Table 1 (example satellite systems shown), and assumes that the result of the difference between T_4 and T_5 will be negative for volcanic ash and positive for water based clouds (Hufford et al., 1999). However, multiple studies have highlighted the limitations of current satellite detection of volcanic plumes (Pergola et al., 2004, Tupper et al., 2004, Prata, 2008, Simpson et al., 2000), the most critical reason being the obscuration caused by atmospheric water and ice clouds. Kite-Powell (2001) offer a comprehensive list of problems including:

- i. Coarse pixel size.
- ii. Low data frequency (from 30 mins. to hours).
- iii. High false alarm rate.
- iv. Plumes being obscured by clouds or moisture.
- v. Reduced availability of night imagery.
- vi. Limited ability to detect small events.

Table 1 - The satellite systems and wavelength bands used for split window difference detection of VA (Malton, 2013).

Satellite System	T ₄ Channel wavelength	T ₅ Channel wavelength
	μm	μm
Advanced Very High Resolution Radiometer (AVHRR)	10.3 – 11.3	11.5 – 12.5
Geostationary Operational Environmental Satellites (GOES)	10.2 – 11.2	11.5 – 12.5
Geostationary Meteorological Satellite (GMS)	10.5 – 11.5	11.5 – 12.5

Lidar techniques are either land based (for example the Raymetrics Raman Depolarisation Lidar (Raymetrics S. A., 2014)) or airborne platform based (for example the Facility for Airborne Atmospheric Measurements (FAAM) Differential Absorption Lidar (Robinson, 2007)). Recent work by Marengo et al. (2011) based upon data gathered by the FAAM lidar during the Eyjafjallajökull eruption quotes data errors may be a factor of two due to uncertainties in the post processing of the data.

None of the above solves the problem that the only method air crew have of detecting ash is visual, and this problem of visual detection was exacerbated by the introduction of arbitrary ash concentration limits for safe flight following the Eyjafjallajökull eruption of 2010. In the late stages of the Eyjafjallajökull event the European and North Atlantic office of the ICAO took the step of defining regulatory levels of atmospheric contamination by ash in accordance with the concentration of ash per unit volume in mg m^{-3} : (a) Low Contamination airspace represented by concentrations of up to 2 mg m^{-3} , (b) Medium Contamination by 2 mg m^{-3} to 4 mg m^{-3} and (c) High Contamination as above 4 mg m^{-3} (International Civil Aviation Organisation, 2010). This allowed flight into Low Contamination airspace at the operators' discretion, but maintained the ruling that flight into 'visible or discernable'

VA was prohibited. This now required the flight crew to make a visual assessment of whether any aerosol cloud was (a) volcanic ash or not and (b) whether it was likely to be above a certain mass concentration. The research of Weinzierl et al. (2012) investigated whether this discrimination was possible and the findings were that: “under clear-sky conditions, volcanic ash is visible at concentrations far below the limit for safe flying, but it is impossible to determine visually when the threshold of 2 mg m^{-3} is exceeded. Volcanic ash cannot be distinguished visually from other aerosol layers, such as mineral dust”, and also “regardless of concentration, volcanic ash is not visible at night.” These findings were exhibited to this author on a field trip to Etna in April 2013 when ash plumes observed to be ejected into the turbulent troposphere (approx. 3000 m) were mixed with local cloud and rapidly became indistinguishable from other aerosols (Figure 6).

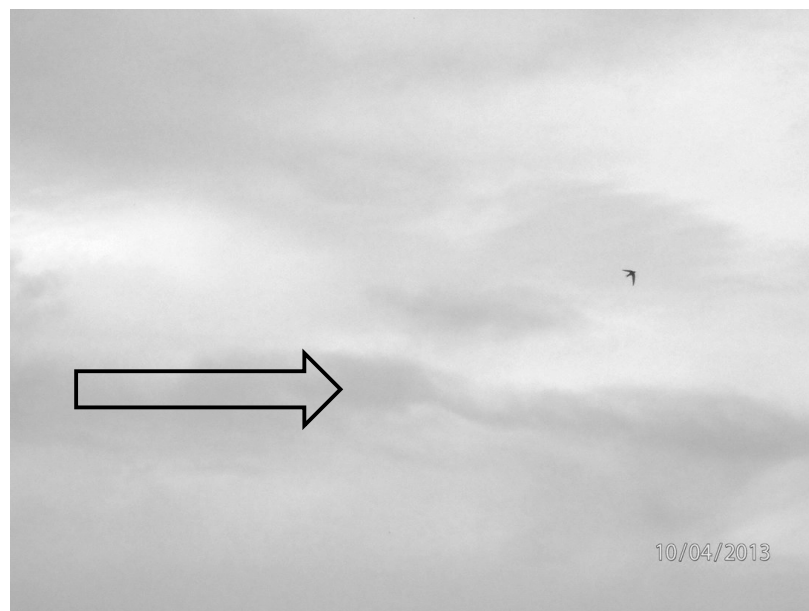


Figure 6 - A photograph of an ash plume from Mt. Etna mixing with local mid-level cloud – arrow indicates plume layer (Malton, 2013).

It therefore remains that flight crews have no effective means to maintain safe flight in the proximity of VA plumes, as visual detection is impossible and there is no currently certified sensor to fit to a commercial aircraft. This has been recognised by the 4th meeting of the ICAO's International Volcanic Ash Task Force (IVATF) in June 2012 where it was stated that “Technologies to measure, record, monitor or warn flight crew of the degree of volcanic debris contamination or damage caused by volcanic cloud were not mature or commercially available.” (International Civil Aviation Organisation, 2012).

The need for a sensor to detect ambient VA concentrations is real and urgent, but not just limited to commercial aviation interests. The science community also has a requirement for a sensor for functions such as ground truth measurements for satellite data and real-time monitoring of plume dispersion. A real and urgent need however, does not infer a solution can disregard the costs, we must consider the end users' requirements and the costs / benefits of a potential sensor.

Initially we must consider an encounter by a commercial aircraft of ash at a hazardous concentration. The global commercial aircraft fleet is forecast to grow to over 45,000 aircraft by 2033, from the current level of approximately 25,000 aircraft (Ascend., 2014). Depending upon the metric chosen, the average life of an airframe is approximately 25 years (Jiang, 2013). If we use a future global fleet number of 30,000 airframes, and use an elevated average encounter rate of 5 encounters per annum to reflect the increased fleet size, then the mean probability of any airframe encountering ash in a year is 0.017%, and 0.42% in the life of the aircraft. The worst-case scenario of an encounter is a total loss of an aircraft, which to date has not occurred. The three events involving a near loss represent only 2.3% of the total encounters recorded. It could therefore be argued that the probability of any aircraft experiencing a potentially fatal accident due to ash is less than 0.01%. In the event of such an accident there are obviously large human and financial costs, for example the loss of an Airbus A330-300 attaches a hull price of €245.6 million (Airbus, 2014), and the compensation for the 300+ passengers could total €30-300 million depending upon the jurisdiction (figures from the Air France flight 447 accident as a guide (Cosgrove, 2010)). However those direct losses would be protected by insurance and the real losses to the airline would be in lost share value over the medium term and increased insurance costs (Broder, 1990). Viewed in these terms the conclusion has to be drawn that encounter protection system costs have to reflect the fact that despite the high potential loss there is a very low probability of a severe encounter.

The losses experienced during the Eyjafjallajökull eruption were not due to airframe damage or aircraft losses discussed above, but due to the closure of airspace as being hazardous. Those losses were extensive as exemplified by the quoted figure from British Airways losing £100 million over 6 days (Williams, 2010). It would be easy to assume that fitting of a suitable VA detection system would remove those losses but this would not be the case. Airspace classed as contaminated will still be closed regardless of the availability of a commercial detection system. However a detection system which is certified to operate in conditions where VA may be present,

and which gives proven avoidance guidance, an equivalent to current weather integrated systems described earlier, may allow some operation in conditions where non-equipped aircraft are prohibited. This follows the model of systems such as instrument landing categories (UK CAA, 2014). This would require aircraft to have the equipment permanently fitted and certified, including the maintenance instructions for the equipment to ensure continued airworthiness. The fitting and certifying of the equipment should cost less than the losses involved in not flying if the investment is to be cost effective. If we look at British Airways and the 2010 Eyjafjallajökull eruption example:

- i. Assume that 75% of flights could have been flown if certified sensors had been fitted equating to total loss saved = £75 million.
- ii. Fleet size \approx 270 aircraft (Wikipedia, 2014)
- iii. Therefore the cost per aircraft to install detection, and maintain it for the life of the airframe, must be less than £75 million / 270 \approx £280k

With the above estimates in mind, and viewing the costs to risk ratio, it seems likely that operators will wish to find the least complex and cheapest solution to the VA detection problem. This would also fit with the scientific community needs which require a low cost and easily transportable solution, which can be mounted on a variety of platforms, more commonly UAVs (Unmanned Aerial Vehicle).

There are a number of sensor technologies in development and testing to address this need, broadly grouped into optically based and electrostatically based. Optically based systems include:

- a) The AVOID system (Nicarnica AS, 2013) is a remote sensing solution, which is based around a forward-looking IR detector and analyses the signal of the 6.3, 8.6, 10 and 12 μm wavelengths. The wavelength differencing technique mentioned previously is then applied, along with multiple data processing stages to identify the ash concentration and produce a colour output display and warnings (Prata and Barton, 1997). This system is well developed but involves a complex IR sensor involving motorized parts, cooling requirements and calibration and, like all other IR sensor based remote sensing, suffers from loss of vision if water ice or droplets obscure the target area. We believe the system will suffer from high installation and maintenance costs.

- b) A Boeing concept to use cameras to analyse the light bursts from the aircraft strobe lights (Tillotson, 2014). This concept relies on the backscatter from light sources such as the wingtip strobe lights or landing lights. Cameras are positioned to view through apertures to external areas illuminated by the light sources. By analysing successive images with the light sources on and off it is believed possible to discern intensity differences related to backscatter by ash. This concept appears limited in that it is only useable at night and would appear to need several camera points to provide data. It is also unclear how it might discriminate between VA and other aerosols.
- c) A Boeing concept which employs infrared cameras to look for spectral peaks indicative of ash ingestion (Tillotson, 2013). The principle is based on the assumption that particles entrained in the exhaust gases will be high intensity emitters and therefore produce an elevated peak in the monitored spectral window. This concept seems to involve similar levels of complexity in terms of the sensor type and processing requirements as item (a) and therefore would be costly to install and maintain.
- d) Within the “In-service Aircraft for a Global Observing System” (IAGOS) project a concept is being developed using detection from backscatter at specific angles from a projected polarized laser light beam to detect external particles (Baumgardner, 2014, Baumgardner and Newton, 2014). The principle uses the concept that the reflected light will have changes in polarisation, which reflect the morphology of the particle, and thus the sensor will identify ash as irregular particles. The discrimination of ice from ash has still to be proven.

The electrostatically based systems include:

- a) The Zeus project (UK Met Office, 2014) which utilises an industry standard JCI 140 (Chillworth technology Ltd.) field mill device installed internally (Woolley et al., 2013) facing a cabin window. The principle of the system is that the cabin window becomes electrically polarized through either (a) particle interaction with the window generating an external charged surface or (b) charging of the surrounding aircraft generating a polarising field. The field mill detects the electric field between the electrically polarised window and the aircraft ground. The measured output is believed to be corresponding to the particulate concentration outside the aircraft. There appear to be a number of variables which need to be resolved; (a) it is unclear how VA will be discerned

from other particulates, (b) it is unclear how differing aircraft external coatings (for example water based paint or polished finish) will affect the charging process and (c) it is unclear how differing surrounding structure types (for example fibreglass fairings, aluminium / glass fibre or carbon fibre structures) will affect the field mill output. The system does not appear to be designed for permanent certified installation and involves motorised parts that will require routine maintenance.

- b) The gas path debris monitoring system for the F35 Joint Strike Fighter (Powrie and Novis, 2006, Khibnik et al., 2013) is a well developed engine mounted system. The system consists of ring detectors on the engine inlet cowlings and probe detectors on the exhaust section (see Figure 7). The detectors measure perturbations in the electromagnetic field in the inlet and exhaust which can be associated with the ingestion of debris or charged particulates. Analysis of the signals from the 3 sensors is then used to infer the debris type and concentration. This is a currently flying sensor system but involves multiple sensors fitted to each engine with the associated control units and post-processing systems.

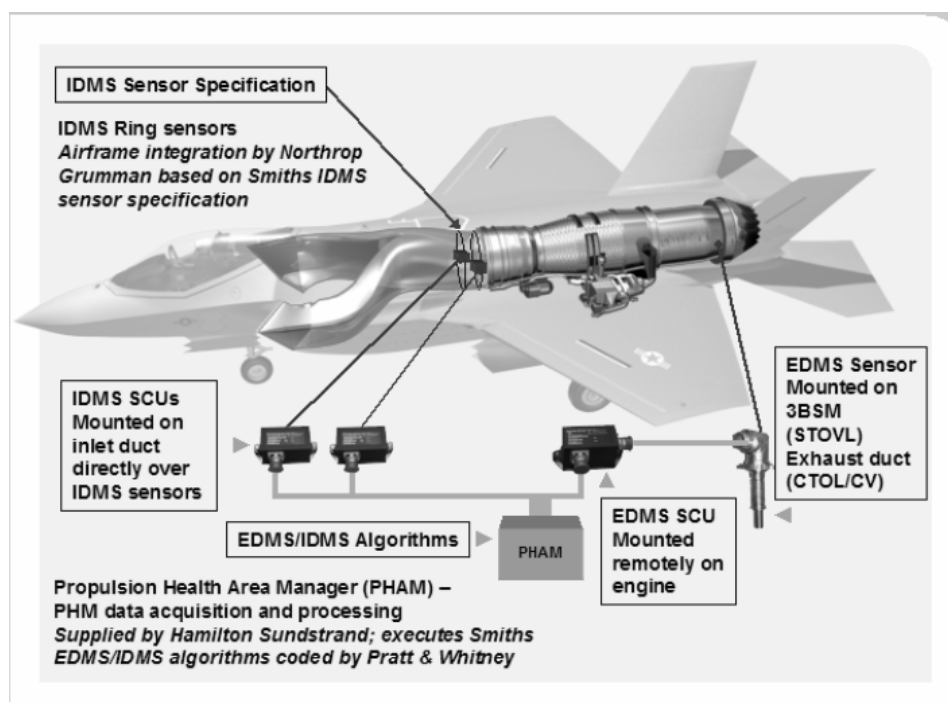


Figure 7 - General arrangement of the F35 JSF gas path monitoring system, after Powrie and Novis (2006) (IDMS - Ingested Debris Monitoring System; EDMS - Exhaust Debris Monitoring System; SCU - Signal Conditioner Unit; 3BSM – 3 Bearing Swivel Module; STOVL - Short Take-Off and Vertical Landing; CTOL - Conventional Take-Off and Landing; CV – Carrier Variant).

- c) A conceptual system by Rockwell Collins to monitor aircraft charging spatially around an airframe (Finley et al., 2014). The system uses an array of two or more voltage detection based sensors to collect charging information from different parts of the airframe. The system then compares the charging levels to create a charge signature to determine the nature of the hazard. However, as with (a) it is not clear how the differences caused by various aircraft coatings and structures would be accommodated without requiring the system to be uniquely tailored to each aircraft.
- d) A system conceived by Cambridge Enterprise Ltd (Welland et al., 2013), shown only in a bench-top configuration, that uses charge collection as the operational basis. The system comprises of conductive elements (cones, plates or wire frames) that are designed to capture particulate from the airflow within an engine compressor bleed air pipe or a pitot tube. The principle assumes that particulate carries an innate charge. If the particulate is considered charge neutral it is imparted with a known charge by a device upwind of the collector. The particulate deposits on the collector and the charge is transferred to the collector. The charge quantity is then representative of the particulate quantity in the flow. This is a simple device but does not consider the physics of what may happen to particulate within the tube flow, as will be discussed within this study.

As detailed in each system description, all but one of these systems employ complex detection methods, often specifying complex detection sensors, and most likely requiring maintenance to ensure adequate performance. As a guide to comparable system costs for an optical system, the cost to install a certified Forward Looking Infrared Radiometer (FLIR) camera system to a Gulfstream business jet is approximately \$100-120k. If certification were required for the installation a further \$50-100k would be added (personal conversation Rockwell Collins engineer, Mike Grumkowski (2014)). These FLIR systems do not require integration into the aircraft avionics displays. We estimate that the cost to integrate, certify and install systems such as the optical sensors proposed would involve costs in the order of \$200-250k per aircraft. We suggest that when assessed in the “whole of life” of the aircraft which includes on-going maintenance, the previously quoted technologies are too complex and expensive for production or aftermarket installation when we consider the cost / benefit calculation previously discussed.

We suggest that an alternative sensor methodology exists, loosely grouped under the electrostatics concept, but based upon the physics of fracto-emission. Fracto-emission is the process whereby high-energy particles and electromagnetic waves are emitted from the fracture of a material. This phenomenon was investigated extensively in the 1980's and 1990's. (Dickinson et al., 1981, Dickinson et al., 1984, Cress et al., 1987, Enomoto and Hashimoto, 1990) and experimentation has continued to the present day on a lower scale (Freund, 2000, James et al., 2000, Samimi et al., 2003, Takano et al., 2013).

Initial work by Dickinson et al. (1978) demonstrated that both electrons and positively charged ions are released during the fracture of oxide coatings on metal alloy substrates, however at this point no mechanisms are suggested. Later work (Dickinson et al., 1981), discussed the possible source of the energies required to liberate these charged particles. Firstly this work suggested that, as the fracture propagates through the material, volatiles in the form of reactive species and ions are released into the crack space. Secondly it was proposed that heat is generated at the crack tip and this heat causes excitation of electrons, and thirdly charge separation at the crack walls may create electric fields to enable emission. The charge separation mechanism was expanded upon in discussion of this work (Derjaguin and Toporov, 1984) proposing that electron emission was due to the bombardment of the crack wall by cations from the opposing wall. However in the same discussion Dickinson proposed that the source of the bombardment particles was the result of gas discharge in the excited volatiles released into the crack space. Dickinson et al. (1982) continued the investigation of the particle species using time of flight measurements, determining that the positive charge particles are light fragments released at fracture, possibly involving the OH^+ or O^+ ions, and invoked the proposal of high energy sites on the fracture surface. (Dickinson et al., 1984) finalised their theories into a five step model involving: (a) charge separation occurs at the crack wall during fracture, (b) desorption of volatiles occurs from the fracture walls. (c) gas discharge within the crack produces bombardment ions and electrons, (d) the bombardment of the crack walls produces high energy sites and "positive holes", (e) electron bombardment adjacent to the positive holes results in positive ion release. Cress et al. (1987) disputed the gas discharge aspect of this model, but agreed that particle emissions occurred at fracture, and that these emissions may also be associated with electromagnetic emissions in the visible light range and radio range demonstrating potentially high energies. The work of Enomoto and Hashimoto (1992) identified charge emission associated with the fracture of rock under the

pressure of an indenter, where both positive and negative charges were detected as being emitted. The work also identified influence of the moisture content of the rock with emissions increasing by two to three orders of magnitude when high moisture content rock was tested. The research of James et al. (2000) demonstrated that the fracture of volcanic materials in a vacuum, and at atmospheric pressure, produced both electrons and positive ions, along with charged particulate, with net charge to mass ratios of the particulates of approximately 10^{-5} to 10^{-6} C kg⁻¹. Specific charges on particles were stated as up to 10^{-3} C kg⁻¹. It was also found that the experiments conducted under atmospheric conditions showed evidence of ion scavenging and net charge reversals compared to vacuum. The work of Dickinson et al. (1984) had so far proposed the most detailed mechanism for the emission of charged particles during fracture, until the work of Freund (2000) investigated high velocity impacts into rock samples, also finding electrical activity associated with the fracture of igneous rock. Freund (2000) demonstrated “when common igneous rocks are subjected to the sudden stress load of an impact event, they generate highly mobile charge carriers.” Freund (2000) asserts “Since the charge carrier are electronic, it is of diagnostic value to know that they are positive.” The findings align with Dickinson et al. (1984) in that Freund (2000) proposes that charge movement is due to electron deficient OH and O species, however Freund proposes that the generation of “positive hole” sites at the fracture surface is due to charge movement within the bulk material rather than surface bombardment.

Whilst the mechanism of charge production may as yet be unclear, the empirical evidence is that fracto-emission occurs and generates net charges proximal to fractured surfaces. The hypothesis presented in this study is that this phenomenon may provide the basis for a low cost passive volcanic ash sensing technique. It is suggested here that, although there are many studies investigating the nature of particle / surface interactions in terms of purely tribo-electric effect or work function / contact charging, the influence of particle fracture on impact with a surface has been a largely neglected area of research. However if we look at the structure of a typical explosive dispersed ash particle (see Figures 8 and 9) it can be seen that, due to the vesicular and granular agglomerate nature of the particle, it is highly likely to break upon impact with a hard surface. Our hypothesis continues to suggest that high energy electrons and ions, generated by fracto-emission during the impact of an irregular or granular particle on a metallic surface, may generate sufficient charge current to drive a detection system.

The empirical evidence demonstrates that the fracture of pumices and other volcanic products can generate specific charges (single polarity) at a charge to mass ratio of $10^{-3} \text{ C kg}^{-1}$ (James et al., 2000). The same empirical findings demonstrated that the charges generated during fracto-emission are of both polarities, and the net charge in a volume of particulate was at least an order of magnitude less than the specific charge. Therefore we can propose the specific charge value as an upper limit of the charge that may be generated by volcanic ash impacting a metallic aircraft surface. Now consider a Boeing 747 Jumbo Jet (B747) which cruises routinely at 480 kts TAS (true airspeed) (Personal communication Captain D Edmondson, British Airways, 2012), and further consider a forward facing conductive surface of cross sectional area perpendicular to the flow of 100 mm x 100 mm. That surface will pass through a volume of approximately $2.5 \text{ m}^3 \text{ sec}^{-1}$. If the ash concentration is at the Low Contamination level limit of 2 mg m^{-3} then that surface could impact 5 mg of ash particulate per second. This could potentially generate a current of

$$\begin{aligned} 5 \times 10^{-6} \text{ kg s}^{-1} \times 10^{-3} \text{ C kg}^{-1} &= 5 \times 10^{-9} \text{ C s}^{-1} \\ &= 5 \text{ nA} \end{aligned}$$

This is a potentially measurable signal.

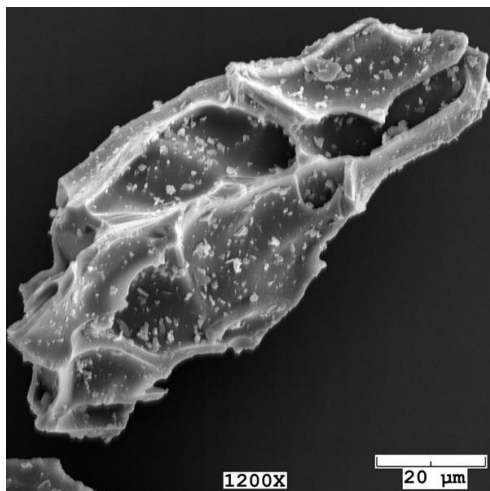


Figure 8 – A scanning electron microscope image of ash from Mount Redoubt eruption of 2009 (Izbekov and Shipman, 2009).

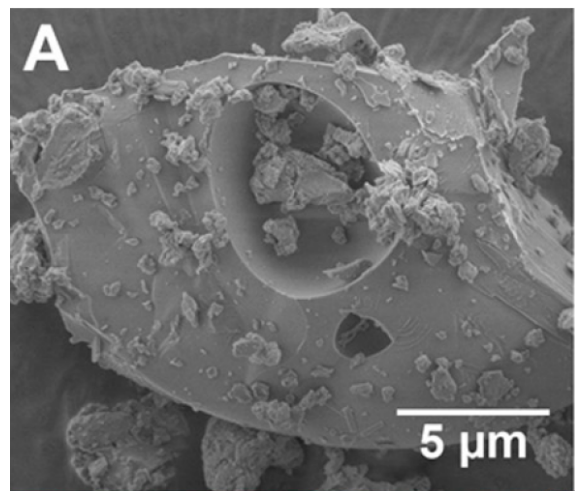


Figure 9 - A scanning electron microscope image of ash from the Eyjafjalljökull eruption of 2010 (Gislason et al., 2011).

This study is an applied investigation into this hypothesis, and attempts to:

- I. Provide empirical evidence of fracto-emission when particulates are deliberately impacted with a metallic surface, commensurate with the previous research.
- II. Investigate whether the character of the charging signal may be correspondent to the relationship between the impacting particle and the impact surface material.
- III. Look at bulk processes in atmospheric conditions in order to determine whether a useable signal in terms of discernibility is likely in atmospheric conditions.

2 Method.

2.1 Principle of the Experimental Setup.

The purpose of this study was to investigate the electrical charge generated by impacts of particulates on a metallic target surface. In the real system the suspended particulate is stationary and the target surface (the aircraft) is moving through the volume of air. Experimentally, the only expedient approach is a stationary target impacted by particles in a moving airstream. Ideally a volume of air with a known concentration of suspended particulate (mg m^{-3}) in a electrical charge neutral charge state would be accelerated (while maintaining uniformity and neutrality), to impact a target of known area. Practically this ideal is likely to be difficult to achieve. However an alternative method, creating an analogy of those impact conditions may be suggested as follows:

- a) Consider a mass 1 mg of VA with a known grain size distribution. It is possible to calculate the number particles within that mass as n_{VA} particles / mg.
- b) If we now consider a suspended VA concentration of $Y_{VA} \text{ mg m}^{-3}$ it is possible to express that as a particle concentration of $n_{VA} \cdot Y_{VA}$ particles / m^{-3} .
- c) Any surface on an aircraft travelling at velocity $V \text{ ms}^{-1}$, with a cross-section normal to the flow of $x \text{ m}^2$ will encounter an air volume of $V \cdot x \text{ m}^3$.
- d) This volume will contain $n_{VA} \cdot Y_{VA} \cdot V \cdot x$ particles, and therefore initiate approximately an equivalent number of impacts on the surface.
- e) Therefore if we generate a flow that initiates an equal number of particulate impacts at an equivalent velocity against a target, we can plausibly assume this would be representative of any scaled equivalent concentration and cross-section combination.

Using this approach, experiments were designed to project a narrow high-speed airflow with entrained particulate of known grain size distribution against a small target. The target size was chosen based upon: (a) the limits of the equipment size; (b) the discussion shown in the Introduction where exposure of a 100 mm x 100 mm target at aircraft cruising speeds would impact 5 mg s^{-1} of VA in an ash concentration of 2 mg m^{-3} . Our equipment limited our target size to 50 mm x 50 mm and at 45° to

the airflow resulting in a normal cross section of 0.0018 m^2 . At this size we were still able to impact the desired mass rate to replicate the larger target. The experiment measured the charges generated at the target. However, any energetic mechanical handling of particulate results in charge generation (Jonassen, 2002), therefore the experiment also measured charging in the particle lofting phase in order to make an assessment of the charges that were already on the particulate when it arrived at the target.

2.2 Experimental Equipment.

The experimental equipment consisted of the following components:

- i. A high-pressure air supply and nozzle to generate the impacting airstream.
- ii. A particulate sample feed system to loft the particulate material and entrain it into the high speed airflow.
- iii. A metallic target.
- iv. An electrical signal sensing system to measure the electrical charge generated at the target and other parts of the equipment.
- v. An enclosure for the target to contain the blown particulate, including a dust extraction system and the associated equipment mountings.
- vi. An earthing and shielding system.
- vii. An ancillary ice cloud generation box.

An evolutionary process refined each component during the research programme.

An overview of the final configuration of the equipment is shown in Figure 10.

2.2.1 The High Pressure Air Supply

High-pressure air was supplied from a commercial oil-less workshop compressor (Airmate Hurricane 25) rated at 8 Bar (116 psig) and 113 l min^{-1} free air delivery. The supplied air was routed to a commercial filter / regulator unit (Clarke CAT41), which was used to control the feed pressure to the nozzle and remove most of the entrained water condensate. An inline filter / desiccant dryer (SIP 07564) was fitted to the regulator output to minimise any remaining entrained water. The desiccator / filter unit was replaced daily. The supply was then routed to an on / off ball valve and then to the nozzle assembly. All connections were made using commercial 8mm ID rubber airline (Clarke RH10) and industry standard PCL quick disconnect fittings.

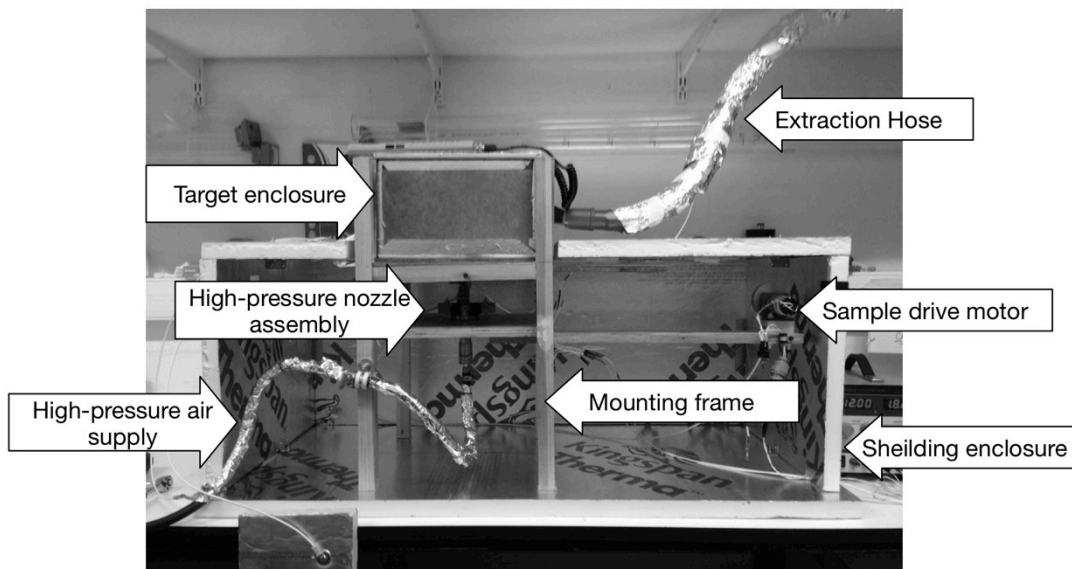


Figure 10 - An overview of the evolved test equipment configuration with the main components arrowed.

The design considerations for the high pressure air supply were to, (a) be able to create an airflow velocity as close to 100 m s^{-1} as possible, (b) maintain the flow for an adequate time for stable measurements to be taken and (c) create a low pressure zone for the entrainment of the particulate sample. The airflow velocity was chosen as being as close to commercial airliner flight speed as we considered could be achieved within the limitations of the equipment.

The nozzle assembly evolved to the final design through five revisions, incorporating improvements to the feed and entrainment of the sample particulate, and improvement of the air pressure control. Revision 1, detailed in Appendix A, was found to be successful in terms of the venturi method of particulate entrainment, but it delivered sample particulate at a rate far higher than the required 5 mg s^{-1} or less. Revision 2, detailed in Appendix B, provided greatly improved sample dispensing control, but changes to the sample feed system to move the sample particulate dispensing closer to the target and inline with the main airflow required further modifications. It was also considered desirable to try to introduce separation of the entrained particulate from the nozzle jet walls by introducing an 'air wall'. The revision 3 changes are detailed in Appendix C and a general arrangement of the revision 3 configuration is shown in Figure 11.

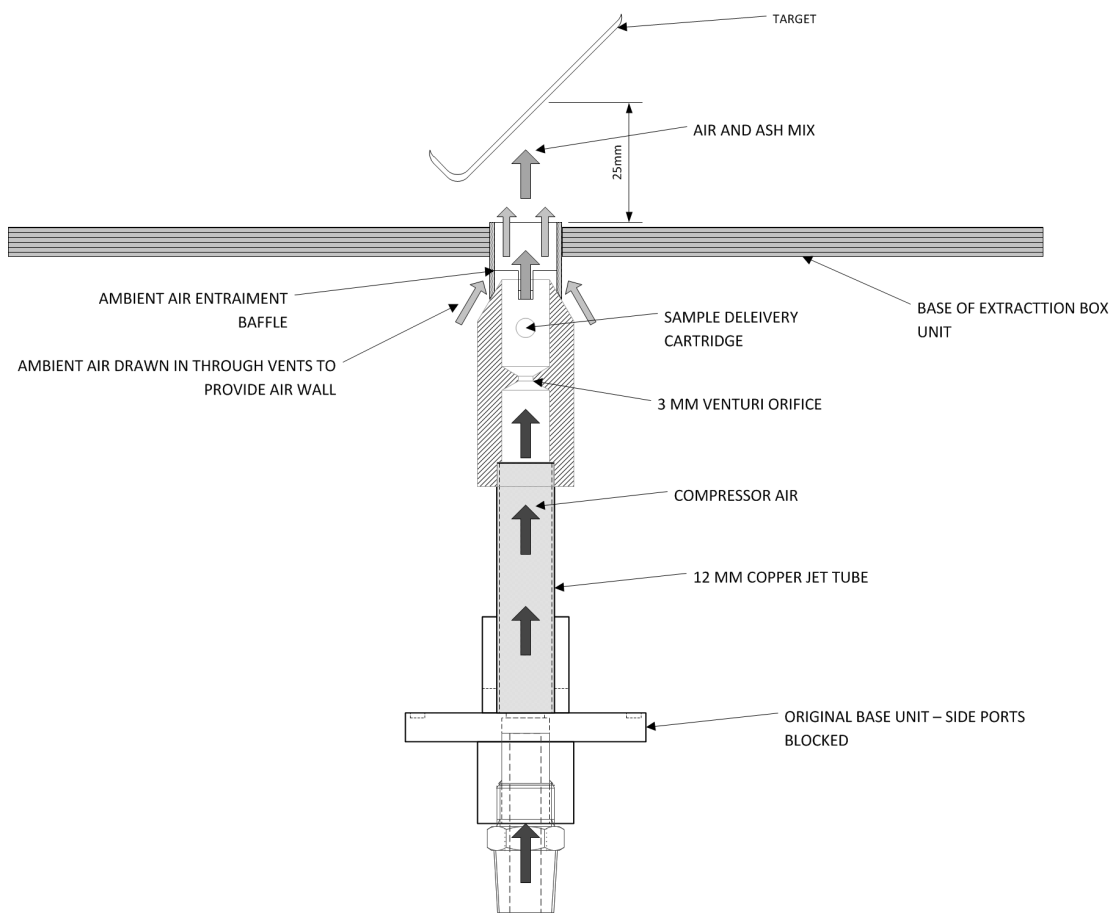


Figure 11 - General arrangement of the revision 3 high pressure air nozzle showing predicted air entrainment path.

Revision 3 was an improvement but further changes to the sample feeder system were required as the location of the feeder cartridge directly in the high-speed flow resulted in very high charging rates at the feeder. Revision 4 as detailed in Appendix D gave a partial improvement, but it proved necessary to move the side feeder tube to above the nozzle, mounted remotely on the base of the target enclosure box. Revision 5, the final revision, was therefore revision 4 but with the side feeder tube removed and the 8 mm angled hole in the high-speed nozzle upper fitting blocked with epoxy resin. The copper tube shroud was cut down to the thickness of the base of the target enclosure (Figures 12 and 19). The nozzle assembly was electrically isolated from the mounting frame using rubber gaskets and nylon attachment hardware but connected to ground via an earth cable (Figure 12).

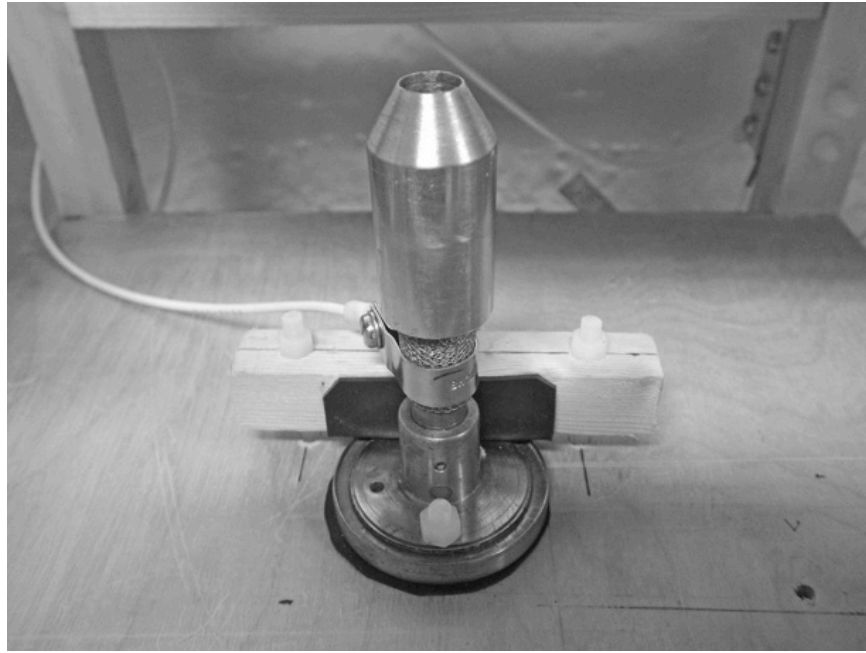


Figure 12 - The final revision 5 high-pressure nozzle.

2.2.2 The Particulate Sample Feed System

The particulate feed system also evolved to the final design through five revisions, incorporating improvements to the feed and entrainment of the sample particulate

The revision 1 particle feed system consisted of a conical hopper that enshrouded the high-pressure air supply nozzle revision 1 (Appendix A Figures 81, 82 and 85). Particulate was entrained by venturi action into the low-pressure area in the high-pressure flow, through the drilled apertures in the copper jet tube, downstream of the orifice plate. This system, based upon the work of Xie et al. (2011), was effective but delivered sample at an excessive rate (§ 2.2.1).

The revision 2 feed system was developed to supply small mass quantities with as little mechanical handling of the sample as possible to avoid friction charging or particle breakage resulting in fracto-emission. The design consisted of three components (overview Figure 13):

- a) A tubular cartridge unit to hold the particulate sample (Appendix E). A macro image is shown in Figure 14 of VA loaded into the cartridge inner.
- b) A side feeder tube, incorporating a connection point for the cartridge unit, which was attached to the nozzle base unit at 90° to the high-pressure flow,

venting into the low-pressure venturi zone (Appendix B Figures 86 and 87; Appendix F).

- c) A draw-wire traction system to pull the cartridge inner through the system (overview Figure 17). The motor was operated at input voltages ranging from 6V to 12V. A series of three calibration runs at input voltage intervals of 1V were carried out to test the linearity of the speed of pull (Appendix G)

The principle of operation is atmospheric air is drawn into the side feeder tube due to the low-pressure area of the venturi zone, creating a flow along the tube. The cartridge inner loaded with particulate sample is drawn across this flow, and the low-pressure area around the cartridge, along with turbulence of the crossing flow, lofts the particulate from the slot in the cartridge. The lofted particulate is then drawn into the high-speed stream in the venturi zone (Figure 13; detail views Figures 15 and 16). The amount of particulate lofted is controlled by the draw rate of the inner cartridge across the side feeder tube, which is regulated by the motor voltage. Using a high-g geared motor means small voltage errors result in very small RPM changes, and the high torque means that slight friction changes in the cartridge will not slow the drive.

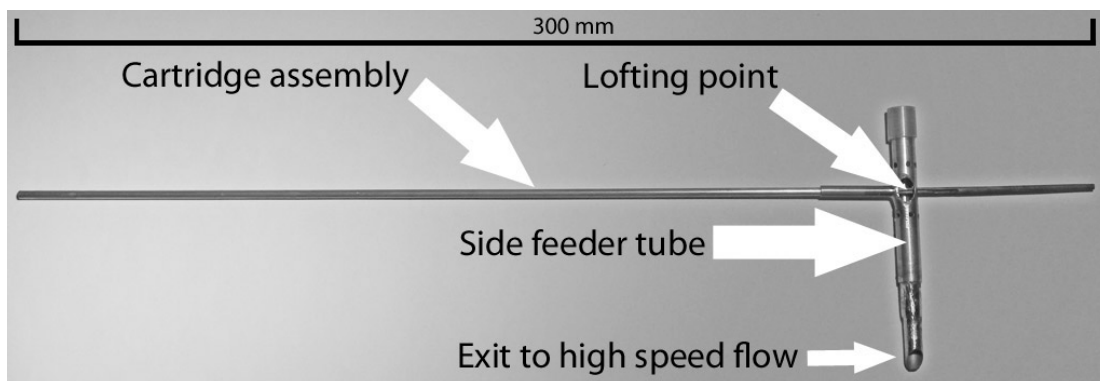


Figure 13 - General overview of the revision 2 sample feeder system with the wall of the side feeder tube removed at the lofting point to show the cartridge crossing.

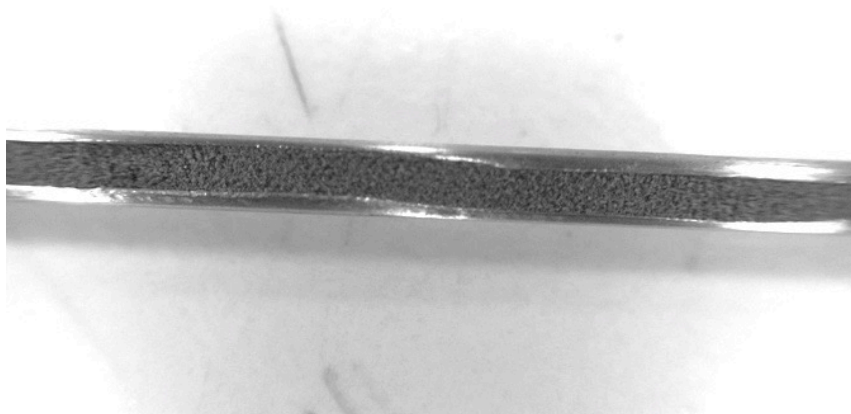


Figure 14 - Detail of volcanic ash particulate sample loaded into a cartridge.

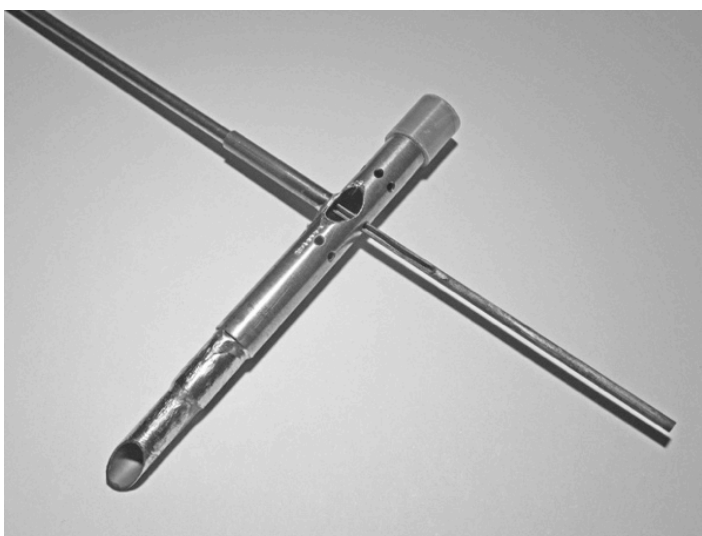


Figure 15 - Overview of the side feeder tube with sample cartridge installed - Note the feeder tube wall has been removed to expose the cartridge in place.



Figure 16 - Detail cutaway view of the sample cartridge inner passing through the side feeder tube - note the tube wall has been removed to show the cartridge in place.

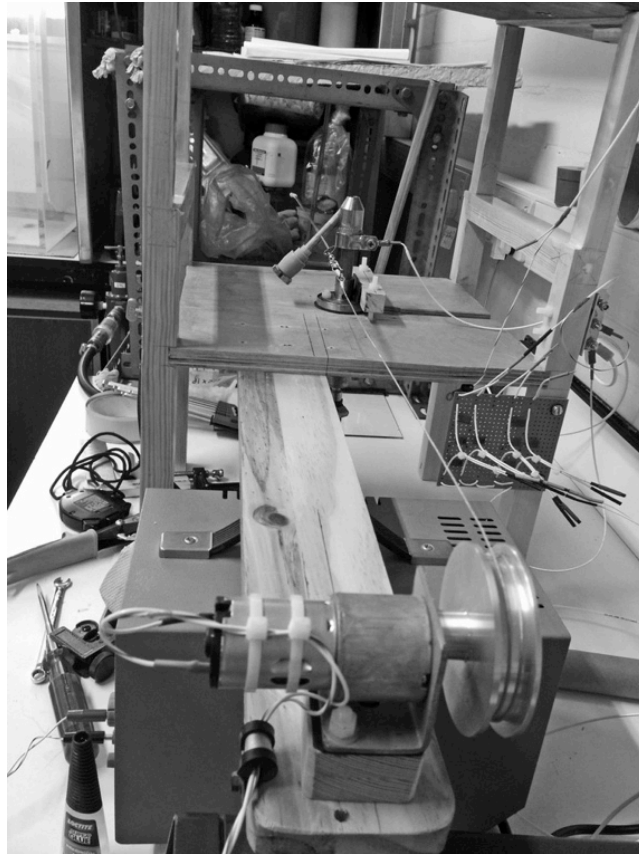


Figure 17 - Overview of the draw-wire mechanism in place and connected to the sample cartridge (at rear of photo).

The general arrangement of the revision 2 particulate sample carrier and draw-wire system was the basis for the remaining revisions. Changes from this point were attempts to reduce the particle charging which was occurring at the feeder system.

Revision 3 removed the side feeder tube and mounted the cartridge in the throat of the upper high-speed nozzle assembly (Figures 91 and 11). This configuration yielded lofting of very high energy and was abandoned.

Revision 4 returned to a straight, parallel bore, side feeder tube of 8mm OD / 7mm ID and removed the radial holes visible in figure 98. The side feeder tube was moved to the throat of the upper fitting of the high-speed nozzle and aligned at 30° to the high-speed flow (see 2.2.1 and Figure 101). Revision 4 also introduced a gauze filter to the inlet of the side feeder tube. The aim of the filter was to reduce inlet turbulence and provide a means of restricting and controlling the inlet flow by means of adding or removing layers of gauze – see Figure 18. By check weighing before and after experimental runs the filter also acted as a check to ensure all the particulate was being ingested into the target enclosure rather than falling back against the flow and out of the side feeder tube.



Figure 18 - The side feeder tube inlet filters.

Revision 5, which was the final arrangement, maintained the same configuration as revision 4 but moved the side feeder further downstream in the high speed flow, mounting it in the external air entrainment zone in the base of the target enclosure box (Figure 19).



Figure 19 - Revision 5 side feeder tube assembly mounted in the base of the target enclosure.

2.2.3 The metallic target.

The targets were cut and folded from stock sheet material (Figure 20). The flat face impacted by the particulate stream was 50 mm x 50 mm and the face was aligned at 45° to the airstream. The targets were drilled in two places to accept silicon rubber mounting grommets through which the mounting bolts fitted, electrically isolating the target from the mounting. The assembly was bolted to the central mounting pillar

within the enclosure (Figure 103). The electrical connection was made using a bolted joint.

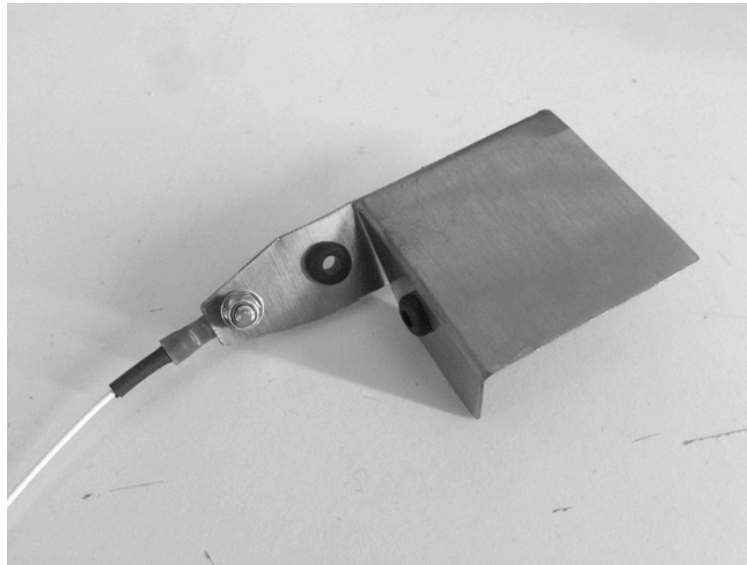


Figure 20 - An example target.

The materials chosen were:-

- Specification 1050 Aluminium (99.5 % pure – unalloyed).
- Specification 260 (ASTM B36) Brass (68.5-71.5% Cu, 28.5-31.5% Zn, Trace Fe and Pb).
- Stainless Steel.

The material choice was based on the criteria of needing to be robust enough to withstand VA impact and suitable to be considered for use in an aircraft environment, which can include temperatures of +50°C to -60°C, water, ice and chemicals such as de-icing fluid.

2.2.4 The electrical signal sensing system

The electrical signal sensing system consisted of two channels. Each channel was connected to an electrically isolated component, either (a) the impact target (§ 2.2.3) or (b) the sample feeder system (§ 2.2.2). The wiring diagrams are shown in Appendices 0 and I.

The connection to the target was bolted (Figure 20) and the connection to the feeder system consisted of a stainless steel gauze compression wrap held in place with an aluminium P-clip and bolted joint (Figures 101 and 19). Each measurement point

was connected to ground via a commercial 100M Ω resistor, meaning any charge generated at either the target or side feeder tube would be bled to ground via the 100M Ω resistor. The resistance values were measured using two Keithley Model 614 electrometers and found within a range of maximum of $\pm 0.4\%$ of the rated values. The voltage, V , across each resistance, R , was measured using Keithley Model 614 electrometers allowing calculation of current flowing, I , by way of Ohms law $V=IR$. Wiring between the measurement points and the electrometers was all 20AWG Raychem 55 shielded cable and the 100M Ω resistors were mounted on commercial "breadboard" prototyping board. Connections at the measurement points were by commercial PIDG ring crimps. Connections otherwise were solder or aircraft grade gold plated Mil. Spec. (MS) connector pins and sockets sleeved in heatshrink.

The Keithley Electrometers were set to an input range of $\pm 2V$ DC. The analogue output from each electrometer is also 2V, which enabled a 1:1 relationship input/output. However it should be noted the electrometer analogue output is inverted in voltage mode by design. Correction of the recorded signal was carried out in post processing. The analogue outputs were routed to a Picoscope 2202 USB oscilloscope connected to a Windows PC. Picoscope V6 software processed and displayed the output. Each channel was sampled at 2Khz with $\pm 2V$ full scale and saved in Picoscope format (.psdata).

2.2.5 The target enclosure and equipment mountings.

The target was required to be enclosed in order to facilitate the capture of the particulate and avoid the entrainment of external materials. The extraction and capture of the particulate would be accomplished using a commercial vacuum cleaner (Vax Power6). This enclosure required mounting in such a way as to facilitate the fitting and support of the sample feed system and high-pressure air system. The enclosure also required a dust extraction. Wood was chosen as the construction material for several reasons; (a) low electrostatic charging tendency, (b) low cost and (c) ease of working and re-working.

The target enclosure had two evolutions. The revision 1 enclosure is detailed in Appendix J. The flow in the revision 1 enclosure was poor, with multiple stagnant areas and vortices. The flow was checked using smoke generator sticks and allowing the smoke to enter the enclosure via the side panel. Revision 2 is detailed in Appendix K and included: flow improvements to minimise stagnant areas and

vortices; incorporation of revision 3 of the high-pressure air nozzle (§ 2.2.1); lowering of the target to increase the air flow velocity at the target face and reduce the amount of flow divergence before impact with the target; various electrical isolation measures to reduce induced fields. Revision 2 was the final configuration however shielding modifications required the replacement of the glass front viewing panel to be replaced with a solid plywood panel (§ 2.2.6).

2.2.6 The earthing and shielding system.

The earthing of the equipment was based as far as possible upon an “earth point and star” configuration to avoid loops which may generate electromagnetic interference (EMI) into the signal lines. The earth point consisted of an aluminium strip and was mounted using nylon hardware on the equipment frame.

During early experiments no shielding was thought to be required, and while mains frequency EMI was present, it was thought adequate to filter this out during post-processing of the data. The earthing arrangement is shown in appendix 0.

However it was discovered that positive voltage offsets and voltage spikes were being induced into the target, and more prominently into the feeder assembly, by external electromagnetic fields from the dust extraction piping. It was therefore necessary to carry out a shielding and earthing program to remove this EMI.

This program introduced the following:

- i. Introduction of a new star earth point.
- ii. Aluminium foil shielding attached to the interior surfaces of the target enclosure box, earthed to the new star point.
- iii. Aluminium foil wrap of the vacuum extraction suction hose, earthed to the new star point, and re-routing of the hose away from the target enclosure.
- iv. Aluminium foil wrap of the high-pressure air supply hose earthed to the star earth point.
- v. Construction of a shield enclosure for the lower experimental rig including the sample feeder drives, earthed to the new star point. The enclosure was constructed from commercial insulation board, faced both sides with aluminium foil and had a removable front panel.
- vi. Earthing of the sample feeder system drive motor to the new star point.

The final earthing and wiring arrangement is shown in Appendix I. Overviews of the shielding enclosure installation are shown in Figure 21 and Figure 22.



Figure 21 - An overview of the test equipment with the shielding box complete.

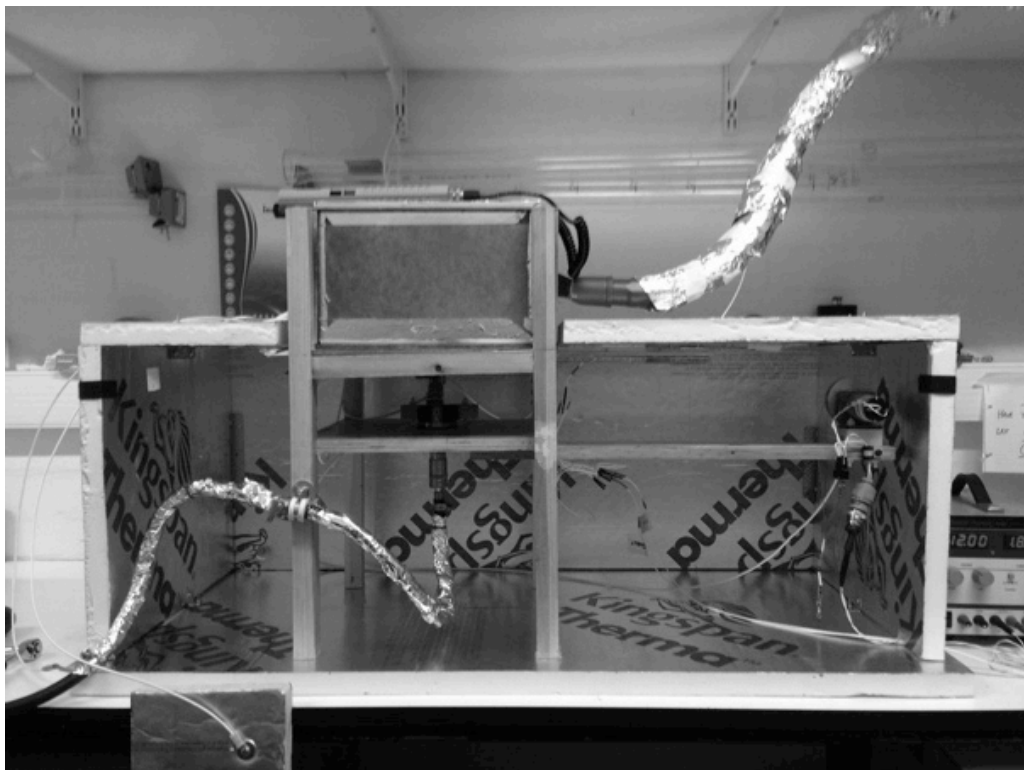


Figure 22 - An overview of the test equipment with the front panel removed and the extraction hose fitted.

2.2.7 The ice cloud generation box.

A method of producing a volume of ice particles was developed to carry out qualitative trials of ice impacts with the test targets. A compartment was fabricated from 25mm Kingspan insulation board which fitted beneath the target enclosure and which enclosed the inlet port of the side feeder tube assembly. The compartment was divided by a steel gauze shelf into a lower open section, and an upper section that contained dry ice. The dry ice cooled the air to below -45°C . At this temperature water will freeze rapidly (Wood et al., 2002). The water injection was done using a commercial Badger model 150 airbrush, which directed a jet of water spray into the lower compartment via an aperture in the vertical side.

The box was fitted to the enclosure mounting and the upper section filled with dry ice. The temperature in the lower open section was monitored with a K-type thermocouple and allowed to fall to below -45°C . The airbrush then injected a water mist into the lower compartment, which was then ingested as ice into the side feeder tube.

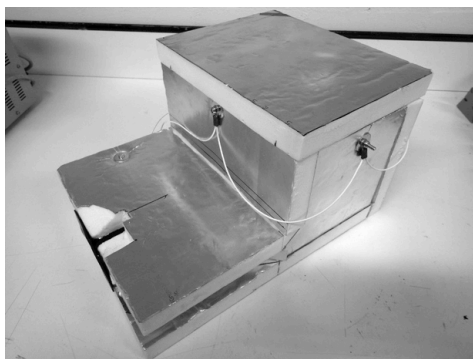


Figure 23 - Overview of the ice cloud generation compartment.

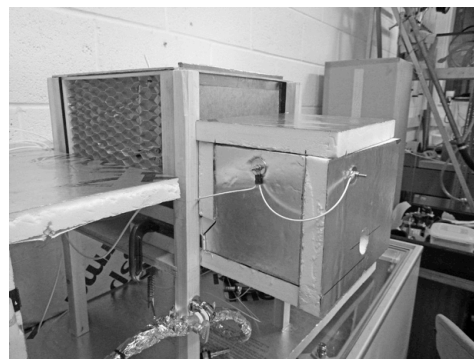


Figure 24. - The ice cloud generation compartment installed on the target enclosure frame.

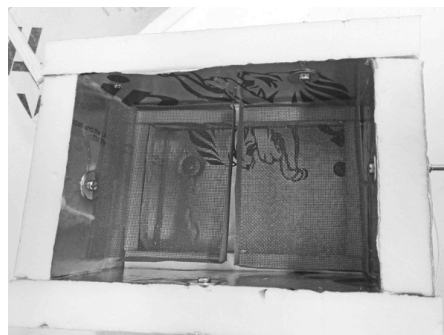


Figure 25 - An internal view of the ice cloud box showing the gauze dry ice trays.

2.3 Experimental Procedure.

Four materials were used as particulates for the experiment:-

- 1) Volcanic ash collected from the Eyjafjallajökull eruption of 2010 (E15 ash). Unsorted ash was supplied by the University of Iceland which was then manually sieved to <63 μm fraction. The E15 ash has been previously analysed by Ivleva et al. (2013), who reports the presence of goethite ($\text{Fe}^{3+}\text{O}(\text{OH})$), hematite ($\text{Fe}^{3+}_2\text{O}_3$), glassy SiO_2 matrices and alkali feldspars ($\text{Na}(\text{Si}_3\text{Al})\text{O}_8$ and $\text{K}(\text{Si}_3\text{Al})\text{O}_8$). Gislason et al. (2011) analysed both the bulk ash and the surface coatings of E15 particulate. The bulk ash was found to be 58% SiO_2 , which is consistent with the other work, along with oxides of Al, Fe, Mn, Mg and others. The study also found surface coatings of multiple compounds (epsomite, $\text{Mg}(\text{SO}_4)\cdot 7(\text{H}_2\text{O})$; scacchite, $\text{Mn}^{2+}\text{Cl}_2$; melanterite, $\text{Fe}^{2+}(\text{SO}_4)\cdot 7(\text{H}_2\text{O})$; Na-metaborate, NaBO_2 ; Na-orthophosphate, $\text{Na}_3(\text{PO}_4)$; ralstonite, $\text{Na}_{0.5}\text{Mg}_{0.5}\text{Al}_{1.5}\text{F}_4(\text{OH})_2\cdot (\text{H}_2\text{O})$; hieratite, K_2SiF_6 ; malladrite, Na_2SiF_6 ; thenardite, $\text{Na}_2(\text{SO}_4)\cdot 10(\text{H}_2\text{O})$; arkanite, K_2SO_4 ; halite, NaCl ; and antarcite, $\text{CaCl}_2\cdot 6(\text{H}_2\text{O})$). A sample particle is shown in Figure 9 and is an agglomerate of particles around a larger core
 - i. Commercial Ballotini™ 45 - 90 μm spherical glass bead from Potters Industries LLC (USA) and were specification AH 170-325. The bead diameter range is 45 to 95 μm with a density of 2500 kg m^{-3} and a roundness of 85%. They are specified with 0% free silica (Potters Beads LLC, 2011). The chemical composition (derived from the Chemical Abstracts Service (CAS) number) is NaO_4PZn .
- 2) Aeolian sand that was manually sieved to <63 μm fraction. The sand was of an unknown origin but is assumed as quartz (SiO_2) grains with Fe impurities indicated by the yellow colouration.
- 3) Volcanic ash collected from the Sakurajima eruption of 1991 (Sak ash). Unsorted ash was supplied by Dr. J Gilbert of Lancaster University, which was then manually sieved to <63 μm fraction.

A primary aim of the study is to identify evidence of fracto-emission. The experimental means of achieving that aim was to compare the charging behaviour of a material that is likely not to fracture, to the one most likely to fracture, that is, volcanic ash. The 45-90 μm diameter Ballotini™ beads were chosen as the non-fracture material, being closest to the sieved ash samples and closest in nature to

those used in earlier contact charging works. The structural differences can be seen comparing the images in Figures 8 and 9 with Figures 26 and 27. It is evident that the Ballotini™ has a spherical form and uniform glass bulk which suggests a resilient particle. The VA particles are more angular, and have coatings which can include small grains. It is proposed that the Ballotini™ are much less likely to fracture on impact than the E15 VA.

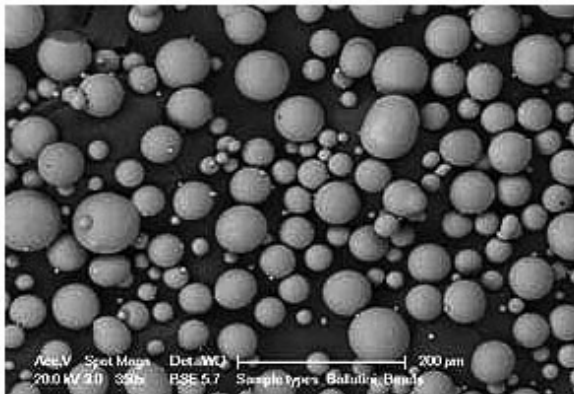


Figure 26 – Scanning electron microscope image of Ballotini™ - image courtesy of The University of Auckland (2014).

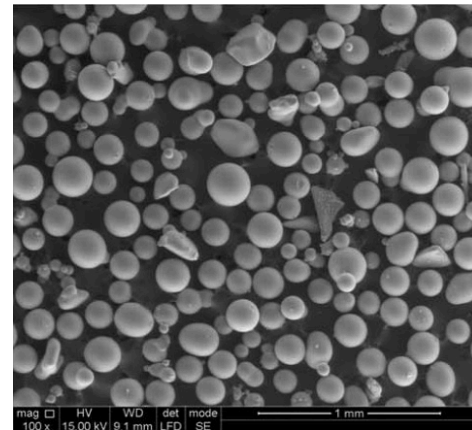


Figure 27 – Scanning electron microscope image of 150 µm Ballotini™ image retrieved from Campo-Deano et al. (2012).

A grain size distribution was carried out on all the sample particulates using a Mastersizer 2000® laser diffraction system.

For each target material - particulate material pair a number of individual test runs were carried out, with the variables of impact speed (high-pressure air flow pressure) and particulate delivery rate (delivery drive voltage) adjusted incrementally. The resulting matrix of completed test runs is shown in Table 2. Time limitations and limited availability of fine sand restricted the final experimental data set.

Table 2 - The matrix of target / particulate pairings, showing the number of individual runs per variable group.

Target	Particulate	High-Pressure air supply pressure / psig	Delivery drive voltage / V	Increment	Number of test runs per increment
Al	E15 ash	40 to 70	12	5psig	4
Al	E15 ash	50	6 to 10	2V	4
Al	Ballotini™	40	12	N/A	2
Al	Ballotini™	45	12	N/A	2
Al	Ballotini™	70	12	N/A	3
Brass	E15 ash	40 to 70	12	5psig	4
Brass	E15 ash	50	6 to 10	2V	4
Brass	Ballotini™	40	12	N/A	2
Brass	Ballotini™	70	12	N/A	3
Stainless	E15 ash	40 to 70	12	5psig	4
Stainless	E15 ash	50	6 to 10	2V	4
Stainless	Ballotini™	40	12	N/A	2
Stainless	Ballotini™	70	12	N/A	3
Al	Sand	50	12	N/A	2
Al	Sand	60	12	N/A	2
Al	Sak ash	50	12	N/A	2
Al	Sak ash	60	12	N/A	2
Al	Ice	50	12	N/A	4
Al	Ice	60	12	N/A	2

The following procedure was used in each of the sample runs. The test target is mounted to the post in the target enclosure and the enclosure reassembled. The continuity to earth of all the screening within the enclosure is checked using a digital voltmeter before the closure of the front panel. The desired air pressure is set on the high-pressure regulator and then the test particulate is loaded into the sample cartridge and the complete cartridge assembly was weighed on a digital scale to an accuracy of ± 0.001 g. The cartridge assembly is mated to the side feeder tube and the draw-wire is connected to the cartridge inner. The required drive voltage is set on

the motor power supply. The cartridge is driven to the point where the start of the sample slot is about to enter the side feeder tube ensuring all slack in the draw-wire has been taken up. The vacuum extraction is initiated. The recording is initiated on the PC (T_0). All the following timings detailed in Table 2 were derived empirically in order to provide a long enough time window to gather accurate data, but also to ensure the set pressure did not fall below the required level as supply pressure decreased in the compressor tank. At the specified time after T_0 the high-pressure air supply is initiated ($T_{air\ on}$). At the specified time after $T_{air\ on}$ the sample cartridge drive is initiated for the required experiment time ($T_{drive\ on}$, $T_{drive\ off}$). After $T_{drive\ off}$, the high-pressure air is turned off at $T_{air\ off}$ and the recording is stopped approximately 5 seconds later. Operation of the equipment was manual and timings were taken from the scope trace progress along the time base. On completion the cartridge is carefully removed from the equipment ensuring no sample is lost, and is then reweighed to find the mass of sample entrained during the test.

Table 3 - Matrix of high-pressure air supply and cartridge drive ON and OFF timings.

High-pressure air pressure / psig	Air ON time $T_{air\ on}$ /sec	Drive On time $T_{drive\ on}$ /sec	Drive OFF time $T_{drive\ off}$ /sec	Air OFF time $T_{air\ off}$ /sec
40	5	10	25	30
45	5	10	25	30
50	5	10	25	30
55	3	5	20	22
60	3	5	20	21
65	5	5	20	21
70	5	5	15	15

A control test was carried out at the start and end of each day. The control configuration was aluminium target / E15 ash / 50 psig high-speed pressure / 12V sample drive. The data were saved in the proprietary Picoscope (.psdata) format. For those experiments using the attached ice box the cartridge feeder was omitted, and the compressor supplying the high-pressure airflow was pressurized and chilled overnight to -30°C.

2.4 Data post processing.

The Picoscope device is specified at 8 bit resolution. This results in the device having a single bit resolution of approximately 0.0156 V when a range of ± 2 V is selected. This digitisation step value can be seen in Figure 28.

Experimental data were processed using Picoscope software where the correction of the signal could be carried out, along with the creation of a calculated channel to provide current (nA) values (using $I=V/R$ where $R=100\text{ M}\Omega$). The current (nA) data were then exported in comma separated (.csv) format and imported into Wavemetrics Igor Pro V6 software for further processing.

Step one was to remove high frequency EMI from the signal by carrying out a 35-point box smoothing. Figure 28 shows an example comparison of an unsmoothed and smoothed signal. A 35-point centre point based algorithm was found to be the best compromise between response loss and EMI reduction.

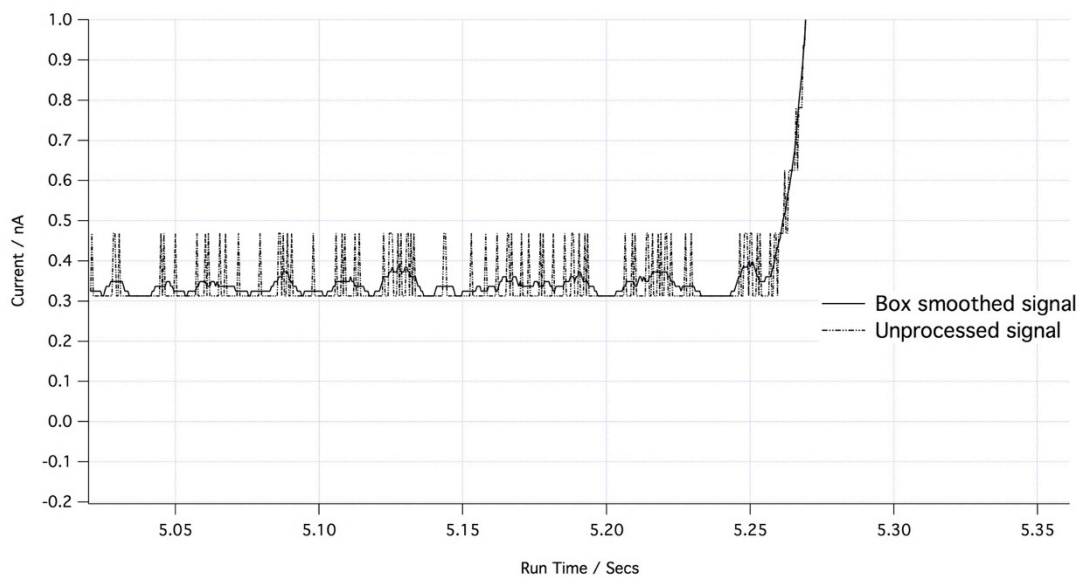


Figure 28 - An example of an unsmoothed signal and the same signal smoothed using 35-point box centre point algorithm.

Step two was to select the section of the recorded data that contained stable conditions of delivery and pressure, this usually being the latter 2/3rds of the sample delivery portion (between $T_{drive\ on}$ and $T_{drive\ off}$) of the data set. Similarly a section of

zero signal data between T_0 and $T_{air\ on}$ was selected to process for offset correction. An example is shown in Figure 29.

The “wave” function was used in Igor Pro to calculate the integral of the two sections of data (Igor Pro uses trapezoidal integration method). The integral will give a total area in units of nA s or nanocoulombs (nC). This value was divided by the time in seconds to give an average value for nC s⁻¹ for both sections of data. The true average charge generation rate can then be found by subtracting the offset value from the total signal value.

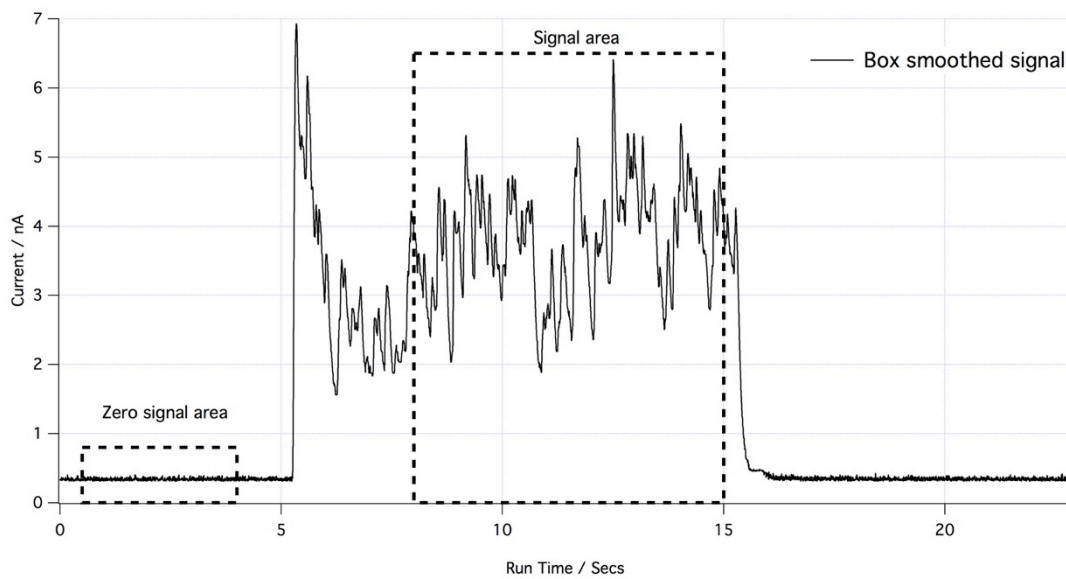


Figure 29 - An example of data selection for processing. The signal area is considered stable sample delivery conditions and the zero signal area is used for offset adjustments.

The average particulate mass delivery rate was calculated by dividing the total mass used by the drive on time.

Therefore if:

$$\dot{m}_{s\text{amp}} = \text{sample mass delivery rate} / \text{mg s}^{-1}$$

$$I_T \text{ (or } I_F) = \text{charge rate of the target of sample feeder tube} / \text{nC s}^{-1}$$

Then:

$$\frac{I_T \text{ nC s}^{-1} \times 10^9 \text{ C nC}^{-1}}{\dot{m}_{\text{Samp}} \text{ mg s}^{-1} \times 10^{-6} \text{ kg mg}^{-1}} = Q_M \text{ C kg}^{-1} \quad (1.1)$$

Where Q_M is charge to mass ratio ($C\text{ kg}^{-1}$), which is the ratio of the charge imparted to the target, to the mass of particulate impacting the target.

Using the relationship between the impacting airflow speed (derived from the high-pressure airflow pressure) and Q_M , the charging behaviour of different target material - sample particulate material combinations could then be investigated

2.5 Airflow Speed Calibration.

The velocity of the flow, from the high-pressure air supply nozzle (Figure 12) against the target, was measured at each of the seven pressure settings used during the experiments. This was carried out using a custom-built relative pressure sensor unit supplied by PSG and Associates, Redlands, CA, USA. The sensor PCB was packaged into a standard plastic enclosure (Figure 30), and a pitot pressure probe was manufactured from a section of brass tube in accordance with the guidance of PSG Associates. The pitot probe was connected to the sensor Hi port using silicon tube, and the static side of the sensor was open to atmosphere.

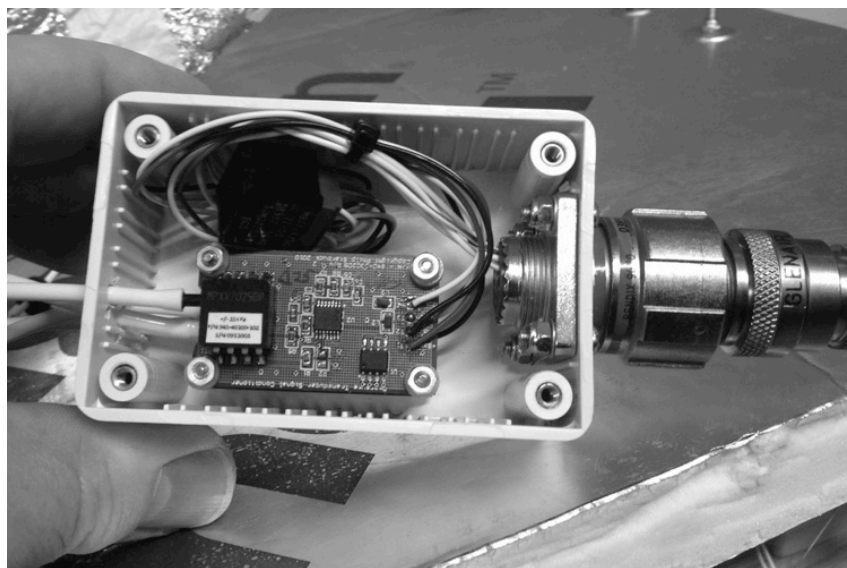


Figure 30 - PSG Associates relative pressure sensor PCB installed in enclosure.

A target example was manufactured with drilled holes in a grid pattern to allow the pitot probe to pass through (Figure 31). The drilled target was installed into the test enclosure in the normal way (Figure 103).

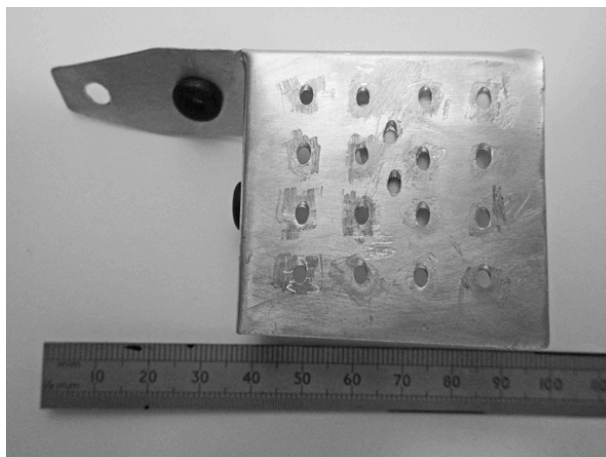


Figure 31 - The airspeed calibration target showing the drill pattern to accept the pitot probe.

The pitot probe was inserted through matching drilled holes in the upper surface of the test enclosure in such a way as to keep the probe parallel to the directed airflow, that is, at 45° to the target face (Figures 32 and 33).

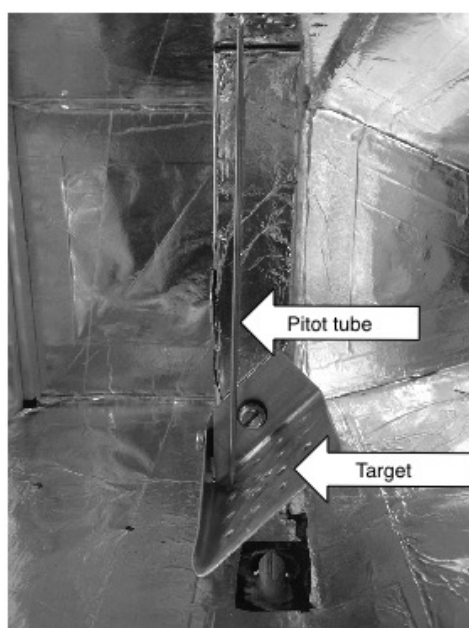


Figure 32 - The pitot probe and calibration target installed in the test enclosure.



Figure 33 - A detail view of the pitot probe installed and projecting through the target.

This arrangement was chosen for the following reasons: (a) we wished to understand the incoming airflow velocity and it was considered that the normal pressure on the face could be calculated if required, (b) it was considered that this alignment would also allow calculation of the flows along the target face if required, (c) it was considered that due to the proximity of the target to the high-pressure

nozzle, this alignment was more likely to detect flow reversals expected at the target edges.

The experimental rig was configured for an experimental test run, including the vacuum extraction system. The 0.5 – 4.5 VDC relative pressure sensor output was fed in to a Picoscope 2002 USB laptop based oscilloscope and the output signals captured and recorded using Picoscope 6 software and saved in picoscope format (.psdata). The sampling rate was set to 2 KHz and the range to ± 5 V. The compressed airflow was initiated and a relative pressure measurement recorded for approximately 10 seconds at each target grid point for each airflow pressure setting (10 grid points x 7 pressure settings = 70 recordings). Each grid point and pressure setting was sampled twice to measure repeatability.

2.5.1 Output processing, limits of sensor performance and calibration

The raw pressure data were processed in Picoscope to comma-separated format, then imported into Igor Pro V6 software. The sensor specification indicates a maximum mechanical response frequency of 500Hz, but notes sensor noise can exist from 500Hz to 1 MHz (Freescale Semiconductor, 2005), and recommends filtering of the signal on a rolling average basis of up to 64 samples. Therefore the signal wave was smoothed using a centre-point box averaging function, with 35 points found to produce a suitable response. A section of smoothed stable recording was selected from each data set and the “*wavestats*” function was used to generate an average output voltage value, a standard deviation value, a minimum voltage value and maximum voltage value for each point on the target for each airspeed tested. These data were then used to calculate and plot the velocity profile across the target and assess the degree of turbulence in the flow.

The device was based upon the Freescale MXVP7007 Integrated silicon pressure sensor. The sensor output is in the range 0.5 V to 4.5 v (4.0 V full scale span (FSS)) and the sensor output voltage is defined by the transfer function (Freescale Semiconductor, 2012);

$$V_{out} = V_s \times (0.057P + 0.5) \quad (1.2)$$

Where:

V_{out} is the sensor output (V),

V_s is the supply voltage (typically 5 V) and

P is the input pressure (KPa).

Rearranging (1.2):

$$P = \frac{\left(\frac{V_{out}}{V_s} - 0.5 \right)}{0.057} \quad (1.3)$$

Converting the pressure P to an airspeed can be achieved using the function for airspeed instrument calibration given by the United States Experimental Aircraft Association (EAA) (Erb, 1994) (equation (1.4))

$$V_c = \sqrt{\left(\frac{1}{\rho_{SL}} \right) 7 P_{SL} \left[\left(\frac{\Delta P}{P_{SL}} + 1 \right)^{\frac{2}{7}} - 1 \right]} \quad (1.4)$$

Where:-

v_c is calibrated airspeed (ft sec⁻¹),

ρ_{SL} is the density of air at sea level (0.0023769 slug ft⁻³) and

P_{SL} is the pressure of air at sea level (2116.22 lb ft⁻²).

In order to utilise the EAA function, the measured sensor output given in KPa was converted to lb ft⁻² (1 KPa = 20.885434 lb ft⁻²). The airspeed resulting from equation (1.4) is given as ft s⁻¹ and is then converted to knots and m s⁻¹.

The sensor specification quotes a wide error band of ± 0.5 KPa (Freescale Semiconductor, 2012) which was considered excessive. Therefore we used the supplied PSG Associates calibration data to improve accuracy. The sensor zero airspeed point was measured at 2.5001 V, which results in a supply voltage of 5.002 V. A table of theoretical sensor output voltage against input airspeed (pressure) was then created using equations (1.3) and (1.4) (Appendix L). These data were then plotted and compared to the calibration values measured by a pitot/static test set supplied by PSG and Associates.

2.6 Sample feeder draw-wire system calibration.

As stated in § 2.4 the mass delivery rate was calculated as an average based upon drive on time and measured mass used. However it was considered necessary to assess the linearity and variability of the drive system in the voltage range used.

The drive system was run at 6 V to 12 V in 1 V increments and the time recorded to travel 200 mm recorded in 50 mm intervals using a stopwatch. Each drive voltage was tested three times and the results plotted.

3 Results.

The results sets consist of the following data groups:-

- i. Calibration data for the airflow velocity.
- ii. Calibration data for the mass delivery system.
- iii. Charge to mass ratio (Q_{Mv}) data for the impact of E15 ash against the three metallic targets at seven airflow velocities (four samples per velocity per target).
- iv. Charge to mass ratio (Q_{Mc}) data for the impact of E15 ash against the aluminium metallic target at one airflow velocity (28 samples taken at the start and end of day testing to act as controls).
- v. Charge to mass ratio (Q_{Mr}) data for the impact of E15 ash against the three metallic targets at four mass delivery rates (four samples per velocity per target).
- vi. Charge to mass ratio data (Q_{Mf}) for the lofting of E15 ash from the brass feeder system at seven airflow velocities.
- vii. Charge to mass ratio data (Q_{Mv}) for the impact of Ballotini™ against the three metallic targets at two airflow velocities (two samples per velocity per target).
- viii. Charge to mass ratio (Q_{Mv}) data for the impact of sand against the aluminium target at two airflow velocities (two samples per velocity per target).
- ix. Charge to mass ratio (Q_{Mv}) data for the impact of SAK ash against the aluminium targets at two airflow velocities (two samples per velocity per target).
- x. Qualitative data for the impact of ice against the aluminium target at one airflow velocity
- xi. The grain size distribution of the E15 ash, sand and SAK ash.

These results sets are documented, following the order shown above, in the following sections.

3.1 Airflow Velocity Calibration

3.1.1 Accuracy of the sensor.

Section 2.5.1 detailed the need to compare the theoretical output of the PSG airspeed sensor as calculated by the transfer function, to the actual performance of the sensor as tested by PSG using a bench pitot / static test set. The transfer function for output voltage against input pressure was calculated and is shown in Appendix L. The test data supplied by PSG were specific to the sensor used in the experiment and reflect a measured voltage output for a calibrated pressure input. These two data sets were overlain in order to assess the performance of the experimental sensor in comparison to theory. The result is shown in Figure 34. It can be seen that the measured performance of the sensor was extremely close to the theoretical transfer function results, and therefore it was considered valid to neglect the manufacturers ± 0.5 K Pa error band for the determination of accuracy. Airspeed accuracy would therefore be determined from the calibration carried out on the experimental rig. Also, due to the wide distribution of flow speeds as shown in the results of the flow measurements described in 3.1.2, it was considered valid to neglect any errors between the pitot static data and theoretical data and assume the transfer function as the input / output reference.

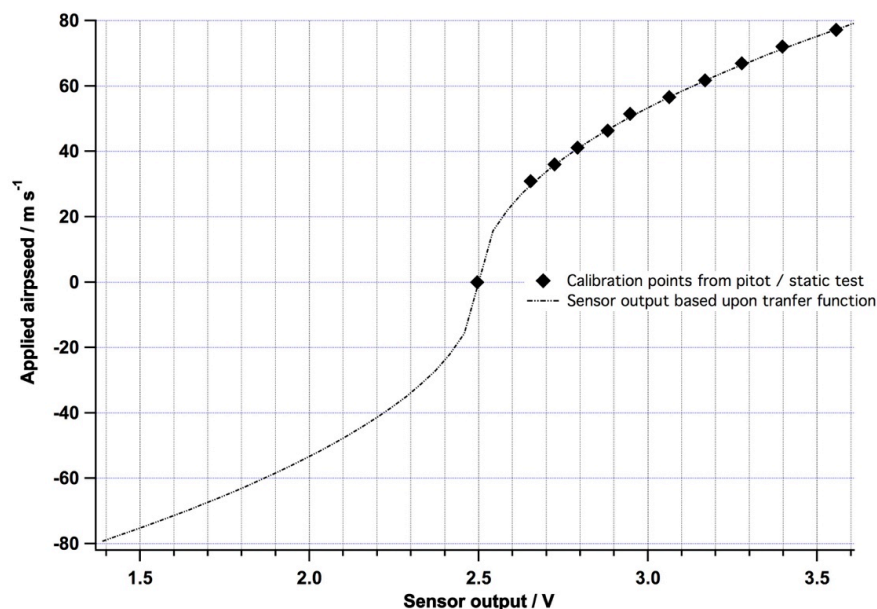


Figure 34 - Comparison between the theoretical output of the PSG airspeed sensor as calculated by the transfer function (Freescale Semiconductor, 2012) and the actual output as tested using a pitot / static test set.

3.1.2 Measured pressures at the target face

A sample of a smoothed pressure sensor output signal as generated by the procedure in section 2.5 is shown in Figure 35. This particular sample shows the pressure signal measured at the target face oscillates between approximately 3.0 V and 3.6 V, with an average value of approximately 3.3 V. This level of variability was seen at all pressure values of the high-speed flow, to differing extents. In order to assess this variability, and to validate the use of the 'waviestats' function in IgorPro, histogram distributions of the signal data were produced from the data collected at 40 psig, 55 psig and 70 psig high-pressure flow settings. The histograms were binned at the digitization value of 0.011 V per bin, with 9000 individual readings in each dataset. The results are shown in Figure 36. It can be seen that mean pressure is a valid value to use as the distribution is normal, however the spread of pressure values increases with increasing air supply pressure. This is attributed to turbulence in the nozzle and across the face of the target. Taking these data into account it is felt that the values obtained using the 'waviestat' function in IgorPro are valid and that airspeed should be calculated using the mean output values with an error boundary of ± 1 standard deviation as calculated by the 'waviestat' function.

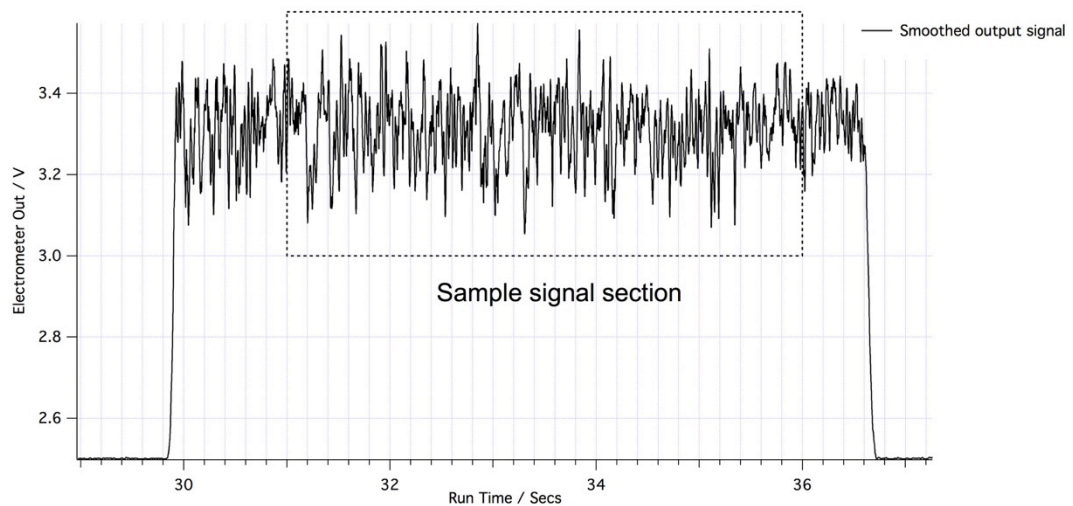


Figure 35 - A sample output signal from the PSG pressure sensor during an airspeed calibration test. The recording has been smoothed to remove high frequency noise.

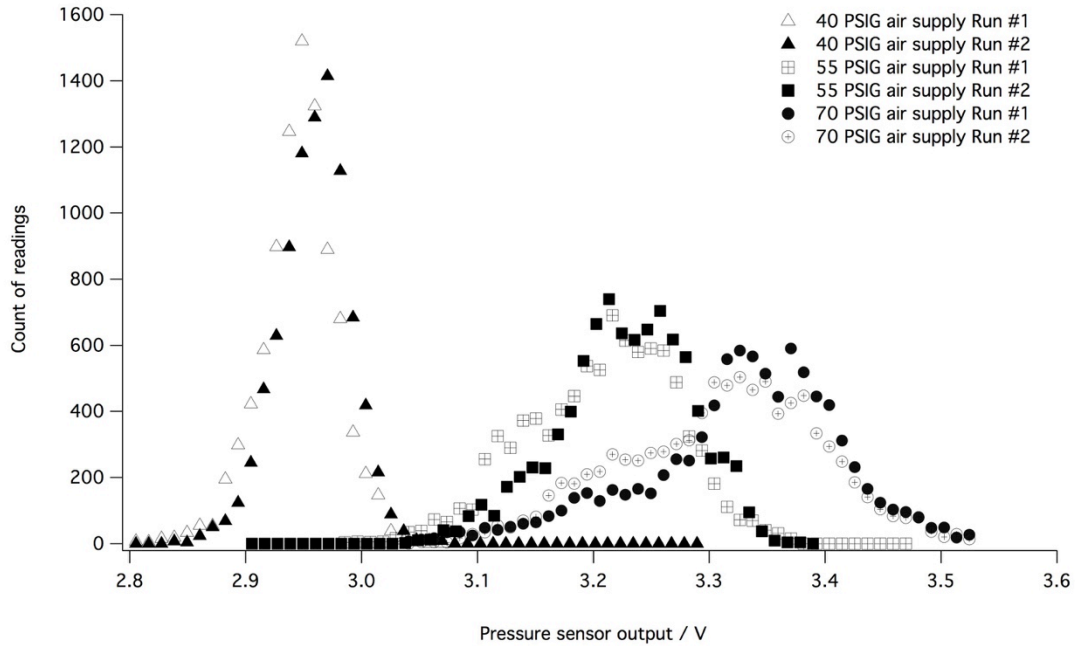


Figure 36 - Histogram of the recorded data from the PSG pressure sensor showing the data spread at three high pressure air supply values. Data points are binned at 0.011V intervals; each dataset has 45 bins and 9000 data points. The data sets were collected at 40, 55 and 70 psig,

3.1.3 Converting the target face pressures to airflow velocity

The data from the calibration tests was processed in accordance with the procedure in section 2.5 and the results are shown in Figure 37 with the error bands at ± 1 sd shown as defined from the discussion in the previous section.

The best-fit lines appear to follow a power law equation of the form:

$$v_{P_{hpa}} = a + bP_{hpa}^x \quad (1.5)$$

where:

$v_{P_{hpa}}$ is the airflow velocity / ms^{-1} ,

P_{hpa} is the the high-pressure airflow set pressure / psig and

a , b and x are calculated coefficients.

The equation coefficients given from IgorPro are shown in Table 4.

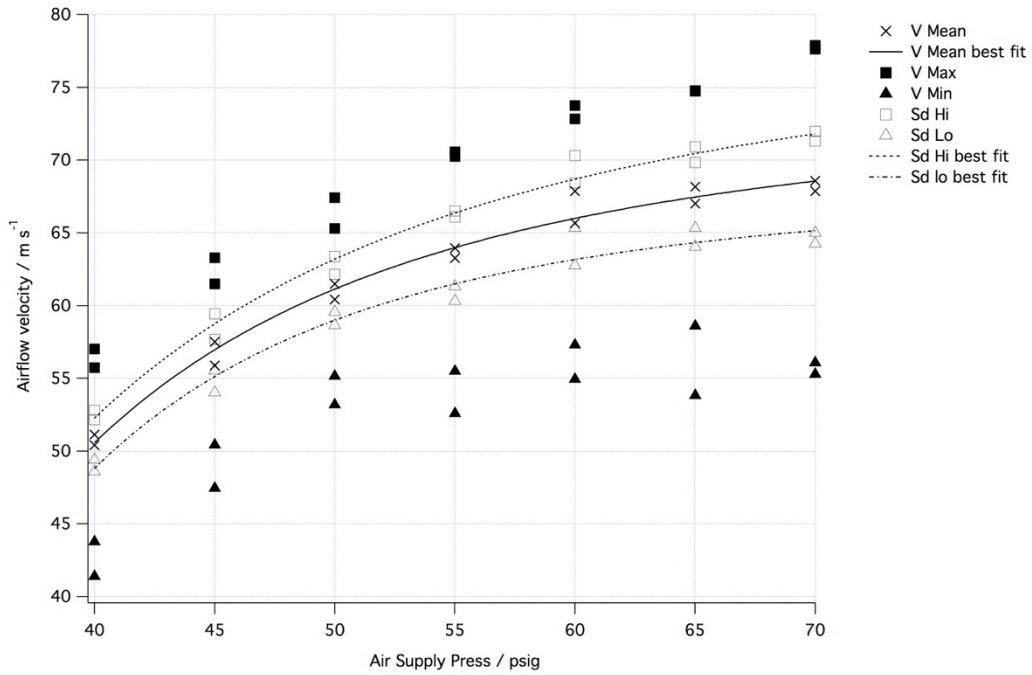


Figure 37 - Calibration curves for airflow velocity vs. high-pressure air supply pressure.

Table 4 - Table of coefficients for the airspeed calibration curves shown in figure 37 and detailed in equation (1.5).

Curve from Figure 37	<i>a</i>	<i>b</i>	<i>x</i>
V Mean best fit	73.28	-7.0344×10^5	-2.8032
Sd Hi best fit	79.149	-1.3907×10^5	-2.3224
Sd Lo best fit	68.071	-4.85×10^6	-3.3712

Using the data from the curves shown in Figure 37, the equation (1.5) and the coefficients in Table 4 the flow velocities used for the experimental results were calculated and are shown in Table 5 along with the error bounds.

Table 5 - The high-speed flow pressure setting / airflow speed calibrated results table. Mean airflow velocity is to 3 sf and errors are to 2 sf.

High-pressure flow pressure setting / psig	Mean airflow velocity / ms ⁻¹	Airflow velocity Hi variability (1 sd) / ms ⁻¹	Airflow velocity Lo variability (1 sd) / ms ⁻¹
40	50.7	2.1	1.8
45	57.0	2.1	1.8
50	61.1	2.3	2.1
55	64.0	2.5	2.5
60	66.0	2.8	2.8
65	67.5	3.1	3.1
70	68.6	3.4	3.4

3.1.4 The airflow velocity distribution across the target

As detailed in § 2.5 and shown in Figure 31 the pressure, and hence airflow velocity, was measured across the face of the target. This was plotted as a contour using 64 bit interpolation in Igor Pro, and then overlain onto digital images of the aluminium target to assess the velocity distribution and its alignment to the target and the erosion zone. The erosion zone can be seen as an area on the face of the target with a matt surface finish as opposed to the bright polish surface of the raw material. This surface matt effect was seen on all targets. The results are shown in Figures 38 and 39 and indicate that the erosion zone is aligned with the high flow speed contours. It is also shown that the highest velocity values are tightly constrained within the centre of the high-speed flow impact area, the centre of the target being aligned over the centre of the high-speed airflow nozzle. The velocity profile rapidly reduces radially from the centre and it can be seen that toward the lower, left hand and right hand edges of the target (Row 1 and column D and A) the flow actually reverses and is negative. The flow is positive to the upper edge.

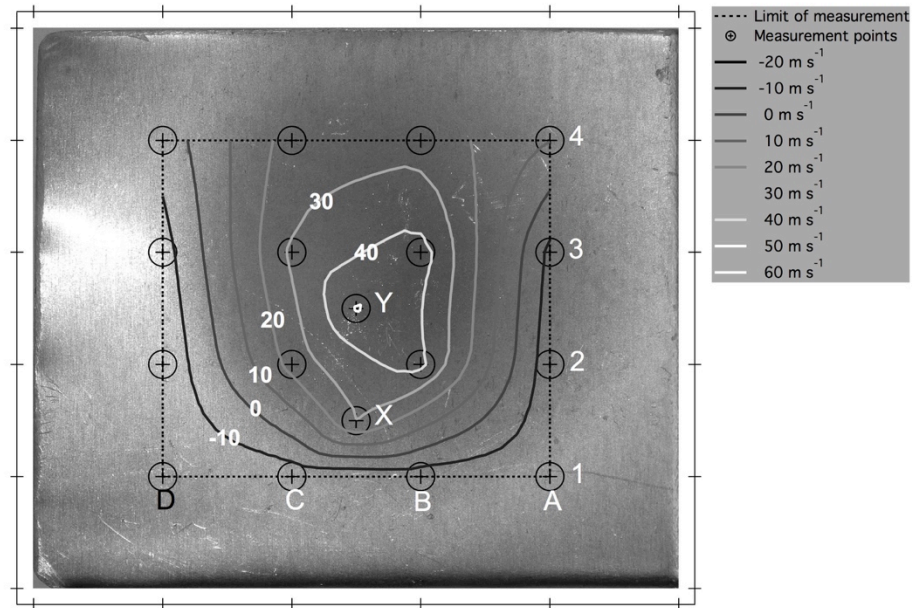


Figure 38 - Airflow velocity contour on the target face (High-speed flow pressure 40psig) overlain on an image of the aluminium target. The erosion zone of the target can be seen as a darker central area.

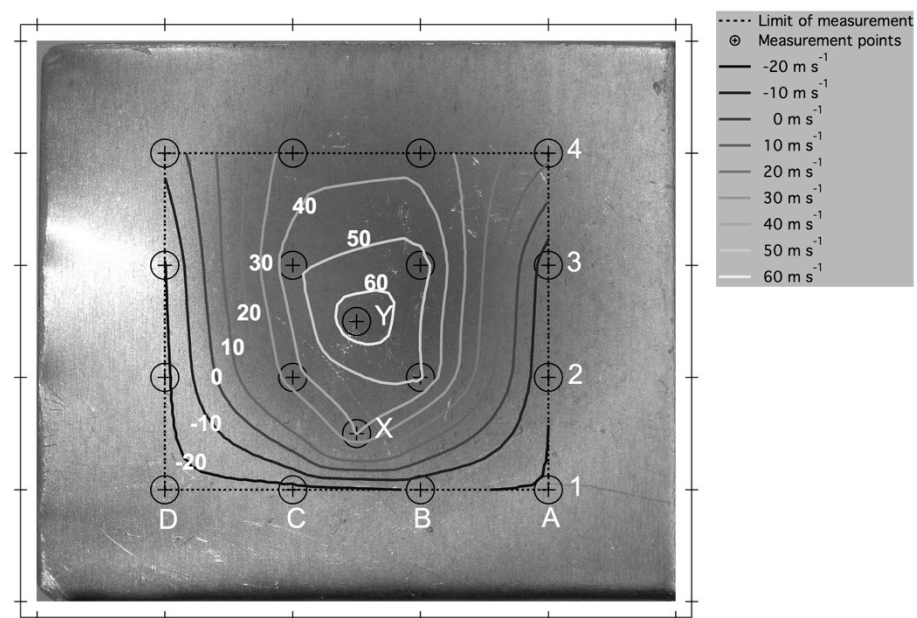


Figure 39 - Airflow velocity contour on the target face (High-speed flow pressure 70psig) overlain on an image of the aluminium target. The erosion zone of the target can be seen as a darker central area.

3.2 Sample feeder draw-wire system speed calibration, and mass delivery system accuracy.

The results of the timed pulls of the sample drawer wire drive system are shown in Figure 40. The results demonstrated a linearity of $\pm 2\%$.

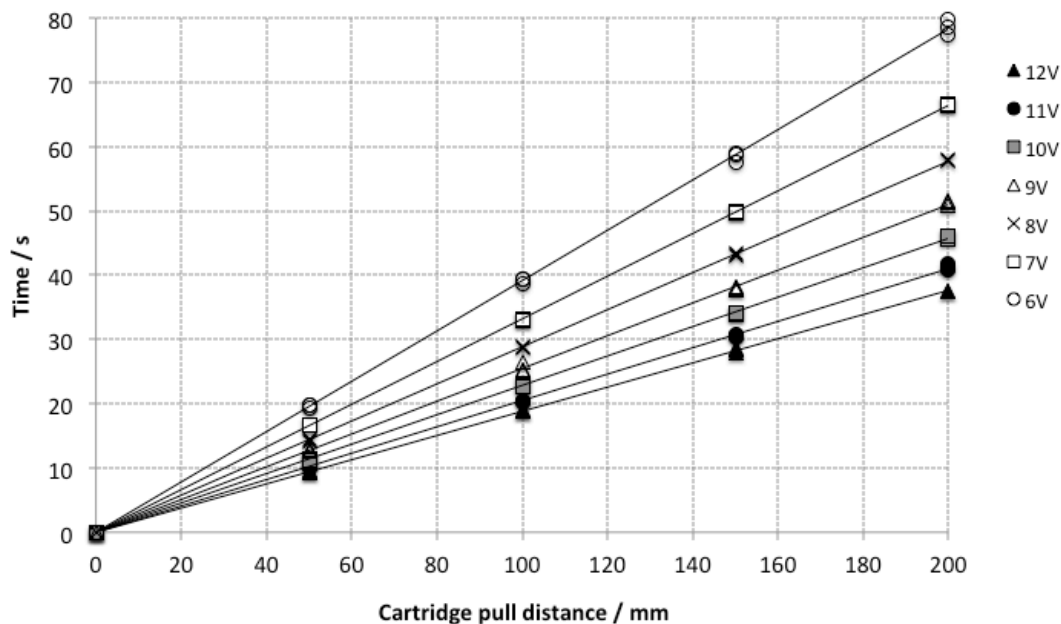


Figure 40 – Graph of cartridge pull distance vs. time for the sample drawer wire drive system at various motor drive voltages.

The weighing of the sample cartridge was carried out on a scale of accuracy ± 0.001 g, suggesting an error bound of ± 0.0005 g. However it was found that, due to the length of the cartridge and laboratory air currents, the stability of the scale was such that accuracy could only be stated to ± 0.001 g for the start and end weight.

3.3 Charge to mass ratio of Eyjafjallajökull ash impacting the metallic targets at varying velocity (Q_{Mv}).

The charge to mass ratio (Q_{Mv}) calculated as per § 2.4 is shown in Figures 41, 42 and 43. The error limits have been derived from § 3.1 and § 3.2. The data, although widely spaced and with significant error bars, appear to best fit a curve of sigmoid general form and using a Boltzman equation of the form:

$$y = b + \left\{ \frac{a - b}{1 + \exp \frac{x_{mean} - x}{\max \frac{dy}{dx}}} \right\} \quad (1.6)$$

where:

b is min y value,

a is max y value,

x_{mean} is the x value at 50% of the a to b value and

$\max dy/dx$ is the maximum slope value.

The values of the coefficients a , b , x_{mean} and $\max dy/dx$ are shown in Table 6.

However it was considered necessary to adjust these data due to the findings of the control run data as described in § 3.4.1.

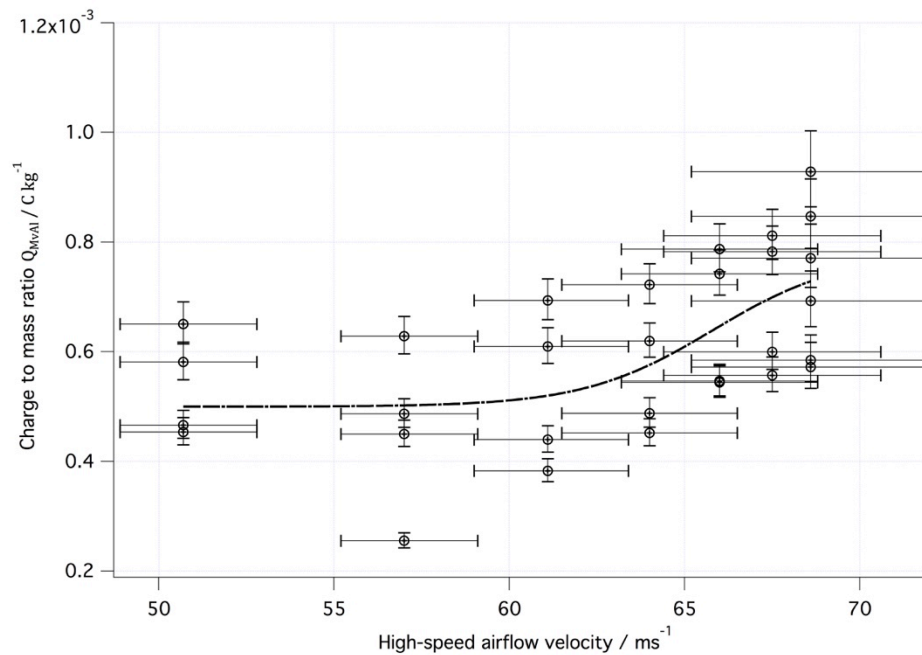


Figure 41 - The charge to mass ratio for E15 ash impacting an aluminium target (Q_{MvAl}) at varying velocities. The “best fit” curve is shown dashed.

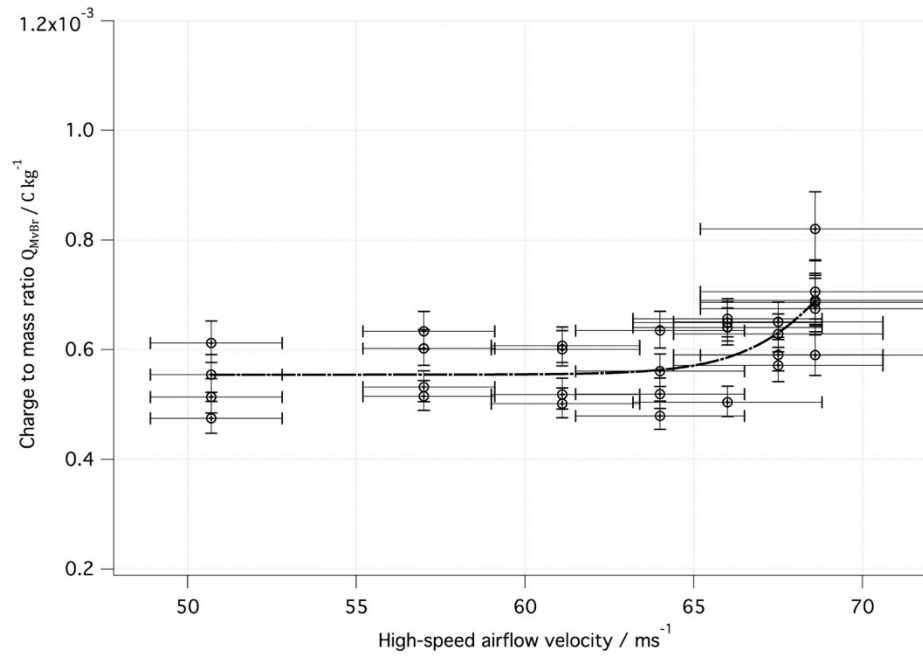


Figure 42 - The charge to mass ratio for E15 ash impacting a Brass target (Q_{MVBT}) at varying velocities. The “best fit” curve is shown dashed

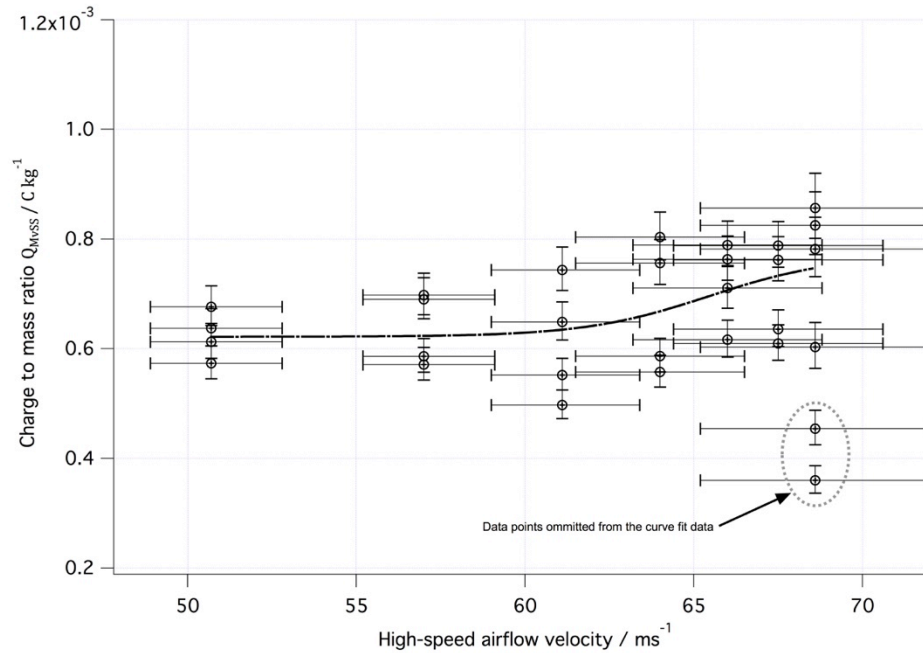


Figure 43 - The charge to mass ratio for E15 ash impacting a stainless steel target (Q_{MVSS}) at varying velocities. The “best fit” curve is shown dashed – NOTE that two points considered as outliers from experimental notes have been excluded from the best fit and are shown.

3.4 Charge to mass ratio of Eyjafjallajökull ash impacting the aluminium target (Q_{Mc}) at constant velocity of 61 ms^{-1} (50Psi high-speed flow pressure) – experimental controls.

The charge to mass ratio results (Q_{Mc}) of the 28 control tests gathered at the start of day and end of day (as detailed in 2.3) are shown in Figure 44 grouped by day. The calculated mean of $5.67 \times 10^{-4} \text{ C kg}^{-1}$ (Sd $0.95 \times 10^{-4} \text{ C kg}^{-1}$) is shown dotted.

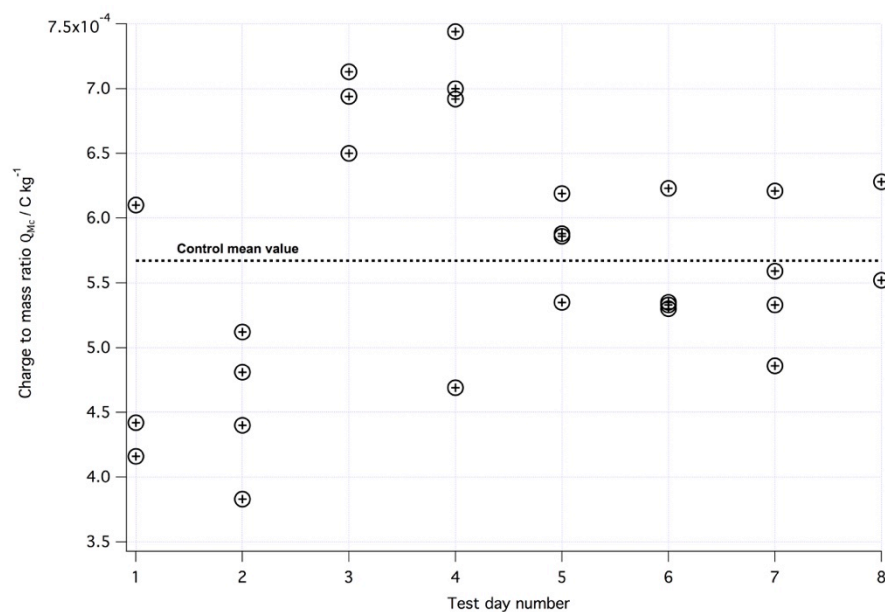


Figure 44 – Charge to Mass ratio (Q_{Mc}) of the 28 control tests, sorted by day number of the test sequence. The mean value is shown as a dotted line.

The spread of the control tests, approximately 3.8 to 7.5 C kg^{-1} , is almost as wide as the total signal variation seen across the varying velocity tests in 3.3. However some pattern in terms of the time location of the control tests was noticed. The tests were gathered over eight days of tests, and normally two control tests were collected at the start of testing for the day, and two at the end of the test period. The variation from the mean value for each test was grouped into bins for the capture period, start-of-day or end-of-day. The results are shown in Figure 45, which reveals a positive variation from the mean for those controls captured at the start-of-day, and a negative variation from the mean for those captured at the end of day. The mean of the start-of-day data (excluding the negative value outliers) is $5.9 \times 10^{-5} \text{ C kg}^{-1}$ (sd of

$6.3 \times 10^{-5} \text{ C kg}^{-1}$), and the mean of the end-of-day data is $-6.5 \times 10^{-5} \text{ C kg}^{-1}$ (sd of $4.9 \times 10^{-5} \text{ C kg}^{-1}$). The difference between the means being $12.4 \times 10^{-5} \text{ C kg}^{-1}$, is in the order of two standard deviations. A t-test confirms a p value of 0.93 confirming the data sets represent a clear difference between the start-of-day controls and the end-of-day controls. This suggests a drift occurring through the test period from positive to negative. It could also be seen that individual days would be biased positive or negative (see Figure 44)

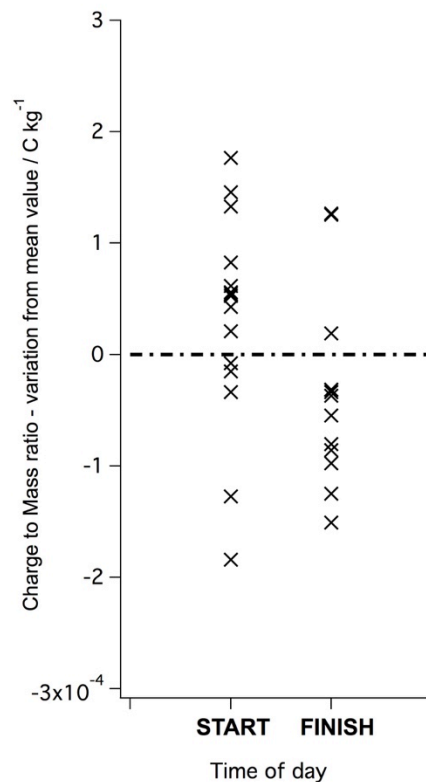


Figure 45 - The variation from the mean of the control test values of Charge to mass ratio Q_{Mv} , grouped by capture period.

3.4.1 Applying the control data to the results shown in 3.3

Using the control data from above as a basis for estimating the drift of measurements, the data shown in 3.3 were adjusted by introducing a modifier accounting for the possible offset of the data set from the mean, and the offset due to drift within the day. The assumptions made for this methodology were; (a) an offset of the control data suggests the data between the control runs will also be offset and

(b) the drift within the dataset, between the day start high and the end of day low, occurred from the maximum value to the minimum value linearly throughout the day.

The offset adjustment value for each data point was calculated as follows:

- i. The mean of the control data for the day of the datapoint was calculated as;

$$\text{day control mean} = \frac{\text{control max} + \text{control min}}{2}$$

- ii. The offset of the control data for the day of the datapoint was calculated as;

$$\text{day control offset} = \text{day mean} - 5.67 \times 10^{-4}$$

- iii. This offset was then applied to the max control datapoint to find a normalized day control max value i.e. the theoretical control max if the data was centred around the control mean.

$$\text{Normalised control max} = \text{control max} - \text{day offset}$$

- iv. The drift per run of the day set was calculated as;

$$\text{drift} = \frac{\text{control max} - \text{control min}}{\text{number of runs in day}}$$

- v. The theoretical offset of the datapoint was then calculated as;

$$\text{datapoint offset} = \left[\text{normalised control max} - (\text{drift} \times \text{run number}) \right] - (5.67 \times 10^{-4})$$

- vi. This offset was then applied to the charge to mass value for the specific datapoint. Each datapoint was calculated individually.

The resulting changes to the data shown in § 3.3 are shown in figures 46, 47 and 48. Those data also had best fit curves attached of sigmoid form using the Boltzman equation.

The values for the Boltzman equation coefficients for these data and the previous base data are shown in Table 6. It can be seen from that table that the base value b is reasonably well constrained for all three targets, whereas the maximum value a is only constrained within useable limits for the aluminium target. Similarly, due to the max values being poorly constrained, the gradient and 50% (x_{mean}) values are also quantitatively unusable.

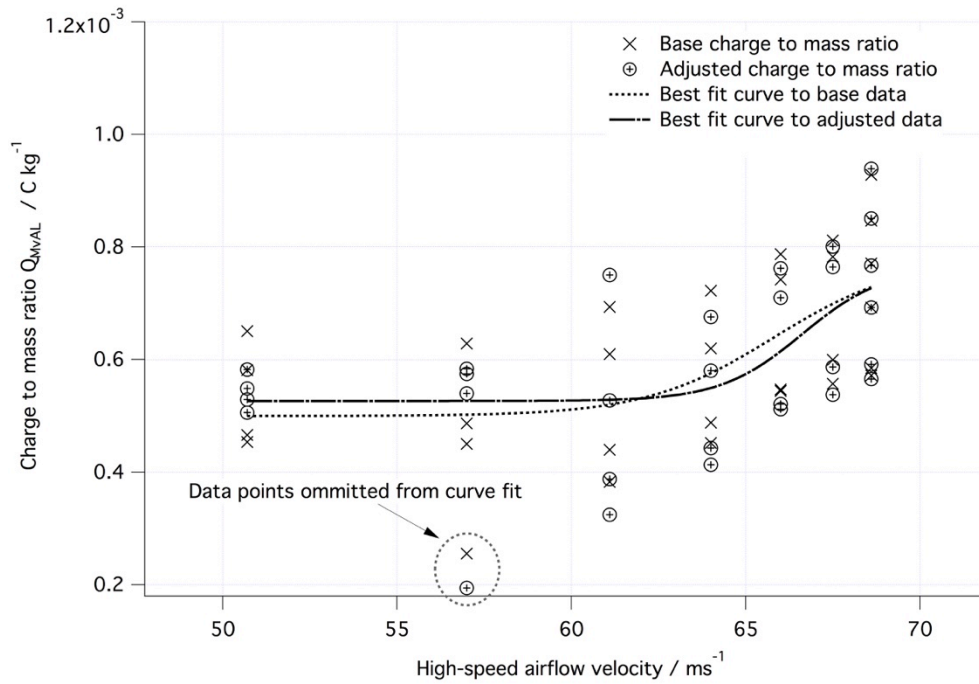


Figure 46 - The charge to mass ratio for E15 ash impacting an aluminium target (Q_{MVAL}) with data points adjusted for control variation (error bars not shown for clarity).

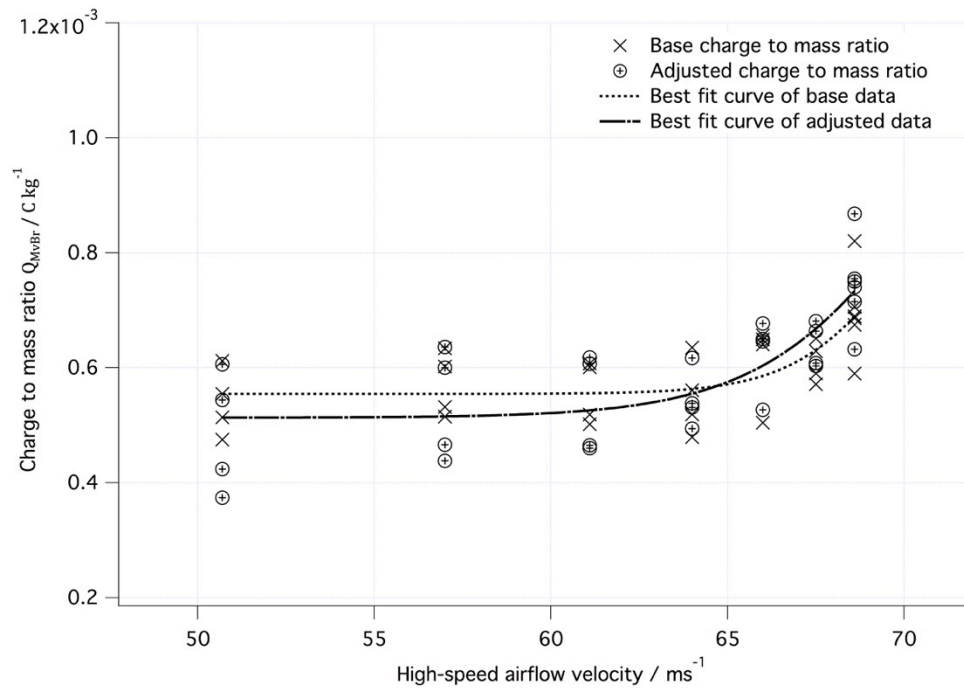


Figure 47 - The charge to mass ratio for E15 ash impacting a brass target (Q_{MVBr}) with data points adjusted for control variation (error bars not shown for clarity).

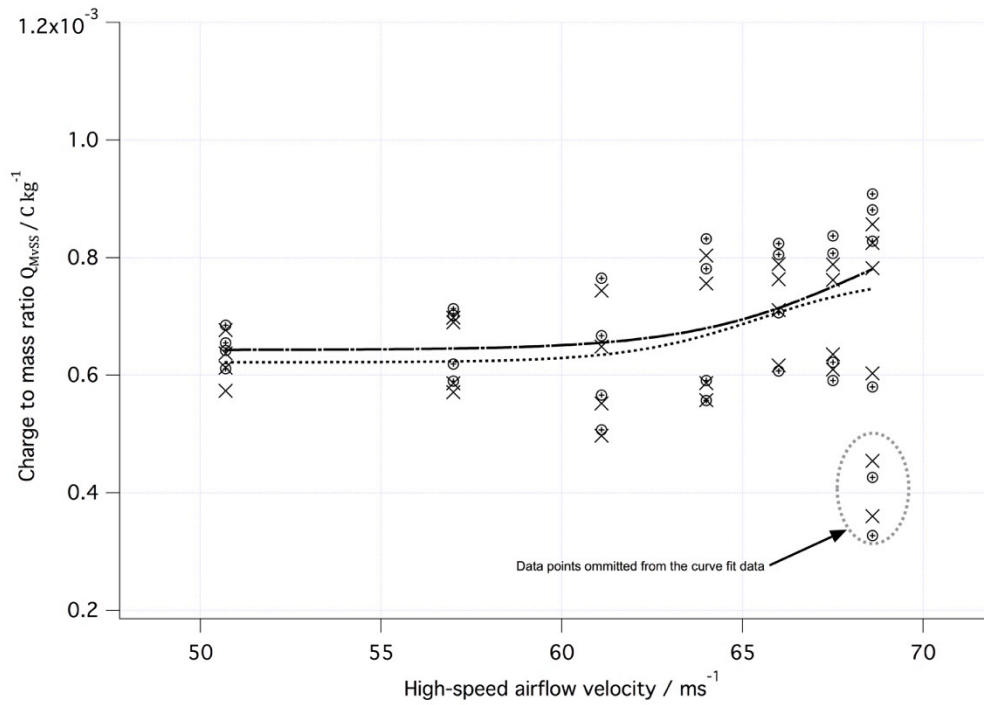


Figure 48 - The charge to mass ratio for E15 ash impacting a stainless steel target (Q_{MvSS}) with data points adjusted for control variation (error bars not shown for clarity).

Table 6 - Coefficients of the Boltzman sigmoid equation best fit curves of QMv against airflow velocity shown in Figures 41 to 43 and Figures 46 to 48.

Target	Coeff.	a	b	x_{mean}	$max dy/dx$
		$C kg^{-1}$	$C kg^{-1}$	$m s^{-1}$	$C kg^{-1} m^{-1} s$
Aluminium	Base	7.79×10^{-4} $\pm 2.8 \times 10^{-4}$	5.00×10^{-4} $\pm 4.8 \times 10^{-5}$	65.8 ± 4.1	1.85 ± 2.78
	Adj	7.64×10^{-4} $\pm 2.3 \times 10^{-4}$	5.26×10^{-4} $\pm 3.9 \times 10^{-5}$	66.6 ± 2.8	1.18 ± 1.94
Brass	Base	1.02×10^{-3} $\pm 3.7 \times 10^{-3}$	5.54×10^{-4} $\pm 1.9 \times 10^{-5}$	70.0 ± 19.2	1.51 ± 2.89
	Adj	1.31×10^{-3} $\pm 4.8 \times 10^{-3}$	5.13×10^{-4} $\pm 3.0 \times 10^{-5}$	70.9 ± 22.8	2.38 ± 3.42

Target	Coeff.	a	b	X_{mean}	$max dy/dx$
		$C kg^{-1}$	$C kg^{-1}$	$m s^{-1}$	$C kg^{-1} m^{-1} s$
Stainless steel	Base	7.70×10^{-4} $\pm 1.8 \times 10^{-4}$	6.22×10^{-4} $\pm 3.4 \times 10^{-5}$	65.5 ± 5.1	1.85 ± 3.54
	Adj	9.08×10^{-4} $\pm 1.3 \times 10^{-3}$	6.43×10^{-4} $\pm 4.3 \times 10^{-5}$	68.4 ± 22.9	2.43 ± 6.79

3.5 Charge to mass ratio of Eyjafjallajökull ash impacting the metallic targets at constant velocity but varying mass rates (Q_{Mr}).

The results of the data gathered of E15 ash impacting the three metallic targets at constant airflow velocity, but varying mass delivery rate, are shown in Figures 49, 50 and 51. The charge to mass ratio (Q_{Mr}) and error values were calculated as for previous data as detailed in § 3.2.

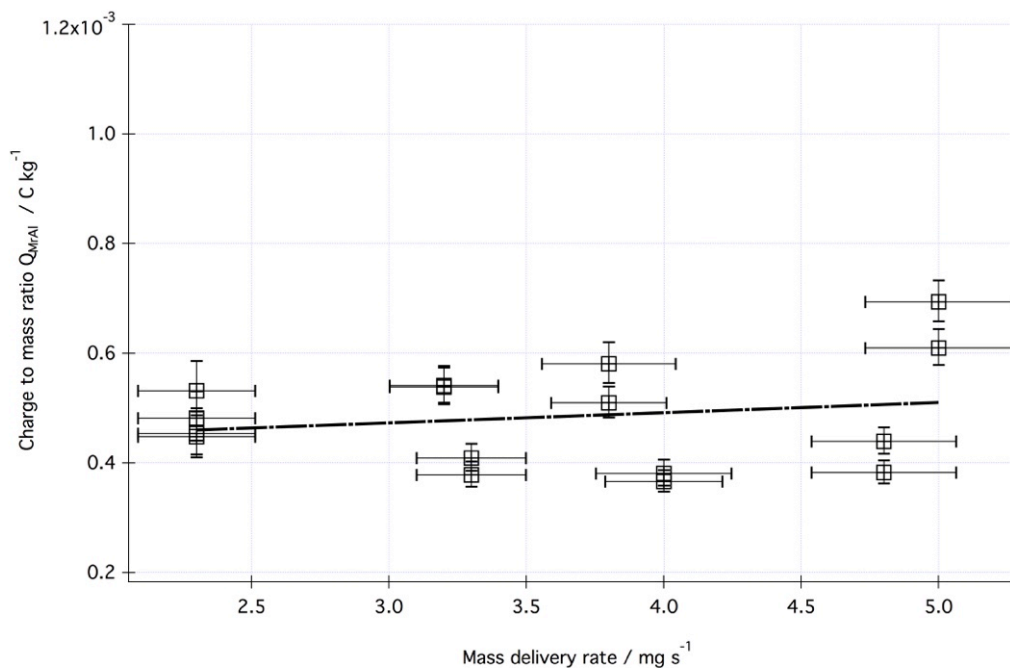


Figure 49 - The charge to mass ratio for E15 ash impacting an aluminium target (Q_{MrAl}) at varying mass delivery rates. The "best fit" curve is shown dashed.

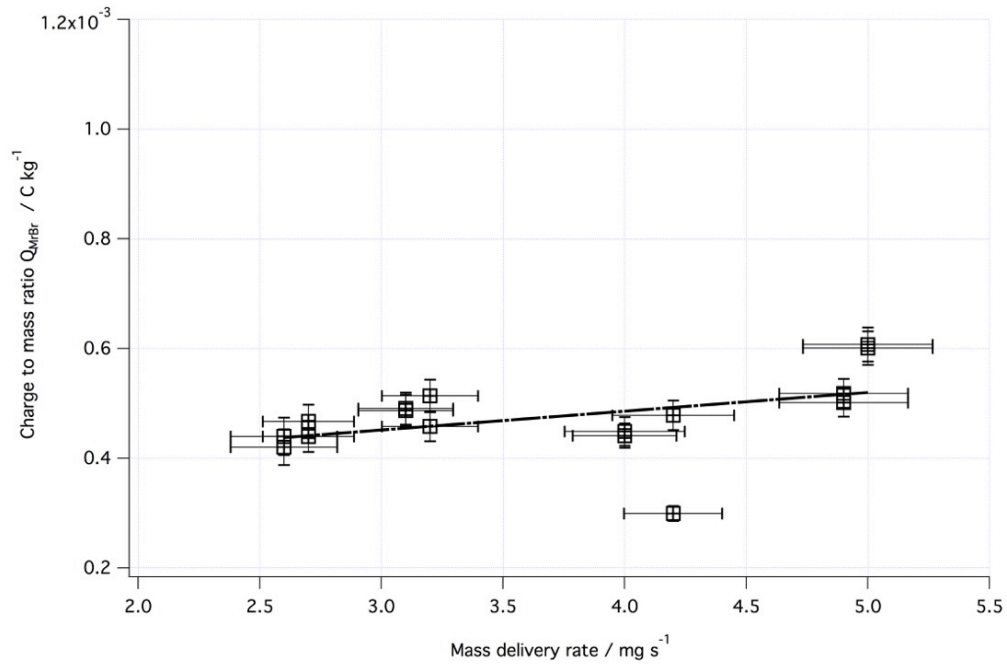


Figure 50 - The charge to mass ratio for E15 ash impacting a brass target (Q_{MrBr}) at varying mass delivery rates. The “best fit” curve is shown dashed.

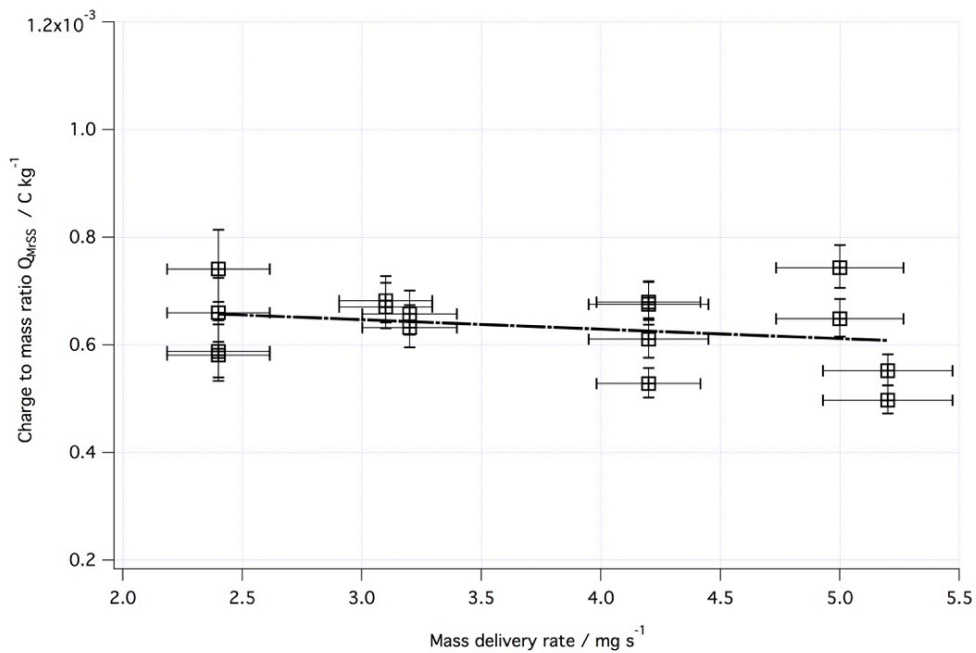


Figure 51 - The charge to mass ratio for E15 ash impacting a stainless steel target (Q_{MrSS}) at varying mass delivery rates. The “best fit” curve is shown dashed.

The base results were adjusted for the control data offsets as in 3.4.1 and the results are shown in Figures 52, 53 and 54

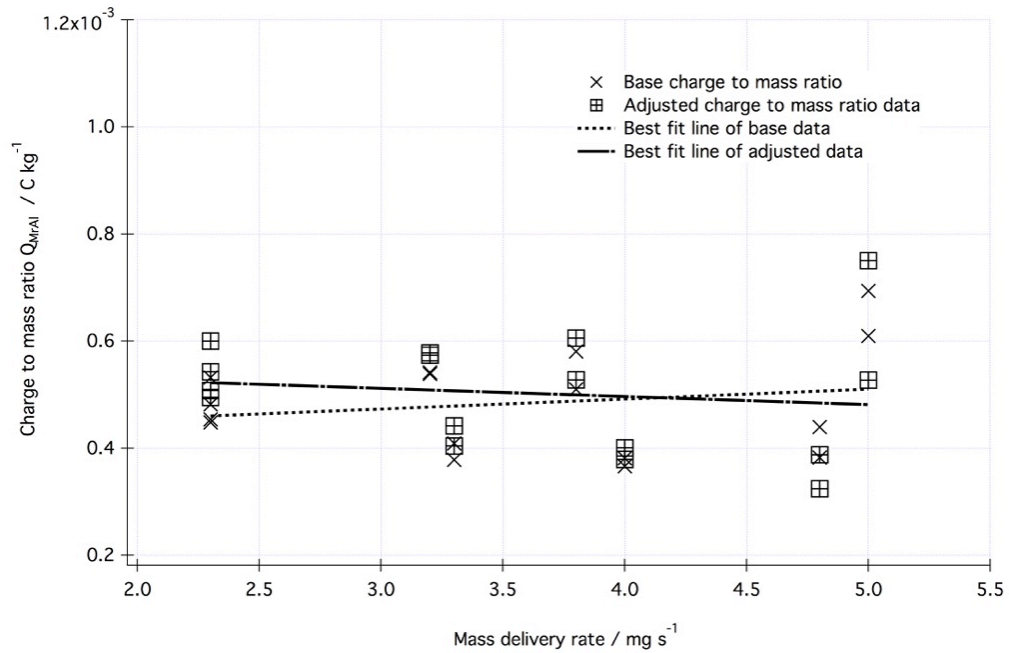


Figure 52 - The charge to mass ratio for E15 ash impacting an aluminium target at varying mass delivery rates (Q_{MrAl}) with data points adjusted for control variation (error bars not shown for clarity).

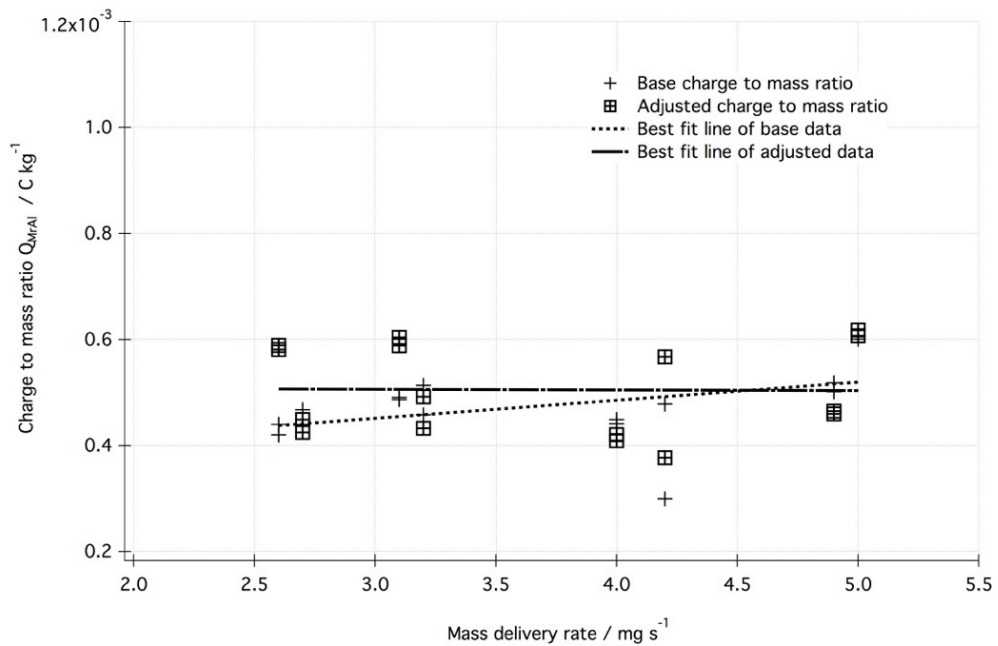


Figure 53 - The charge to mass ratio for E15 ash impacting a brass target at varying mass delivery rates (Q_{MrBr}) with data points adjusted for control variation (error bars not shown for clarity).

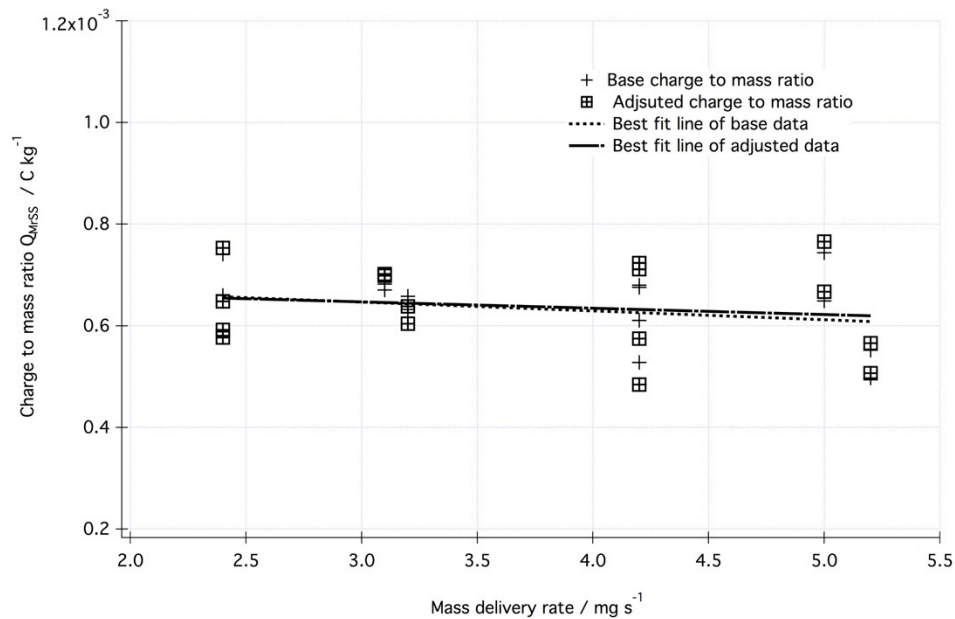


Figure 54 - The charge to mass ratio for E15 ash impacting a stainless steel target at varying mass delivery rates (Q_{MrSS}) with data points adjusted for control variation (error bars not shown for clarity).

It can be seen that, although the unadjusted data shows a possible positive or negative trend of Q_M , when the adjusted data is added to the analysis it would seem that Q_M remains approximately constant at all mass delivery rates. This means the absolute charging rate values obtained are linearly proportional to mass delivery rates.

3.6 Charge to mass ratio of Eyjafjallajökull ash leaving the side feeder tube at varying velocities (Q_{MT})

The charge deposited on the side feeder tube was measured in parallel with the target charges as described in the experimental setup (§ 2.2.4). As the feeder tube assembly remained unchanged for all versions of target and sample types, these data are analysed from two approaches: (a) comparing the feed tube charging rate with the target charging rate for experimental runs and (b) investigating the variability of the charging rate at the feeder tube. These results are restricted to the experimental data of E15 ash impacting the three target types.

It should be noted that although the high-pressure airflow velocity is shown, the actual velocity through the feed tube was not measured or quantified, and the

assumption is made that flow velocity in the feed tube increases with increasing high-pressure flow velocity. The use of the high-speed flow velocity is to align data collected in parallel. The charging values as given by the charge to mass ratio (Q_M), in this instance defined as Q_{Mf} , is shown in Figures 55 to 57. The data are aligned with the respective target data in order to make a comparison with target charging.

Feeder charging data were also collected in parallel during the 28 controls runs, and have been processed in exactly the same way as for the target charging control data (§ 3.4). The experimental data have then been adjusted for offset and drift from the control run findings in exactly the same way as the target data. The best-fit curves for the target data for each experimental set are shown in the results as a reference.

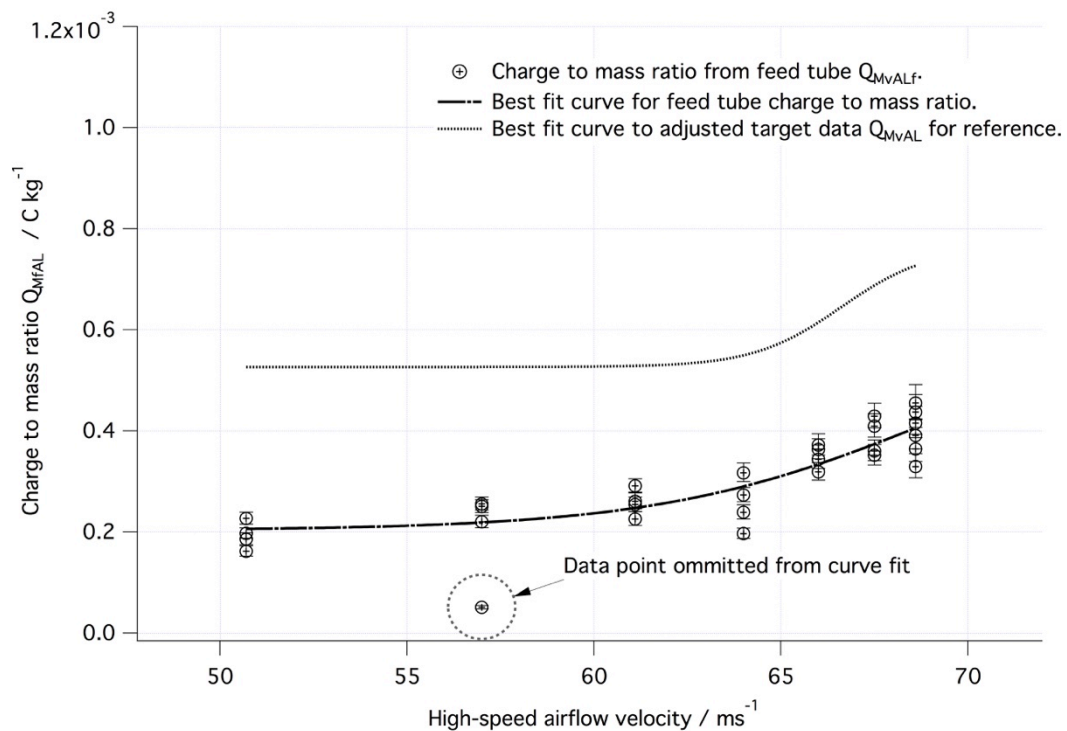


Figure 55 - Charge to mass ratio results for the side feeder during the E15 / Aluminium target experimental group. The results are aligned by the high-speed airflow velocity value. The feed tube velocity is unknown and therefore no x-axis error is shown. The target Q_{MVAL} best fit curve is shown for reference.

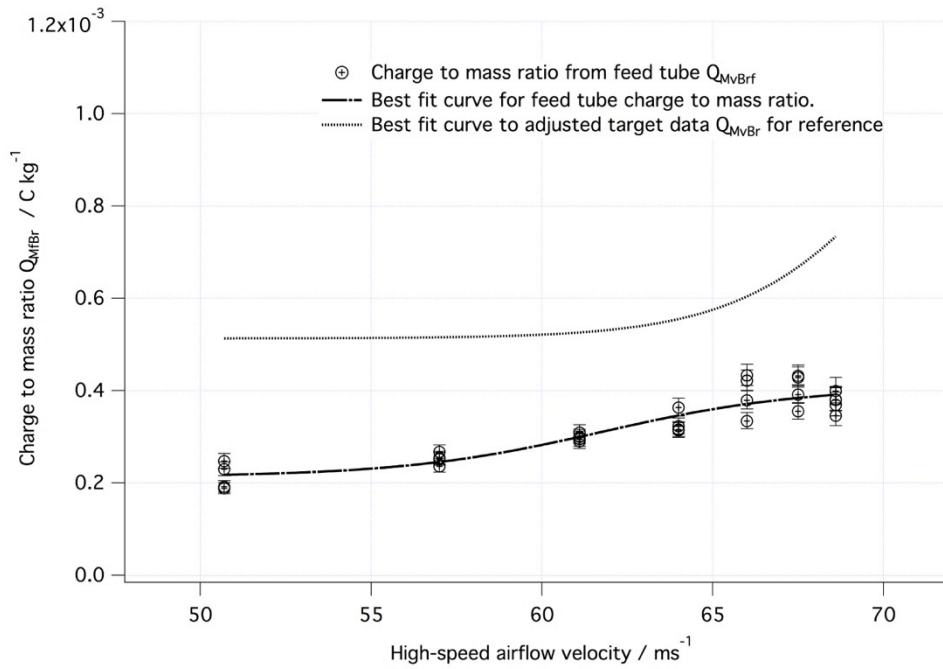


Figure 56 - Charge to mass ratio results for the side feeder during the E15 / Brass target experimental group. The results are aligned by the high-speed airflow velocity value. The feed tube velocity is unknown and therefore no x-axis error is shown. The target Q_{MvBr} best fit curve is shown for reference.

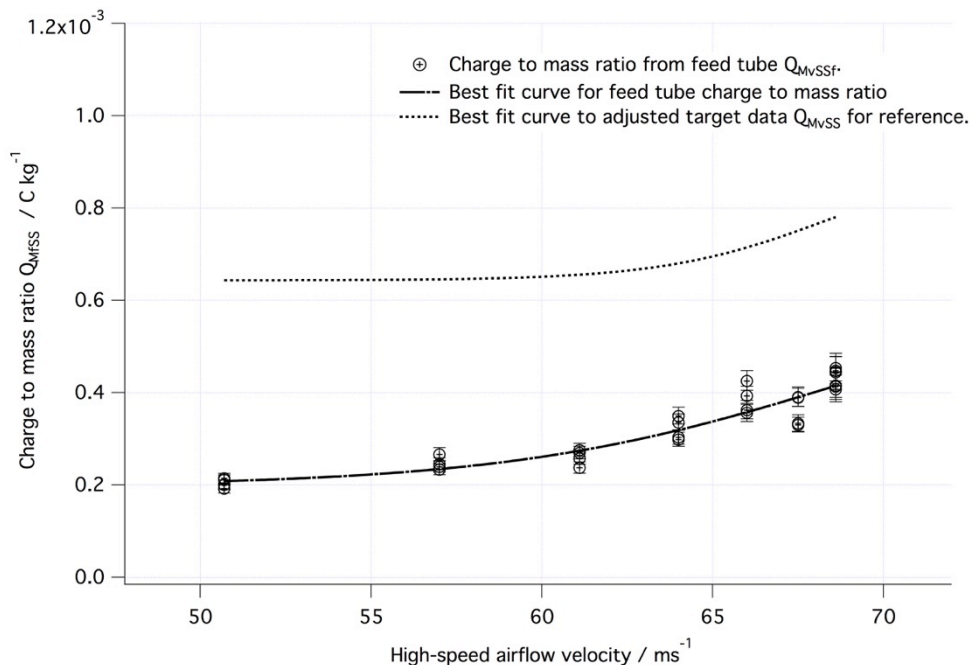


Figure 57 - Charge to mass ratio results for the side feeder during the E15 / Stainless steel target experimental group. The results are aligned by the high-speed airflow velocity value. The feed tube velocity is unknown and therefore no x-axis error is shown. The target Q_{MvSS} best fit curve is shown for reference.

The three curves shown in the Figures 55 to 57 are shown overlain in Figure 58. It can be seen that the three curves are of similar value and shape. This finding, along with the observation that the curves do not mirror those of the target signal, suggests that the voltages measured at the feeder tube are not induced by voltages at the target but induced by charging caused by the lofting of the particulate. It might be postulated that the lower value relative to the target values is due to a lower energy event, and that the increasing trend is due to increasing flow speeds in the feeder tube.

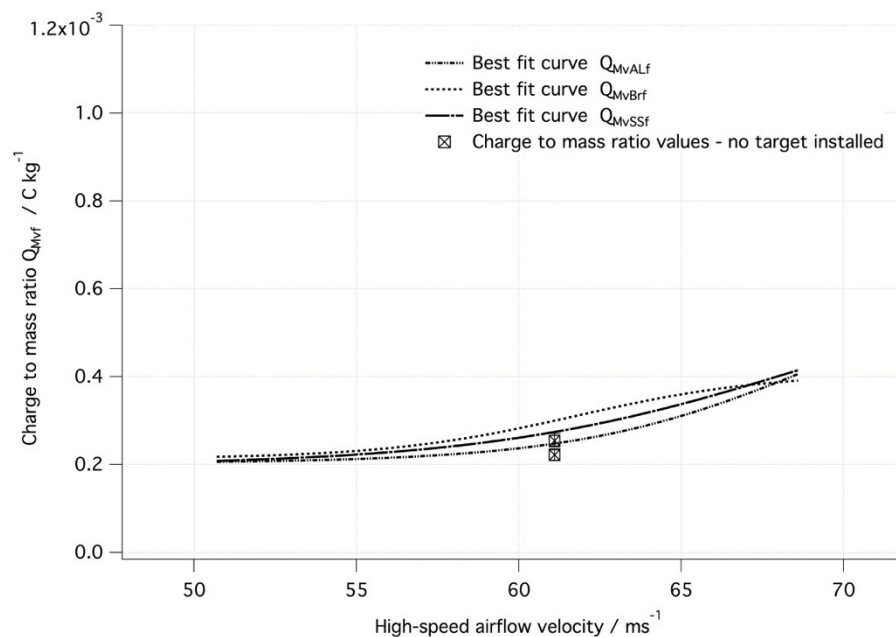


Figure 58 - Comparison of the best-fit curves of charge to mass ratio (Q_{MvALF} , Q_{MvBrf} and Q_{MvSSf}) vs high speed airflow velocity.

In order to confirm that the sense voltages, and hence the calculated charge values, were not being influenced by the field from the target, two tests were run in control configuration but with the target removed. The values measured, adjusted in accordance with control protocol, are shown plotted on Figure 58 and it can be seen that they lie in the bounds of error on the plotted curves.

In order to confirm that the measured signal was due to lofting, and not the mechanical transport of the sample in the cartridge, another test was conducted running a cartridge loaded with E15 ash through the feeder with no airflow or vacuum system running. This test measured no detectable signal from the feeder system or target.

3.7 Charge to mass ratio of Ballotini™, sand, and Sakurajima ash impacting the metallic targets at varying velocity (Q_{Mv}).

The results of impacting Ballotini™ (BAL), sand (SAN) and Sakurajima ash (SAK ash) against the aluminium target are shown in Figure 59 with the best-fit adjusted data for E15 ash shown plotted at the same airflow velocity points for comparison.

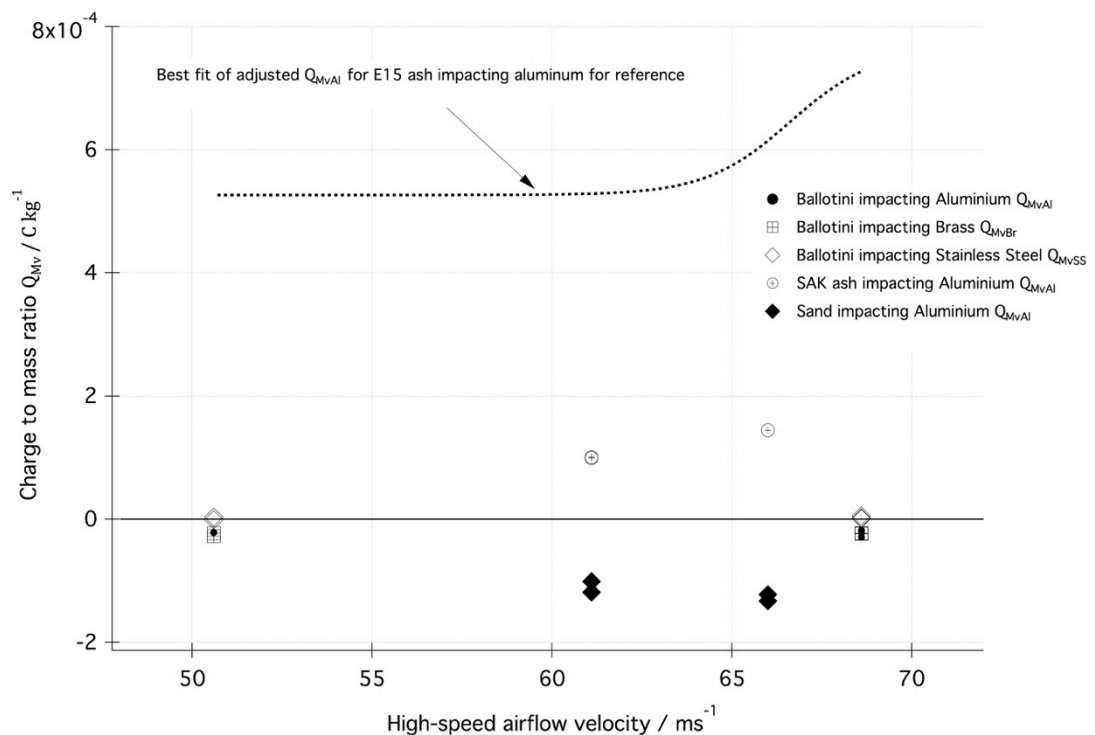


Figure 59 – The charge to mass ratio Q_{Mv} for Ballotini™, Sand and SAK ash impacting targets – error bars omitted for clarity.

Although the data are limited some quantification is possible. The Ballotini™ produced negligible signal above background levels, even at the highest airflow velocity, but signals appear to demonstrate a slight negative charge direction. This was common to all the impact target materials for Ballotini™ particulate. The sand produced a defined signal but again negative, as opposed to the ash signal. The SAK ash produced a positive signal but of a much lower level than that produced by E15 ash. It might be suggested that there is a rising charging trend with increasing airflow velocity both with the SAK ash and the sand but such a small sample and large error bounds mean this needs further investigation. A factor that may strengthen the suggestion is the current signal generated is less variable for both

sand and SAK ash than E15 ash (Figure 60), and this reduces error bounds and the spread of the data. This is evidenced by the two SAK ash data points at 61 m s^{-1} overlaying each other, and the close proximity of the other data points for sand.

Table 7 - Comparison of mean charge to mass values for Ballotini™ versus E15 ash for the tested airflow velocities.

	Mean of charge to mass for target type / $\text{C kg}^{-1} \times 10^{-4}$		
	Aluminium	Brass	Stainless steel
Airflow velocity 51 ms^{-1}			
E15 Ash	5.41	4.87	6.48
Ballotini™	-0.22	-0.25	0.01
Airflow velocity 69 ms^{-1}			
E15 Ash	7.34	7.43	7.99
Ballotini™	-0.23	-0.23	0.03

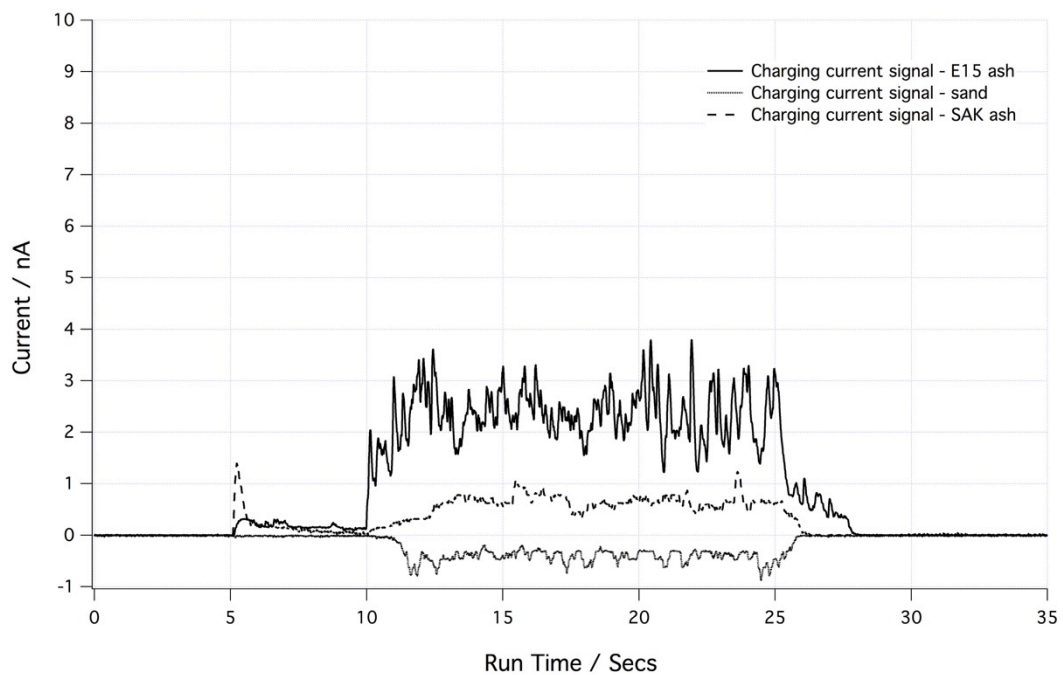


Figure 60 - Signal current traces for E15 ash, sand, and SAK ash impacting the aluminium target at 61.1 m s^{-1} (50 psig high-speed airflow pressure).

3.8 The impact of ice on an aluminium target

The results shown here are not analysed in a quantitative way, but are shown to suggest a likely behaviour. The high-speed airflow pressure was set to 50psig but the compressor was not powered for safety reasons and to keep the supplied air as cold as possible. This resulted in pressure drop after approximately 60 s of running and therefore airflow speed cannot be stated. The results are eight individual experimental runs selected from a total of 18 attempts. The remaining ten runs have known failures or no signal captured. Each of the experiments is shown below with a descriptive summary.

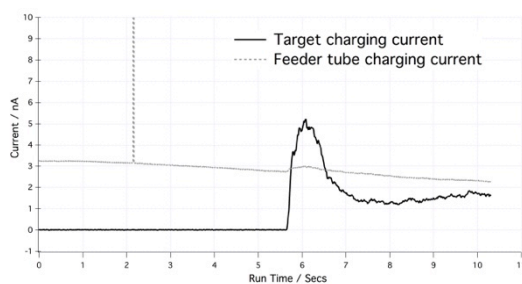


Figure 61 - The charge current signal for ice impacting an aluminium target – run #1.

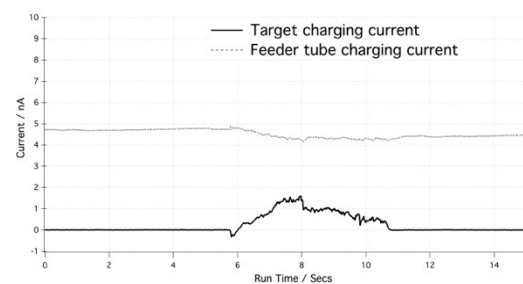


Figure 62 - The charge current signal for ice impacting an aluminium target – run #2.

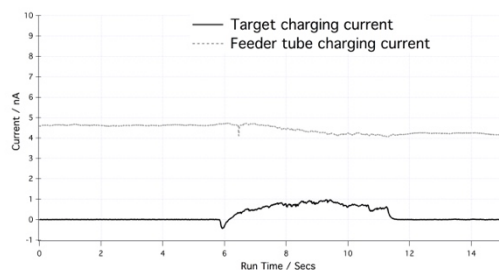


Figure 63 - The charge current signal for ice impacting an aluminium target – run #3.

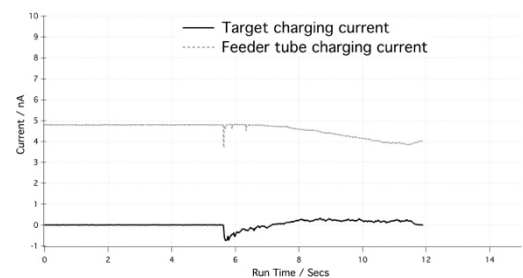


Figure 64 - The charge current signal for ice impacting an aluminium target – run #4.

Run #1 (Figure 61) was a short 50psig high-pressure airflow run ensuring constant supply pressure. The airflow and ice jet were simultaneously initiated at approximately 5 s and stopped at approximately 10 s. The signal recording was also stopped at air and ice off time. The recording shows features; (a) a high positive charge burst at the target at ice initiation followed by a relatively steady positive charging and (b) a large positive permanent offset on the feeder tube charging which tends to fall as the run progresses.

Run #2 (Figure 62) was a similar format but the water supply for the ice generation was not turned on, hence the sample injected was lofted ice grains from the ice box chamber. The initial positive charge surge is not seen, rather a very slight negative spike, but a general positive charge is seen on the target. The feeder charging remains similar to run #1.

Run #3 (Figure 63) was a repeat of run #2. The recording is generally similar to run #2 but the overall charging rate appears to be lower. The feeder tube shows a similar profile to the previous runs.

Run #4 (Figure 64) was a repeat of run #1. The profile of the target signal for this run is however different to run #1. The negative spike seen on runs 2 and 3 has amplified and the positive charging flowing is greatly reduced. It should be noted that the airflow pressure will have been depleted at this point but the levels were not recorded.

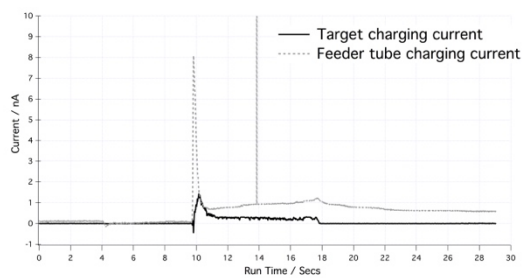


Figure 65 - The charge current signal for ice impacting an aluminium target – run #5.

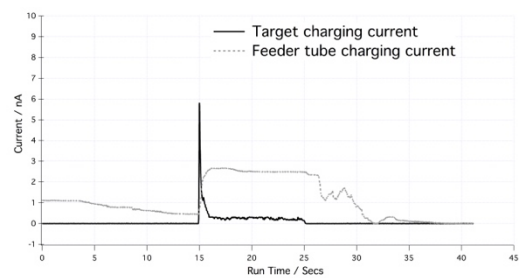


Figure 66 - The charge current signal for ice impacting an aluminium target – run #6.

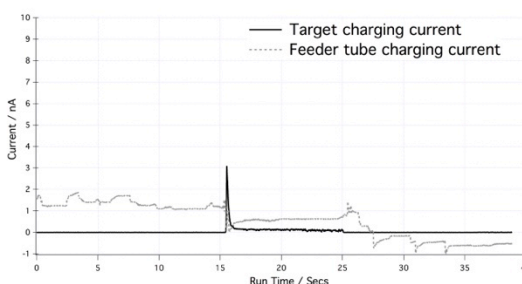


Figure 67 - The charge current signal for ice impacting an aluminium target – run #7.

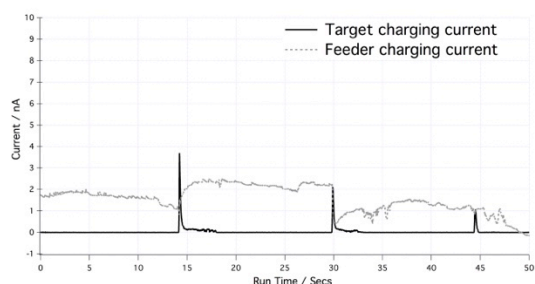


Figure 68 - The charge current signal for ice impacting an aluminium target – run #8.

Run #5 (Figure 65) was a known 50 psg run for approximately 8 s. The profile of the target charging is similar to run #1 but at a lower charge level. The feeder tube charging however shows an opposite trend, with no initial positive offset but a

positive offset and rising trend during the injection of ice. Runs 6 to 8 (Figures 66 to 68) all show a similar target charging profile to run #5, with a high initial positive spike followed by a much lower continuous positive charge level during the ice injection. Run #8 records three separate short ice injections and seems to indicate a decrease in signal that accompanied the fall-off in high-pressure airflow supply pressure. The feeder tube charging however shows a variable result, with variable positive offsets and increasing charge during injection.

In summary, no quantitative assessment of the charge to mass ratio for ice on metallic targets can be made as it was impossible to determine the mass of ice arriving at the target. However it seems reasonable to suggest that charging by ice impact is likely to be positive and probably mass rate dependent and velocity dependent. Whilst it was not possible to confirm by measurement or instrumentation that what arrived at the target was ice particulate, the evidence gathered during, and at the end of tests strongly suggests that the flow maintained as frozen past the target: (a) The temperature of the ice creation reservoir was able to be maintained at -45°C to -55°C for the tests (b) The high pressure air supply, which also supplied the airbrush, was driven from a reservoir at -30°C (c) Visible checks of the interior of the ice generation box showed no evidence of rime ice indicating the presence of liquid water (see Figures 69 and 71) and (d) checks of the face of the target showed no wetness.



Figure 69 - View to the interior of the ice generation box taken from the water injection port after completion of tests.



Figure 70 - View from above of the feeder tube impression in ice build up at the delivery end of the ice generation box.



Figure 71 - View of the interior of the ice generation box with the dry ice trays removed at the end of testing.

The offsets and variability of the feeder tube signal may be ascribed to two design issues of the feeder tube and sensing connection: (a) the feeder tube was found to collect a collar of ice, shorting the tube to the ice box chassis and (b) the electrical connection to the feeder tube consisted of a stainless steel gauze, clamped to the tube by a cadmium plated p-clip, with tinned copper crimp connection. Extreme temperature variations and the presence of water could generate dissimilar metal voltages.

3.9 The particulate grain size distribution

The particle size distribution for the three particulate samples E15 ash, sand and SAK ash are shown in Figure 72. The distribution is shown as the output of the Mastersizer 2000® laser diffraction system, with the output bins set to 2.5 micron interval. The output measure is the percentage of the total particle volume that is taken up by particles of the diameter in the group. The diameter is the diameter of an equivalent spherical volume of the measured irregular particle.

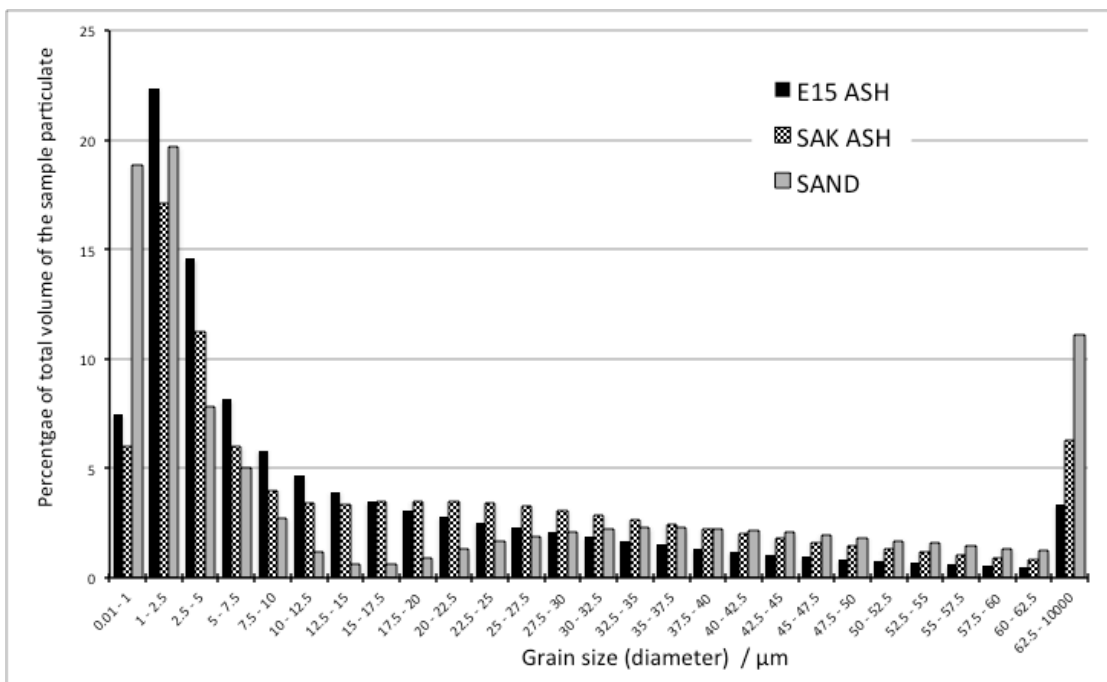


Figure 72 - Grain size distribution for experimental particulates.

4 Discussion

When we discuss the experimental findings we must consider the plausible processes that may be taking place, whilst also taking note of the uncontrolled variables and limitations inherent in the experimental equipment. An aim of the study is to investigate the physics underlying the generation of signals robust enough to be utilised in a service environment, where it should be easily discernable above background influences. It was a decision taken during the experimental design to focus on first order processes, and that certain variables would not be controlled or measured due to time scales constraining the experimental complexity.

The notable characteristic of the Ballotini™ impact experiments was the lack of charging signal for all target materials between the minimum and maximum airflow velocity limits. The signal that was detectable was generally negative as shown in Table 7, only stainless steel being close to neutral, which is interestingly in the same polarity as the sand, both materials being silicate based. Considering the particle size was consistent with the larger fraction of the VA tested, and considering the work function is likely similar to VA (both materials being silicate based), one would expect the material to charge the target equivalently. We suggest in this study that this is an indication of the relative charging influence of the contact charging mechanism compared to fracto-emission. The hypothesis is that the Ballotini™ beads, with a high roundness and high impact strength, do not fracture and hence generate negligible emissive particles and that the contact charging signal is at least an order of magnitude lower than the fracto-emission induced signal.

Whilst the experimental equipment does not allow us to capture the after-impact particulate to directly test for breakage, there is evidence to support this proposal in the work of John et al. (1980). It is stated: “Examination of the deposit on the after filter of the impaction probe revealed the presence of crystalline fragments of particles indicating that a significant fraction of the sodium chloride particles break up during the impaction”, however no remark is given in text as to the effect of the breakage. The results do however show unexplained anomalous high charge transfer values for NaCl (Figure 73).

Table 3. Contact charge* in $\mu\text{C/g}$ for particle velocity 75 m/sec

Probe	Particle material		
	Methylene blue	Potassium biphthalate	Sodium chloride
Stainless steel	-2.7 ± 0.1	-1.9 ± 0.1	$+8.0 \pm 0.6$
Inconel	-1.1 ± 0.2	-2.7 ± 0.6	$+25 \pm 4$
Titanium	-3.6 ± 0.5	-6.9 ± 0.3	$+24 \pm 2$
Platinum	-3.4 ± 1.6	-20 ± 3	-75 ± 5

* Charge transferred to the probe.

Figure 73 - Extract from John et al. (1980) showing anomalous charge values and polarity reversal for Sodium Chloride and Potassium biphthalate.

Ballotini™ is closest in physical character to the sand tested but the results show differing characteristics. Figures 59 and 60 show the negative charging effect on the target of the impact of fine sand. The reason for the negative target charging is not known at this time, and opposes the work function based expectation (assuming quartz based sand has a work function similar to VA being silicate based). However the nature of the signal gives us reason to suggest that fracto-emission might be the primary generation mechanism. The recorded trace shown in Figure 60 exhibits a high level of variation (although not as high as VA) indicating bursts of charge. Hence it is more likely that fracturing of the weaker particles is taking place. It can only be assumed that the net emission product is heavily biased towards electrons.

Figures 59 and 60 show the data points for Sak ash impacting the Al target. The Sak ash charges the target positively in line with the E15 ash however there are some key differences between the Sak ash and E15 data:

- i. The quantity of charging is much lower than E15 ash.
- ii. The variability of the charging signal is much lower than E15 ash (similar to sand).

As Sak ash is likely to be very similar to E15 ash, then the charging rate difference must be due to other reasons. The structure of the Sak ash may mean the degree of fracture that occurs on impact may be different to E15 ash. Unfortunately we have no image data to compare the ash types. We can perhaps look at the variability of the trace in Figure 60 and propose that the reduced variability is an indication of less dynamic activity or fracturing. When we examine the grain distribution shown in Figure 72 it is evident that the Sak ash has a significantly lower fine fraction than E15 ash. If we expand that hypothesis and look at the results for only those particulates

that we believe to be fracturing we can detect some possible linkage between charging behaviour and particle size. If we look at only the charge to unit mass magnitudes (particles impacting aluminium) whilst ignoring the polarity of the charge we can order the material types from high to low for the two air velocities we have data for (tables 8 and 9).

Table 8 – Mean charge to mass values for particles impacting an aluminium target at 61 m s⁻¹, ordered by quantity.

	Material	Mean Charge to mass / C kg ⁻¹ x 10 ⁻⁴
higher	E15 ash	4.97
⇕	Sand	1.1
lower	Sak ash	1.0

Table 9 - Mean charge to mass values for particles impacting an aluminium target at 66 m s⁻¹, ordered by quantity.

	Material	Mean Charge to mass / C kg ⁻¹ x 10 ⁻⁴
higher	E15 ash	6.26
⇕	Sak ash	1.45
lower	Sand	1.27

Examining these data and comparing them to the grain size distribution, a link can be seen between the different material particle fractions in the diameter bands from 1 µm to 15 µm, and the ordering of the charge magnitude. In the 1-2.5 µm band the grain size ordering follows the ordering shown in Table 8, the lower velocity, whilst between 2.5 µm and 15 µm it follows that of Table 9, the higher velocity. This might suggest that the combination of the energy of impact and the particle size distribution is a driving factor in the magnitude of the charge generated.

Having considered the comparison between a fracturing particle and a non-fracturing particle, and between fracturing particles of differing types, we can further examine the detailed results of the E15 ash impacts to determine whether the charging behaviour seen is better explained by contact charging theory, or by fracto-emission.

To do this we must look at the experimental equipment dynamics of the particle transport outlined below, and begin at the point at which particles leave the dispenser cartridge in the side feeder tube. The lofting process can reasonably be expected to involve particle-particle interactions and particle-feeder interactions, each of which may introduce charge to the particles and gases. The particulate entrainment air is room atmospheric and so is of variable relative humidity (RH) and temperature, recordings taken indicated a range of 40-55 % RH and temperatures of 18-24 °C. The 'dusty gas' is then further entrained into the high-speed flow and impacts the target. The distance between the side feeder tube interface with the high-speed flow and the target is small at 25 mm and we therefore neglect any increase in particle-particle interaction that may take place before the 'dusty gas' interacts with the target. The particulate loaded flow then impacts the target and the following scenarios are postulated:

- i. A particle approaches the target and flows round it without impacting the surface.
- ii. A particle impacts the target, rebounds physically unchanged, and is carried away in the airflow.
- iii. A particle impacts the target, fractures, and the component parts are carried away in the airflow.
- iv. A particle impacts the target, pierces the surface of the target removing some surface material, rebounds physically unchanged, and is carried away in the airflow.
- v. A combination of (iii) and (iv).

This study investigated the hypothesis that particle fracture and hence fracto-emission is occurred within this dynamic process, and generated a measurable signal. Therefore in each of the above cases, where particle-surface or particle-particle interactions take place, we must hypothesise what the possible electrical charging outcomes of the interaction may be. In the case of (i) above, any charging would be particle-particle only, but this scenario would depend on the airflow character and the particle size in accordance with Stokes Law. In the case of (ii), charging would have to be analysed using the model of contact or frictional charging, either with simple impact / rebound theory or the more complex impact / slide / roll / rebound theory (Matsusaka et al., 2010). In the case of (iii) we have to consider the electrical characteristics of the fracture products as described in the introduction. In the case of (iv) we have to consider the electrical characteristics of the fracture products of the surface, but also the result of contact charging processes

from (ii). Finally in the case of (v) we have to consider the possibility of all of the aforementioned processes operating simultaneously.

Before we can interpret the experimental results in order to identify process, it must be recognised that the two charging mechanisms of the target, the particles, and the surrounding gasses have a significant difference. Contact or frictional charging involves only the interaction between the contact face of the particle and impact surface while the two components are physically together, or shortly after the point of separation. The involvement of the surrounding space is only invoked when the charge levels on the particle interaction exceed the level required to generate an electrical field strength sufficiently high to trigger gas breakdown (Matsuyama and Yamamoto, 1997). Conversely fracto-emission implicitly involves the surrounding space as the electrically charged products of the fracture are ejected into the surrounding free space whether gas filled or not. We propose that the charge transfers that occur after a fracto-emission event proximal to a metallic conductor and in atmospheric conditions will not necessarily conform to the same relationships of impact velocity and energy predicted for contact charging. The empirical models proposed by John et al. (1980), Matsuyama and Yamamoto (1994), and the earlier works quoted therein, should be observed if contact charging is the functional process and fracto-emission is not present. If deviations from those contact charging relationships are found then it may be possible to find an explanation within fracto-emission hypothesis.

There is an assumption made in the previous empirical contact charging work that the particles involved are spherical, homogenous and do not fracture. We have already shown in the images in Figures 8 and 9 that this is not the case here. We must also consider the chemical and physical constitution of the particulates involved in the impacts (those properties are shown in Methods).

It may be useful at this point to propose some generic comparisons of outcomes and effects based upon work from the two charging hypotheses of a particle impacting a surface. Also, as our samples were all polydisperse, it is necessary to consider the effect of particles' charge reaching the value where the electric field created is sufficient to cause gas breakdown.

4.1.1 The products of the impact.

Contact or frictional charging during impact would result in charge transfer to or from the metallic plate in accordance with the work function of the materials. This is demonstrated in the work of Trigwell et al. (2009) who found the work function of lunar simulant. Ions in the free space proximal to the surfaces would only be generated by the electrical breakdown of the gas or by heating actions of the impact (Harper, 1970). Of note is the determination in John (1995) that there are no data on the charge transfer of impacts of sub-micron particulate.

The oxide layers fractured in the fracto-emission work of Dickinson et al. (1978) may point to likely electron emissions into the free space on breakage of the oxide layers in the coatings and bulk, of the E15 ash particles. The work of Dickinson et al. (1981), Dickinson et al. (1982) and Dickinson et al. (1984) would suggest emission of ions such as OH^+ and H_2O^+ and the work of Gislason et al. (2011) demonstrated that those ions are all present in E15 ash. Furthermore the chemical analysis results of Gislason et al. (2011) indicate that the findings of Freund (2000) are possible, with positive “electron charge holes” being presented to the fractured particle surfaces.

4.1.2 The effect of the material pairing

The relationship of the impacting particle material and the target material in contact or frictional theory has effects based upon work function as stated in § 4.1.1, where the charge transfer polarity and magnitude is dictated by work function differences. Charge transfer will also be affected by the particle physical characteristics such as the Young's modulus and surface topography (John et al., 1980).

When considering fracto-emission the material pairing effects can be constrained to the mechanical differences that control the degree of fracture, which material fails and in what proportion. This has been demonstrated in work carried out by Nicholls et al. (2013) in the erosion of compressor blades by different particulate materials. This work found differences between the erosion rates of silica sand and volcanic ash when impacted against Ni and Ti alloys. If fracto-emission is taking place then the increased removal of the compressor alloy or reduced failure probability of the particle may change the ratio of ions and electrons released into free space.

4.1.3 The effect of velocity of impact.

The research on contact or frictional charging suggests linear relationships between the normal component of the impact velocity and charge generation, up to the level of charge saturation causing gas breakdown. John et al. (1980) demonstrated a linear dependence which was confirmed in the work of Matsuyama and Yamamoto (1994) and re-stated in John (1995). However when we consider the effect of velocity of impact in fracto-emission we must consider the effect on breakage probability. John (1995) discussed the failure of particles (without reference to charging) and found that for many particles, impact at velocities that generated rebound also occurred above the plastic yield limit. John (1995) further discussed earlier work on the deagglomeration of 2.8 μm latex doublet particles (John and Sethi, 1993) noting that the probability of breakage increased in the measured velocities of 10 to 100 ms^{-1} . These velocities and particle size are in the range of this study. Later work in smaller and larger particle size ranges yielded a common result of the breakage probability of irregularly shaped particles (see Figures 74 and 75) following a lognormal curve when plotted against impact energy (Froeschke et al., 2003, Aman et al., 2011), thus a similar probability against v^2 .

The theory of breakage probability following a lognormal curve lends support to the chosen selection of a Boltzman curve for the line of best fit for the charge vs velocity curves shown in the results sections 3.3 and 3.6. The proposed behaviour is that, as the velocity increases, a specific particulate size fraction or size band reaches its failure limit and charges are generated. As velocity continues to increase fracture increases in accordance with the lognormal curve, and likewise charge generation. However a velocity is reached where either all particles fracture, and therefore charging is at it's maximum, or charge neutralisation occurs through gas discharge and again a maximum is reached.

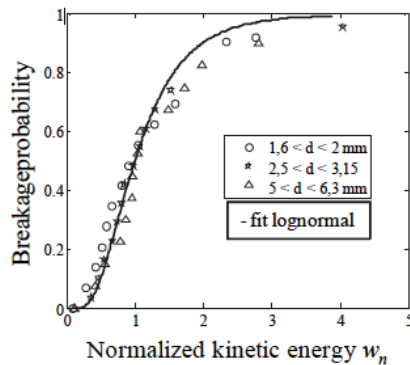


Figure 74 – Cumulative experimental distributions of breakage probability of basalt particles versus normalized kinetic energy – image and text Aman et al. (2011).

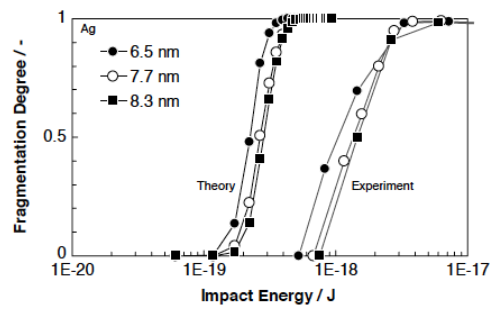


Figure 75 - Calculated degree of broken bonds based on the model (array of curves left-hand side) and experimental determined kinetic energy, which is necessary to obtain a certain degree of broken bonds (array of curves right-hand side) after Froeschke et al. (2003).

4.1.4 The effect of particle surface charge limits.

The one common factor between charging mechanisms is the maximum charge that a single particle may maintain after the charging event in atmospheric conditions, but the magnitude of this charge has been debated. The charge limit is determined by the field strength at which the charge can bridge any contact gap by electron tunnelling, or gas breakdown occurs. The commonly quoted value is $3 \times 10^6 \text{ V m}^{-2}$ for air, which equates to a surface charge of approximately 26 to 27 $\mu\text{C m}^{-2}$ (Blythe and Reddish, 1979, Bailey, 1993); this value equates to flat surfaces. The radius of small particles cause field divergence and field reduction according to an inverse square law, resulting in the stability of higher surface charge densities, theoretically in line with the values calculated from Paschen's Law. Quantification by Blythe and Reddish (1979) suggest charge per surface area magnitudes of 250 to over 500 $\mu\text{C m}^{-2}$ for 20 μm diameter particles, but in text revise this to merely 10 $\mu\text{C m}^{-2}$ as a realistic net charge figure for particulate in a pipe stream. This lower non-particle size value is not in agreement with Bailey (1993) who quotes an expression to find the maximum charge per unit area as:

$$\sigma = 8.2 \times 10^{-6} r^{-0.3} \text{ C m}^{-2} \quad (1.7)$$

and also an expression to determine charge per unit mass as:

$$Q_{Mr} = \frac{2.45 \times 10^{-5}}{\rho r^{1.3}} C \text{ kg}^{-1} \quad (1.8)$$

Using the values of $10 \mu\text{C m}^{-2}$, $27 \mu\text{C m}^{-2}$ and equation (1.7) the maximum charge per particle values for the experimental particle size bands within the measured grain size distribution curves in figure 72 were calculated. The diameter used for each band was the geometric mean of the range. The geometric mean was chosen to be in line with the manufacturer's methods of size band selection (Malvern Instruments Ltd, 1999). The results are shown in Table 11.

Using these data and commonly used bulk densities for basaltic ash (2800 kg m^{-3}) and quartz based sand (2600 kg m^{-3}), we can estimate the maximum charge per unit mass that the experimental particulate can sustain under atmospheric conditions. Those data are shown in Appendix N Tables 13, 14 and 15 are converted to charge to mass value (C kg^{-1}) and summarized in Table 10. Net charge values can be orders of magnitude less in a multi-polarity particle volume (James et al., 2000).

Table 10 – The maximum theoretical charge per unit mass (C kg^{-1}) that can be sustained under a range of surface charge limit assumptions.

Material	Max charge to Mass / C kg^{-1} (Surface charge value $10 \mu\text{C m}^{-2}$)	Max charge to Mass / C kg^{-1} (Surface charge value $27 \mu\text{C m}^{-2}$)	Max charge to Mass / C kg^{-1} (Surface charge i.a.w. Eq (1.7))
E15 Ash	2.07E-02	5.59E-02	2.26
Sak Ash	1.66E-02	4.49E-02	1.82
Sand	4.40E-02	1.19E-01	5.31

Table 11 - Calculated maximum particle surface charges according to various theoretical surface charge limit assumptions.

Size band / μm	Geometric mean dia. of the particle / μm	Surface area of one particle $4 \pi r^2$ / m^2	Charge on a particle with surface charge of $10 \mu\text{C m}^{-2}$ /C	Charge on a particle with surface charge of $10 \mu\text{C m}^{-2}$ /C	Charge on a particle with surface charge i.a.w. Eq (1.7) /C
0.01 - 1	0.10	3.14E-14	3.14E-19	8.48E-19	3.99E-17
1 - 2.5	1.58	7.85E-12	7.85E-17	2.12E-16	4.36E-15
2.5 - 5	3.54	3.93E-11	3.93E-16	1.06E-15	1.71E-14
5 - 7.5	6.12	1.18E-10	1.18E-15	3.18E-15	4.36E-14
7.5 - 10	8.66	2.36E-10	2.36E-15	6.36E-15	7.85E-14
10 - 12.5	11.18	3.93E-10	3.93E-15	1.06E-14	1.21E-13
12.5 - 15	13.69	5.89E-10	5.89E-15	1.59E-14	1.71E-13
15 - 17.5	16.20	8.25E-10	8.25E-15	2.23E-14	2.28E-13
17.5 - 20	18.71	1.10E-09	1.10E-14	2.97E-14	2.91E-13
20 - 22.5	21.21	1.41E-09	1.41E-14	3.82E-14	3.60E-13
22.5 - 25	23.72	1.77E-09	1.77E-14	4.77E-14	4.35E-13
25 - 27.5	26.22	2.16E-09	2.16E-14	5.83E-14	5.16E-13
27.5 - 30	28.72	2.59E-09	2.59E-14	7.00E-14	6.03E-13
30 - 32.5	31.22	3.06E-09	3.06E-14	8.27E-14	6.95E-13
32.5 - 35	33.73	3.57E-09	3.57E-14	9.65E-14	7.92E-13
35 - 37.5	36.23	4.12E-09	4.12E-14	1.11E-13	8.95E-13
37.5 - 40	38.73	4.71E-09	4.71E-14	1.27E-13	1.00E-12
40 - 42.5	41.23	5.34E-09	5.34E-14	1.44E-13	1.11E-12
42.5 - 45	43.73	6.01E-09	6.01E-14	1.62E-13	1.23E-12
45 - 47.5	46.23	6.72E-09	6.72E-14	1.81E-13	1.35E-12
47.5 - 50	48.73	7.46E-09	7.46E-14	2.01E-13	1.48E-12
50 - 52.5	51.23	8.25E-09	8.25E-14	2.23E-13	1.61E-12
52.5 - 55	53.74	9.07E-09	9.07E-14	2.45E-13	1.75E-12
55 - 57.5	56.24	9.94E-09	9.94E-14	2.68E-13	1.89E-12
57.5 - 60	58.74	1.08E-08	1.08E-13	2.93E-13	2.03E-12
60 - 62.5	61.24	1.18E-08	1.18E-13	3.18E-13	2.18E-12
62.5 - 250	125.00	4.91E-08	4.91E-13	1.33E-12	7.35E-12

The discussion below will look at the each stage of the particle flow in the experimental equipment during a test run, using the generic outcomes and effects from above as a framework.

4.2 The particle lofting and high-speed flow transport.

We need to consider the method of the lofting of the particulate in relation to flow energy and likely flow patterns. The flow through the side feeder tube (Figure 19) is driven by low pressure at the side feeder tube exit caused by the crossing of the high-speed flow. The flow in the high-speed air nozzle ranges approximately from 50 to 70 ms⁻¹. Knowing the high-speed airflow velocity we can estimate the flow in the side feeder tube as 10 ms⁻¹. Using the equation for Reynolds number in a pipe flow:

$$\text{Re} = \frac{\rho v D_H}{\mu} \quad (1.9)$$

ρ = density of air 1.2754 kg m⁻³ @ 20°C.

v = the velocity of the fluid 10 ms⁻¹.

D_H = the hydraulic diameter of the nozzle = 0.010.

μ = the dynamic viscosity of air @ 20°C = 1.837 x 10⁻⁵ kg m⁻¹s⁻¹.

This yields a value of Re of approximately 7000. It can be seen from Figure 76 that the flow behind the side feeder tube would be a fully turbulent vortex sheet. This would indicate that the likely extraction mechanism of the particulate is rotational scavenging with particulate dragged into the low pressure centres of the vortices and pulled into the airflow. It is evident that this process would involve collisions of the particulate with the edges of the sample cartridge and frictional contact of the particulate in the cartridge. There will also be collisions with the inner wall of the feeder tube on its way to the high-speed flow.

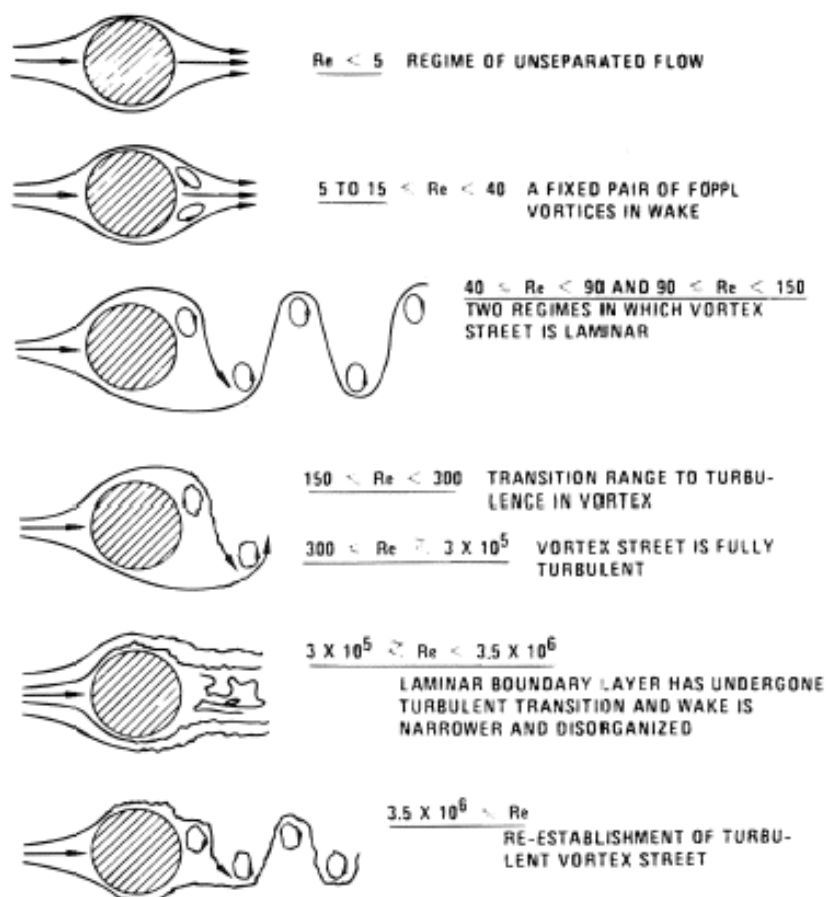


Figure 76 - The effect of Reynolds number on turbulence behind a cylinder, image from Blevins (1977).

One might expect the charging in these conditions to be in accordance with contact / frictional charging principles. If we assume the work function values in Table 12 then the brass feeder tube should charge positively in respect to the E15 ash (Bailey, 1993). The evidence from Figure 58 appears to show this is the case, as the curves of charge to mass ratio versus airflow velocity (based upon the suction velocity as the actual velocity is unknown) show an almost linear trend and positive charging of the feeder tube. However we suggest that there are some indications that fracto-emission may be present. Firstly the curves for all three data sets show an upward non-linear trend which, although small enough to be considered within error limits for a straight line, is consistent across the data set. Secondly the data display an increase in variability in the region of impact velocity of 65 ms^{-1} (see Figures 55 to 57), which suggests a change in dynamics. We suggest that the lofting process is at the bottom of the curves shown in § 4.1.3 and that further airflow velocity increase would yield a non-linear response. Support for this argument is found in the development of the lofting equipment where it was found that the flow rate over the

feeder cartridge was a critical value; with a more energetic flow the particle charging rate in the feed system could actually exceed the target charging rate.

Table 12 - Available Work function values for experimental materials – Note: the figure quoted for E15 ash is that of the closest equivalent known and that of the NASA JSC-1 Mars simulant.

Material	Work Function value	Reference
Aluminium	4.08 – 4.29	(Eastment and Mee, 1973)
Brass	4.8	(Bond, 2008)
Stainless Steel	4.2 – 4.4	(Feuerbacher and Fitton, 1972) (Sternovsky et al., 2002)
E15 Ash (JSC-1 Simulant)	~5.4	(Trigwell et al., 2009)

The measured range of charge to mass values, being $0.2 - 0.4 \times 10^{-3} \text{ C kg}^{-1}$ is well below the various maximum values shown in Table 10 and suggest the particulate is considerably below its atmospheric charge limit. A charge to mass ratio of $0.4 \times 10^{-3} \text{ C kg}^{-1}$ equates to a surface area charge average across all particles of $0.14 \mu\text{C m}^{-2}$ which is two orders of magnitude smaller than the limit suggested by Blythe and Reddish (1979). The values from the three experimental runs show good consistency when adjusted using the control methodology described previously and the low charge values indicate a low energy process. The flow rate achieved appears to be the best compromise between the energy of dispersion versus the efficiency of the scavenging. Figure 77 shows an example of the scavenging effect with the emptied section clean and bright. There is evidence of down-tube scavenging but this remained a constant within the test run.

The assumption is made that the lofted particulate leaves the side feeder tube with a net negative charge if charge balance is maintained. Considering the findings above, and the lack of charging seen from the Ballotini™, we propose that the charging seen at the feeder system is consistent with fracto-emission. We further propose the fractures occur when interlocking particles are separated and when particles impact the feeder components.

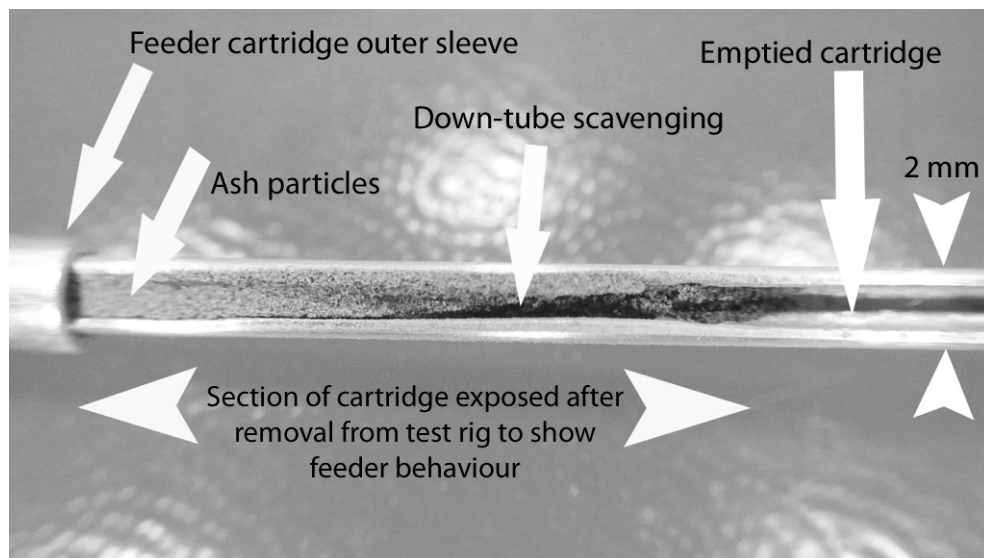


Figure 77 - An example of particle scavenging from the feeder cartridge. Evidence of scavenging from inside the cartridge is evident but the empty tube section is clean and bright.

4.3 The impact at the target face.

In considering the impact process at the target we must discuss the airflow at the target face. Using equation (1.9) we can calculate the Re number for the high-speed flow where v = the velocity of the fluid = 50 m s^{-1} or 70 m s^{-1} . This yields an Re value in the main flow of the high-speed airflow of approximately 34700 to 48600 which indicates that the flow in the high-speed nozzle is sustained turbulent (Avila et al., 2011). Given the flow is turbulent the use of Stokes law to determine if the particulate is impacting the surface is invalid, therefore we will use the empirical evidence. The best available evidence comes from the erosion patterns seen on the target faces shown in Figures 38 and 39. It can be seen that the patterns closely align to the velocity contours, and that even in the lower velocity areas, erosion indicative of particle impact is visible. While the dynamic behaviour of individual grain size bands cannot be quantified, we believe it is reasonable to assume a high percentage of the particulate impacts the target.

Consider first the results of the E15 ash impacting the three metallic targets shown in Figures 46, 47 and 48. When shown plotted together some common features and differences appear (refer to Figure 78). Each curve displays a consistent charge level up to 60 ms^{-1} , at which point a non-linear increase in charge per unit mass occurs. Also at that point the difference between the curves for Brass and Al and that

of stainless steel reduces, that is, the rate of increase of charging is higher for Brass and Al.

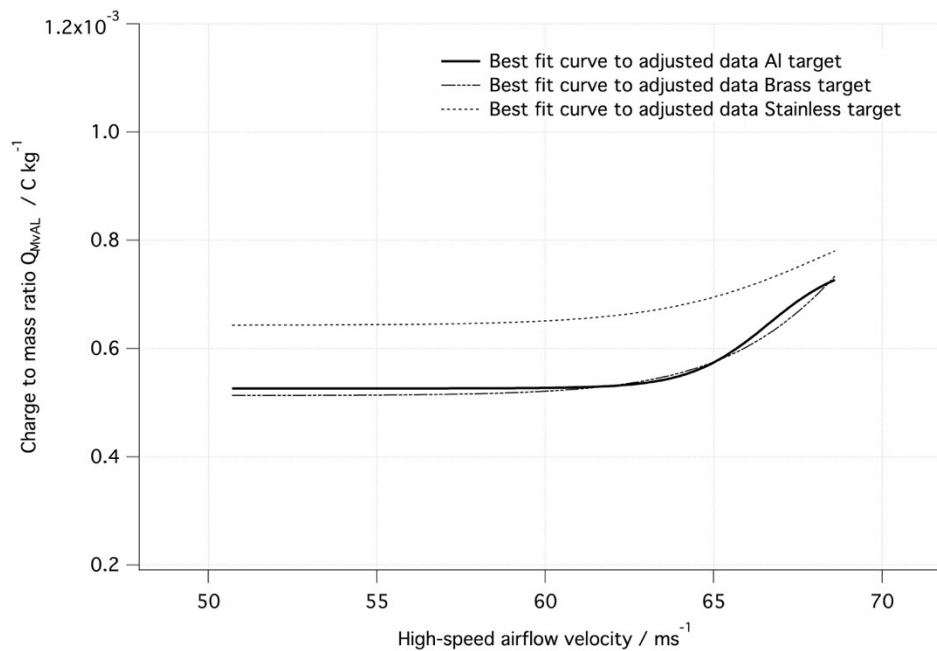


Figure 78 - The comparison of the adjusted best-fit line for the charge behaviour of E15 ash impacting the three metallic targets.

Whilst the charging rate of the Brass and Al target are very similar, the rate for stainless steel is significantly higher. This might be explained by differences in work function if we were to assume the contact charging model. However there are some inconsistencies that suggest that the contact charging / work function model may not be the driving process:-

- i. Considerable disagreement concerning the work function of alloys and oxidised metallic surfaces exists. The data shown in Table 12 are for pure metals with bright surfaces, however Harper (1967) postulated that all oxidised surfaces will have a work function of $\sim 5.5\text{eV}$. This would be on parity with the VA samples. This ambiguity casts doubt on the charge rate differences seen being due to work function differences. That doubt is increased when we consider that the erosional action of the ash would remove the oxide layer of the metallic target and expose new material, hence changing the work function during the flow of particulate. This should be seen in a change of the charge rate at a constant mass delivery rate over time, which was not observed.

- ii. All of the data in the literature concerning the variation of charging with impact velocity for contact charging, such as John et al. (1980), propose a linear relationship as stated in § 4.1.3. The charging behaviour observed appears to show a rapid increase in target charging after a velocity of 60 m s^{-1} is achieved. Also, as per the feeder tube, the data become much more variable at 60 m s^{-1} velocity (particularly evident in the case of Al and stainless steel (Figures 46 and 48.)) This seems indicative of a change in dynamics.

We suggest in this study that the charging curves shown could be indicative of the failure of the particles of a certain size due to yield limits being reached at specific velocities. The Figures shown in § 4.1.3 indicate that once a critical energy is achieved, the failure probability of irregularly shaped particles rapidly increases to 100%. This rapid increase in fractured particles has two effects:

- i. The fractured surface area rapidly increases, producing a burst of electrons and ions into the free space around the target.
- ii. If we then consider the theory expressed in equation (1.7), where an increased charge can be held on smaller particles, it is feasible that charge generated during fracto-emission can be held on the smaller particles, increasing the charge to mass ratio in a non-linear way. This can be modelled using the measured particle distribution for E15 ash and assuming an arbitrary breakage regime. The model is based on the assumption of larger particles shedding small fragments in the sub micron range. An excel solver function was used to find a reduction factor which increased the sub micron range count by approximately 30%. The range from $1 \mu\text{m}$ to $10 \mu\text{m}$ was left unchanged. The solver delivered a reduction in the coarse fraction of approximately 6% and an total charge increase of approximately 30%. The data are shown in Appendix O, and figure 79.

The data for the charge to mass ratio of the particulate impacting the Al target at varying mass rates but constant velocity (shown in Figures 52, 53 and 54 and combined in Figure 80) demonstrates a high degree of linearity and constant charge to mass ratio, regardless of the mass delivery rate and target material type. The charging rate difference between Al, Brass and stainless steel is maintained. This direct relationship between the rate of mass impact (which can be equated to mass concentration by volume in airborne suspended ash) and the charge created on the target is important when we consider the need for a potential sensor to deliver mass concentration data.

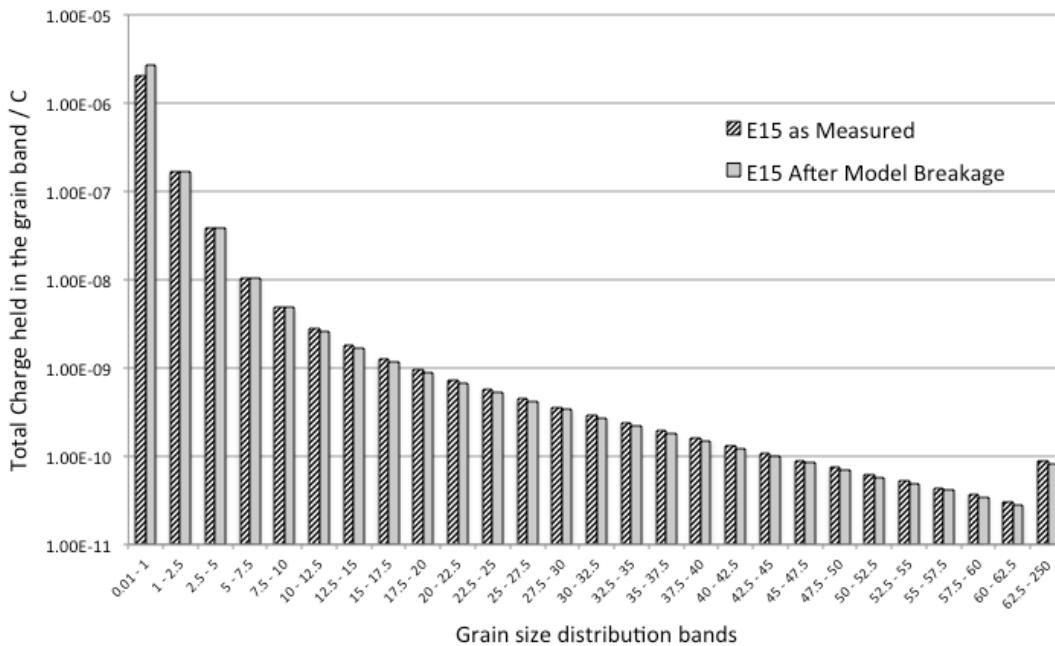


Figure 79 - Graph of charge held per grain size distribution band (C / band) pre and post breakage according to the suggested model.

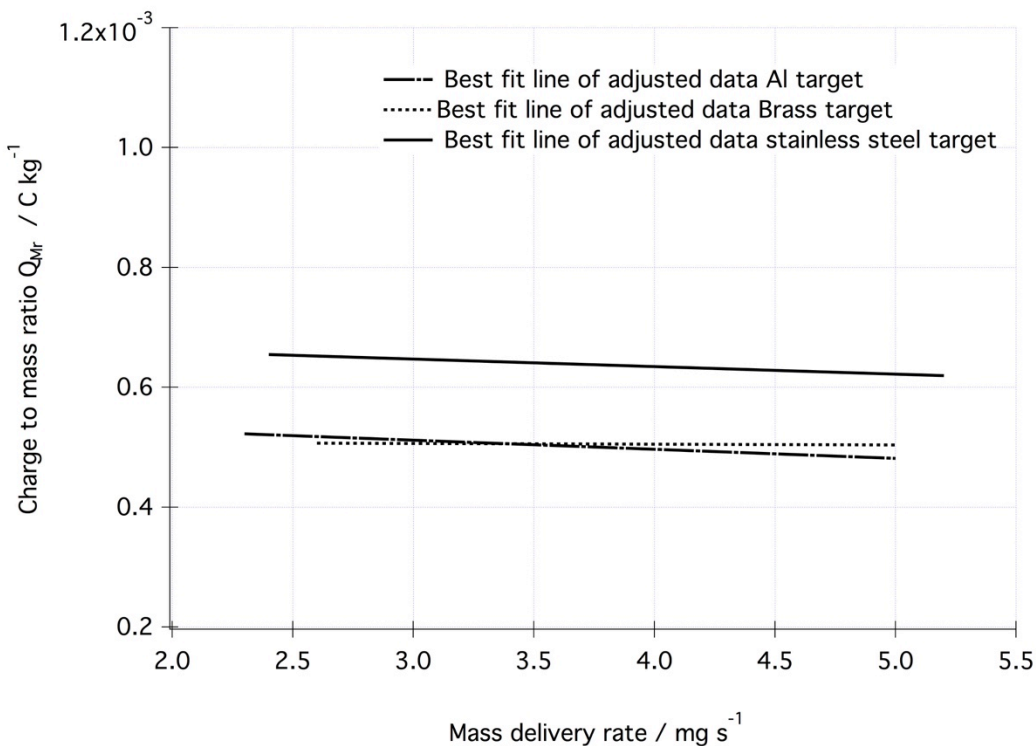


Figure 80 - The comparison of the adjusted best-fit line for the charge behaviour of E15 ash impacting the three metallic targets at constant velocity but varying mass delivery rate.

Further, when we review the data for varying impact velocity we see a further indication that the relationship between the impacted material, and the particulate may invoke differing charging behaviours. The data shown in Figure 78 and Table 6 suggest that the rate of increase of charging with increasing velocity generated by E15 ash impacting the aluminium target may be reducing towards an impact velocity of 70 m s^{-1} . However the same particulate impacting the brass target shows an increasing rate of increase of charging with increasing velocity.

If we combine the effect that particulate / target material pairs have differing charging behaviours at any particular velocity, and that the differences between pairings may change with differing velocity, then we can suggest that: (a) a particulate / target pairing may have a unique charging 'signature' when plotted against impact velocity and (b) exposing a target array of differing materials to the same particulate stream we may be able to identify the particulate material by comparison of the charging behaviour.

4.4 The analysis of the impact of ice.

The investigation of ice impacts has been qualitative rather than quantitative in an attempt to see if a conclusive detection of ice impacts was possible using the equipment. The results of the eight useable tests shown in Figures 61 to 68 show some consistent and some variable features:-

- i. All of the eight recordings display a positive charging element.
- ii. Three of the eight display a negative spike on the initiation of particle flow before a reverse to positive charging.
- iii. All of the eight show stability within the recording that is to say there is minimal signal noise compared to VA signals.

This behaviour is contrary to the findings of Illingworth (1984) who stated that most metals, including Al charged negatively in accordance with the work function rule. Further work from the same group (Caranti et al., 1985) stated a work function for ice of 4.3 eV which is close to the value of Al which seems to contradict the earlier assumptions. Firstly there are also some statements that may allude to other processes being involved. In the 1984 work Illingworth states: "For some of the interactions with the largest particles positive charging was found, and these events were often accompanied by complex waveforms. It appears that although the 45cm long free-fall section of tube is long enough for complete freezing of the $100 \mu\text{m}$

particles, because of the mass increase and greater terminal velocity, the 200 μm particles are only partially frozen and so are likely to disintegrate when hitting the target". Evidently some kind of disintegration event involving slush caused a positive charge on the metallic target. Secondly Caranti et al. (1985) states, "A layer of ice estimated to be 1 μm thick deposited from the vapor ("frost") on the target is sufficient to cause it to charge positively", so when a particle hits and ice layered surface, the impact removal of the frost causes positive charging. We therefore propose that the positive signals seen in this study are due to either or both of the effects above, and that the events where negative spikes are shown correspond to brief periods of clean ice-on-metal contact.

5 Conclusions and suggestions for further work.

We conclude that, whilst the “traditional” theory of contact or frictional charging might be applied to this study, the system studied here does not focus on pure spherical particles working in a vacuum or low pressure, but is examining irregular and structurally weak particles in an uncontrolled atmospheric environment. The evidence from (a) the comparison of Ballotini™ particles impacting metallic targets to E15 ash impacting metallic targets, and (b) the errors and inconsistencies in terms of charge values and dynamic charging behaviour identified, strongly suggest that fracture of the particles is occurring and that such fracture will generate charged particles and surfaces in accordance with earlier empirical evidence, that is, fracto emission is taking place. Further support for this hypothesis is demonstrated when we compare the charging magnitudes seen in this study to values seen in the work of James et al. (2000). Our experimental findings of target charging magnitudes of $5 - 7 \times 10^{-4} \text{ C kg}^{-1}$ (Figure 78) align reasonably well with the findings of James et al. (2000) who derived net charge values of 10^{-5} to $10^{-6} \text{ C kg}^{-1}$ and specific charge values up to $10^{-3} \text{ C kg}^{-1}$. We suggest that these comparisons indicate that the primary driver of the target charging is fracto-emission.

We further conclude that the evidence of differing charging behaviours between the three metallic targets under the impact of E15 ash (Figure 78), along with the evidence of differing charging behaviour of sand and E15 ash impacting the Al target (Figure 60) indicate that there is a charging magnitude and polarity relationship due to the target material and particle material pairing. It is felt valid to consider the fact that the fracture probability (and hence the changing of the grain size distribution of the particulate along with the increased number fracture faces) determines the changing magnitude of the charging. The fracture mechanics, and therefore the charging processes associated, will be non linear, based upon the mechanical properties of the particulate, and the physical properties of the surface impacted. Whilst we have no direct evidence, such as particulate captured after impact with the target, to make a grain size distribution comparison, there is unexplained evidence in earlier work (as previously stated in § 1) that this process occurs, such as John et al. (1980), Illingworth (1984) and Caranti et al. (1985).

In this study we propose the following dynamic process for the impact of VA against the target surfaces:

- i. The particulate is lofted at low energy from the feeder cartridge. The lofting involves particles being fractured as they are pulled from the cartridge due to being interlocked while at rest, and due to impacts with the cartridge edge and feeder tube while in the vortex stream. The fractures cause electron and ion emission and the production of positive charged surfaces in accordance with Freund (2000). This burst of positive sites at the fracture face causes the scavenging of electrons from the surrounding gas and metallic contact surfaces. This process, along with the removal of electrons to neutralise emitted +ve ions, leaves the feeder tube electron deficient, that is, positively charged.
- ii. The particulate is accelerated in the high-speed flow and impacts the target. The same fracture emission process described at the feeder occurs at the target face, but with much increased energy. The increased energies of higher velocity impacts are enough to trigger failure of a band of particle size resulting in a cascade of electrons, ions and fine particulate into the volume. This particulate is able to retain more charge than the equivalent large particulate volume, increasing the charge to mass ratio inline with the particle breakage. Differing mechanical properties of the impact material (Young's modulus, surface texture, coatings) cause differing fracture properties resulting in differing charge levels for various materials. The particulate leaves the target with an increased negative charge and leaving the target net positive.

We propose that having met the aims of:

- a) Showing fracto-emission is occurring;
- b) Identifying linkages between the impacting particle material and the target material and;
- c) Collecting the data in atmospheric conditions at rates of impact of mass inline with the assumptions for an aircraft mounted sensor suggested in § 1;

that this study provides evidence that an aircraft sensor based upon fracto-emission charging is feasible.

We further propose that a sensor may be usefully composed of an array of differing target materials, and that the development of empirically based signatures for the charging behaviour of pairings of particulate and target material may enable it to not only sense the mass concentration of particulate in the airflow, but to identify an unknown particulate material.

Using the hypothesis that a sensor based upon fracto-emission could provide mass impact rate data, and impacting material type data, it can be seen that the integration of those data with aircraft on-board data could provide the basis for a warning and guidance system for pilots. Combining the sensor dimensions with the aircraft velocity allows the volume swept to be calculated, which can then be combined with the ash mass impact rate to derive the volumetric mass concentration. Combining the detection of a certain volumetric concentration of VA with the GPS location of the aircraft and a database of known volcano GPS coordinates can assess the proximity of the aircraft to the source. Further combining the VA volumetric mass concentration, proximity to the source information, and wind direction data can form the basis for pilot guidance for the most expedient exit from the encountered plume. Additionally, for those encounters with VA which are not hazardous, combining the ash mass exposure data with engine performance data, such as hours run and power settings, can provide guidance for maintenance actions for the ground staff.

We recognise the limitations of the equipment, such as the inability to capture particles after the impact with the target and poor airflow control, and further recognise the impact these limitations pose on the accuracy of numerical findings of this study. We would propose the following improvements:-

- a) The particulate dispensing system should be redesigned to provide a smaller sample and in a more uniform airflow.
- b) The high-pressure airflow system requires expanding to generate a larger uniform impact area and improved extraction system.
- c) The target mounting requires redesign to improve insulation.
- d) The enclosure system requires improved screening and calibration for resistance to ground of the target and the capacitance of the target to ground.

Further work is required to characterise the energy required to fracture ash of particular size, whilst further looking at the variables of the impact angle and higher velocities. Also if we consider the charging behaviour seen to be due to fracto-emission, then the differing charging behaviour measured on dissimilar targets impacted by the same particulate raises the question of the influence of the target material's mechanical properties on the impact outcome. Properties such as hardness, brittleness, surface finish and toughness need to be considered.. Other variables that could affect charging such as: the mineral composition of the VA; the

water content of the VA; the charging influence of the removal of target material by erosion, could also be investigated.

6 Appendix

A. Revision 1 high-pressure air nozzle parts, assembly and description.

Revision 1 of the nozzle assembly consisted of a machined base fitting, and a straight, parallel sided, copper tube jet pipe (12 mm OD; 10 mm ID). The base incorporated a threaded fitting for the quick disconnect for the air supply, a replaceable flat plate metering orifice, four radial feed holes to feed the sample into the low pressure area downstream of the orifice plate, and fixings for the copper jet pipe (Figures 81 to 85). The copper jet pipe was drilled in four places at the lower end to match the radial feed holes in the base fitting. The jet pipe was a sealed fit into the target enclosure (Figure 83) This assembly was based upon the design detailed in Xie et al. (2011)



Figure 81 - View of revision 1 nozzle assembly with feed cone in place.



Figure 82 - View of revision 1 nozzle assembly from above with feed cone in place.

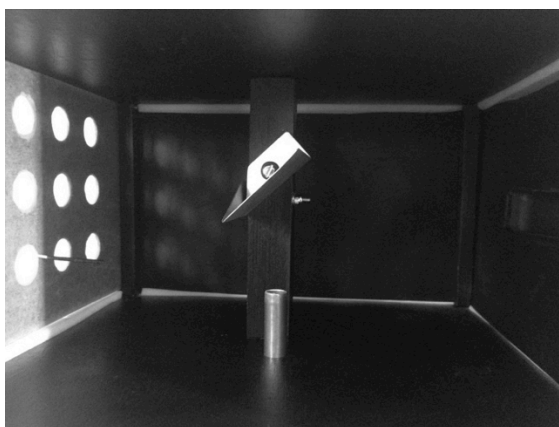


Figure 83 - View of the revision 1 jet pipe installation into the revision 1 target enclosure.

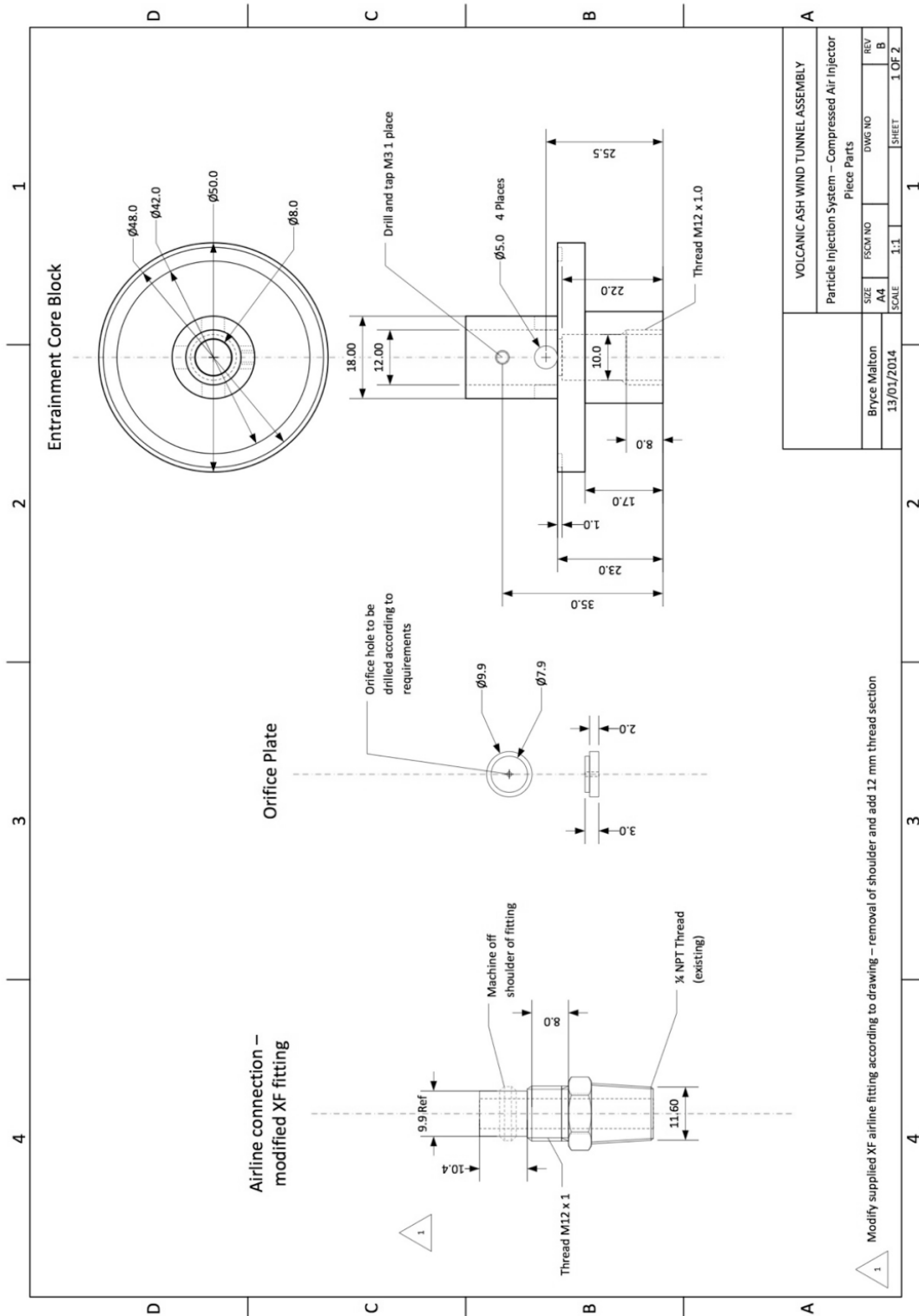


Figure 84 - Revision 1 high-pressure air nozzle piece parts.

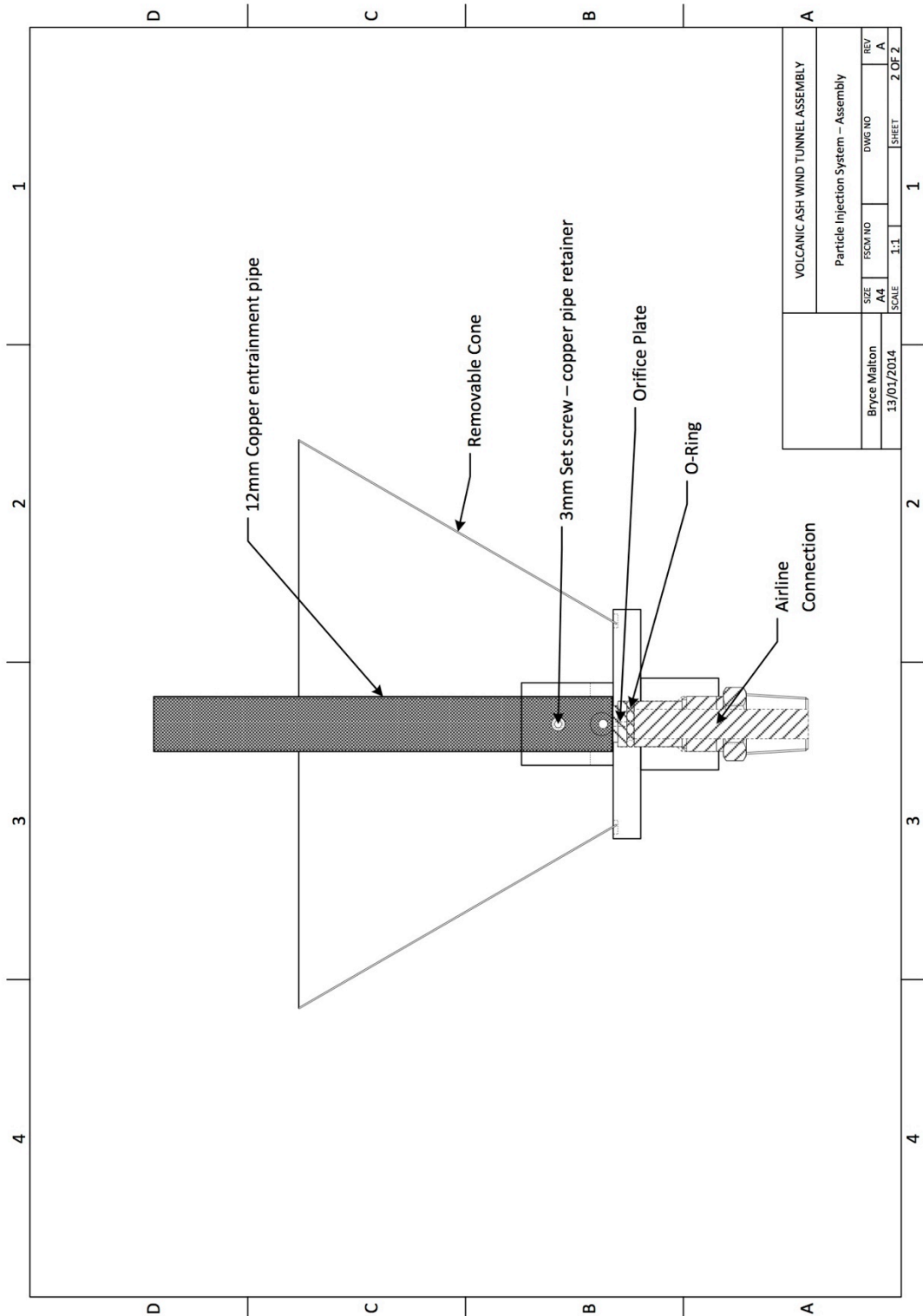


Figure 85 - Revision 1 high-pressure air nozzle general assembly.

B. Revision 2 high-pressure air nozzle parts, assembly and description.

Revision 2 modified the high-pressure air system by the removal of the feed hopper and the fitting a single side feed tube in place of the radial feedholes. The copper jet pipe was modified to accommodate the new side feed tube whilst blocking the redundant feedholes (Figures 86 to 90).



Figure 86 - A view of the revision 2 high-pressure nozzle arrangement.

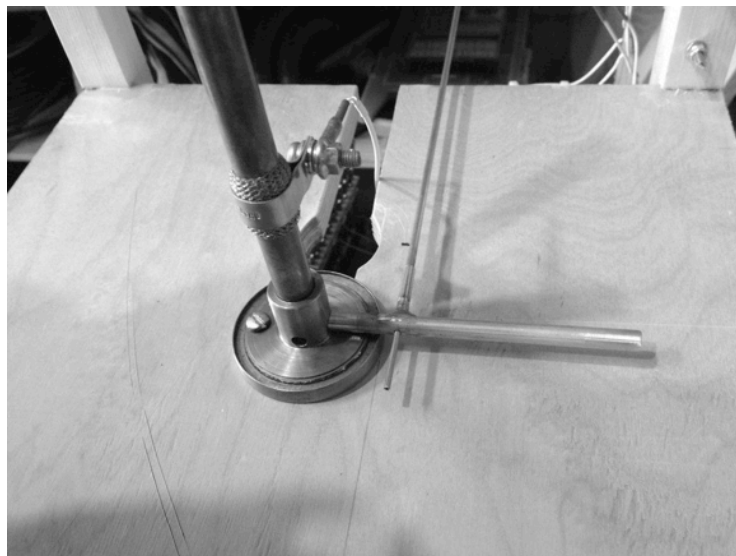


Figure 87 - A view of the revision 2 high-speed nozzle arrangement with a prototype side feeder tube and cartridge installed.

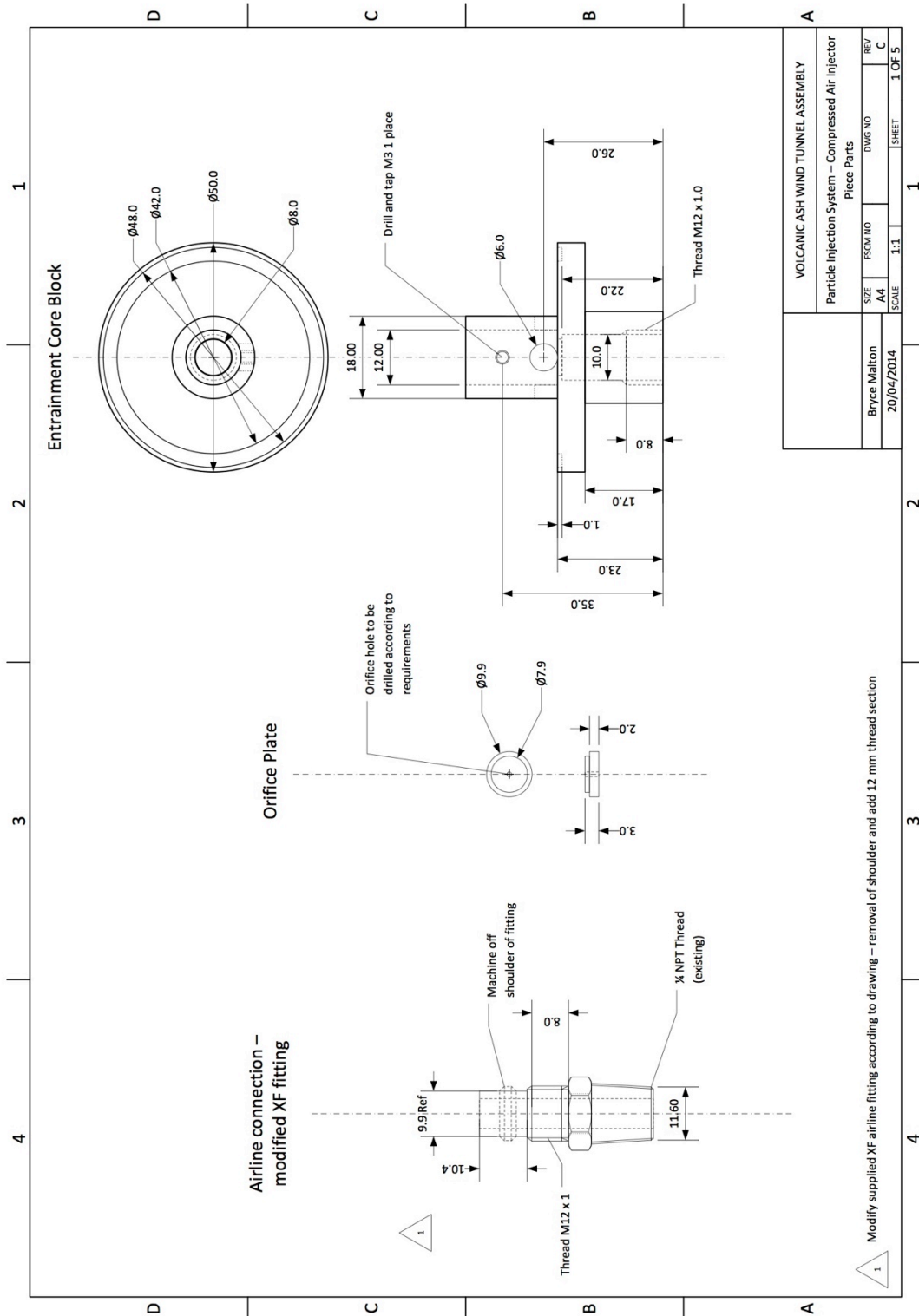


Figure 88 - Revision 2 high-pressure nozzle piece parts.

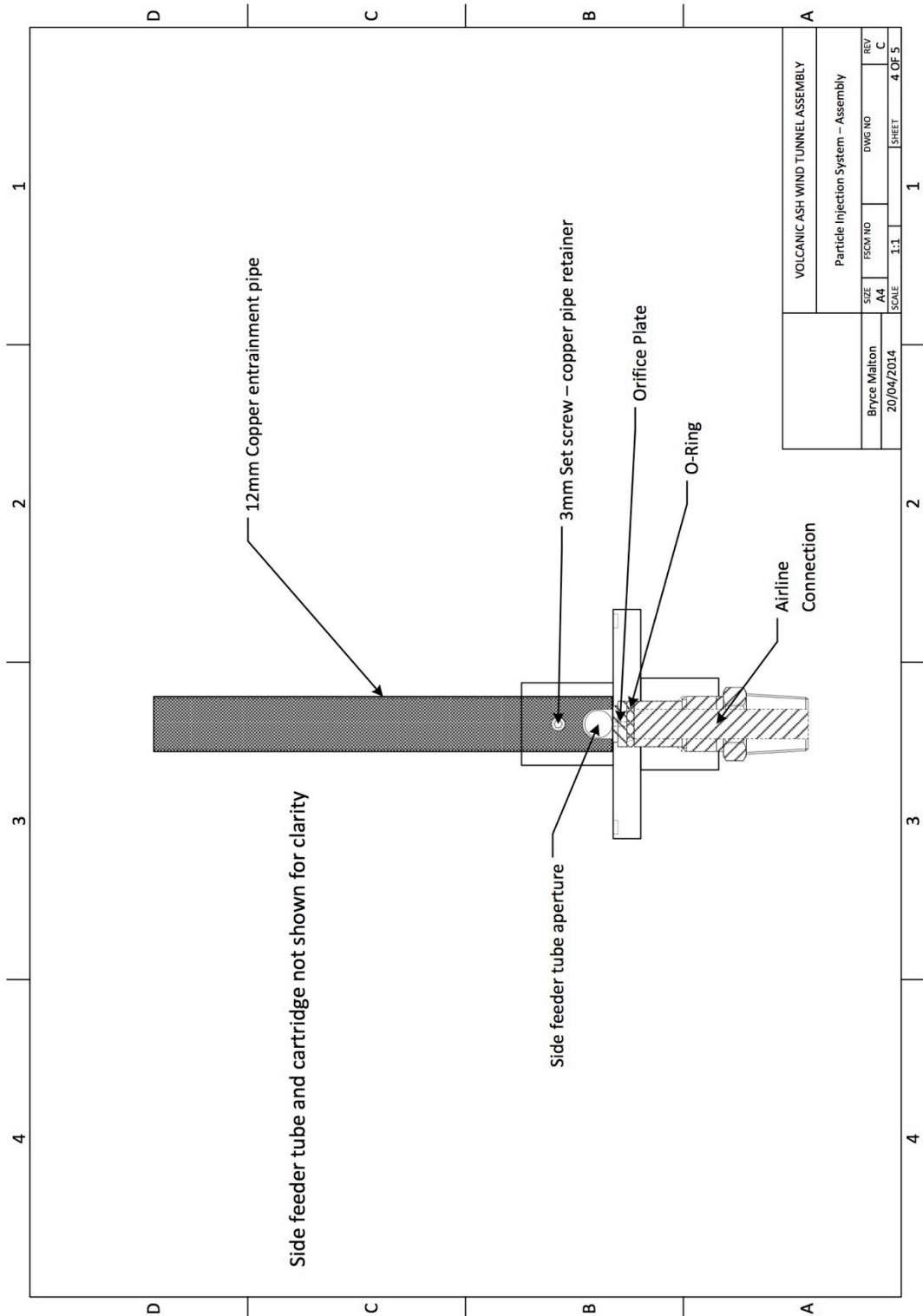


Figure 89 - Revision 2 high-pressure air nozzle general assembly.

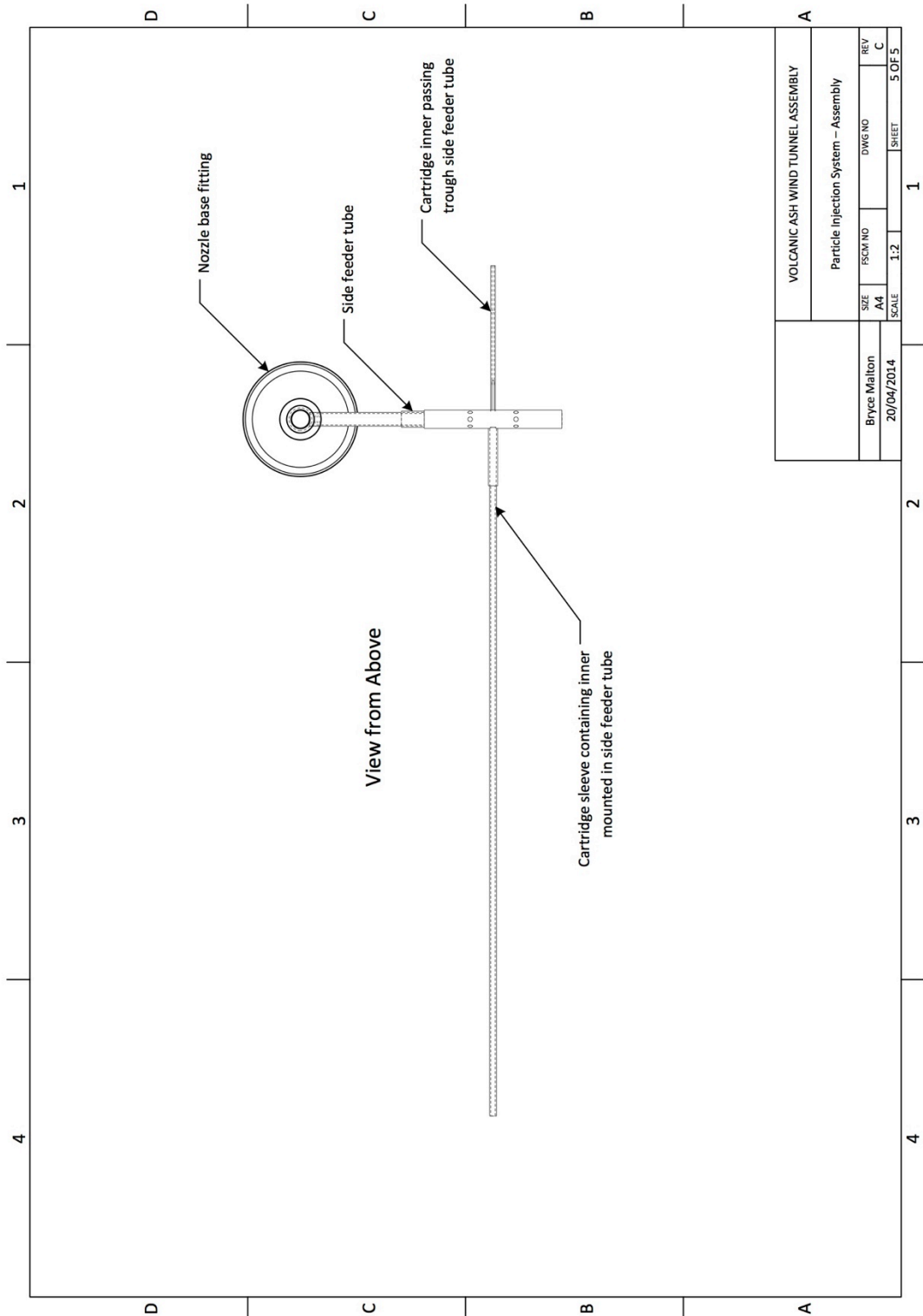


Figure 90 - Revision 2 high-pressure air nozzle view from above showing the general arrangement of the side feeder tube installation.

C. Revision 3 high-pressure air nozzle parts, assembly and description.

Revision 3 removed the aperture for the side feeder tube, as the feeder cartridge was now located in the upper nozzle fitting, and removed the replaceable orifice plate from the nozzle base assembly, as the restrictor aperture was relocated to the upper nozzle fitting. The sealed entry to the target enclosure shown in Figure 83 was abandoned in favour of a design to entrain atmospheric air from outside the enclosure at the exit of the nozzle in an attempt to create an 'air wall' around the high-speed flow. This was achieved by incorporating a 30° external taper at the exit of the nozzle, and mating this to a 15mm dia. copper tube shroud. The copper jet pipe linking the base fitting to the new upper nozzle fitting was shortened to accommodate the new upper fitting. The new upper fitting also incorporated a 3 mm fixed orifice, and a crosswise mounting for the sample cartridge (Figures 91 to 93) and the general arrangement shown in Figure 11.



Figure 91 - The revision 3 nozzle upper fitting.



Figure 92 - The revision 3 upper fitting with the mating entrainment shroud in place.

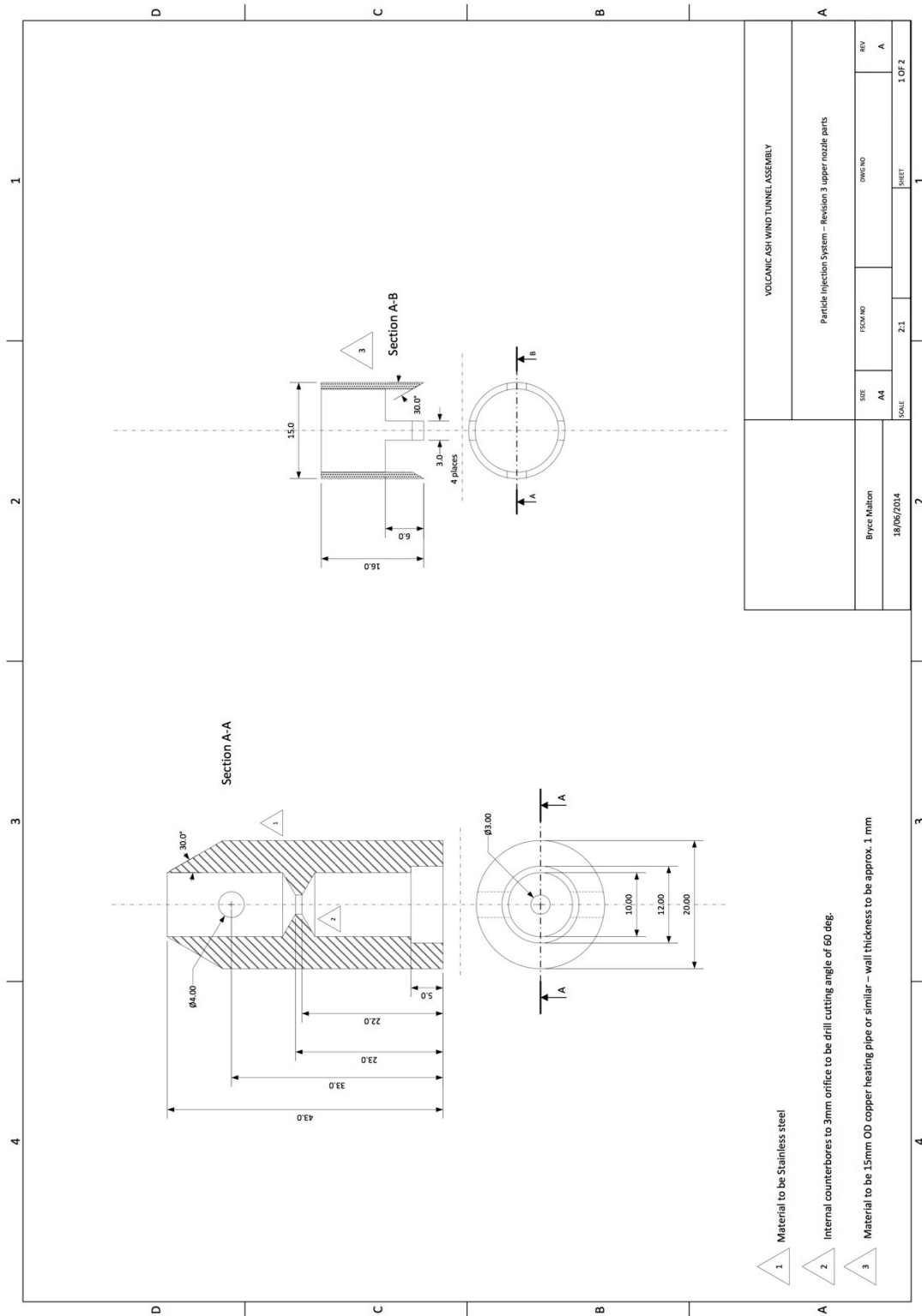


Figure 93 – Revision 3 high-pressure air nozzle upper section piece parts.

D. Revision 4 high pressure air upper nozzle parts.

Revision 4 removed the crossways mounting of the sample feed cartridge and returned to a side feeder tube configuration, but mounted at 30° to the flow and at the nozzle exit. The fixed orifice was also reduced to slightly over 2 mm to improve pressure retention, and it was lowered in the throat of the nozzle to accommodate the side feeder tube.

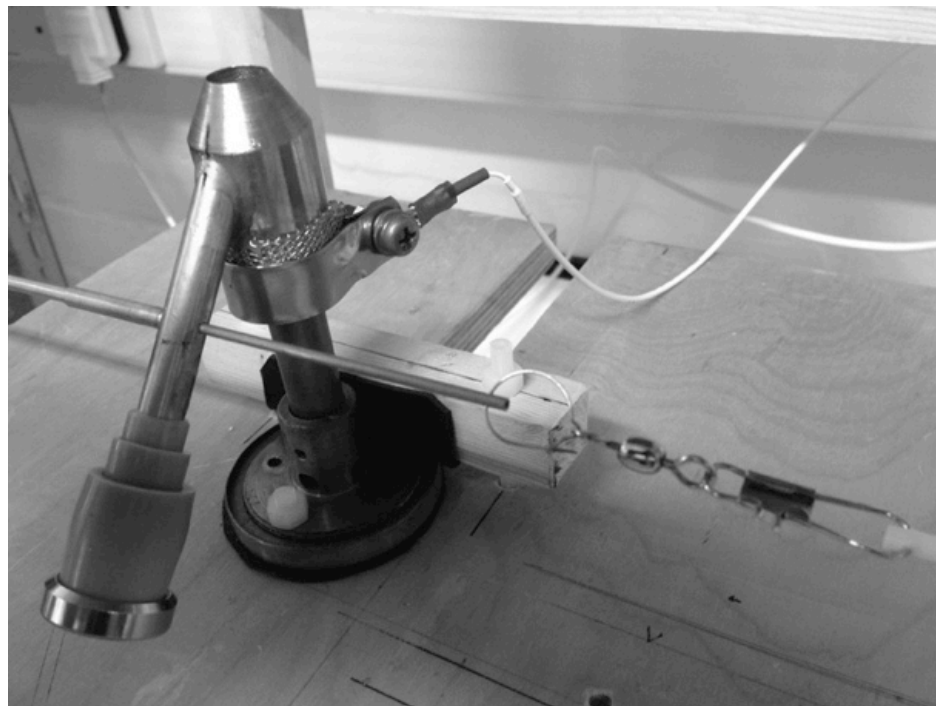


Figure 94 - View of the revision 4 high-pressure air nozzle with angled side feeder tube.

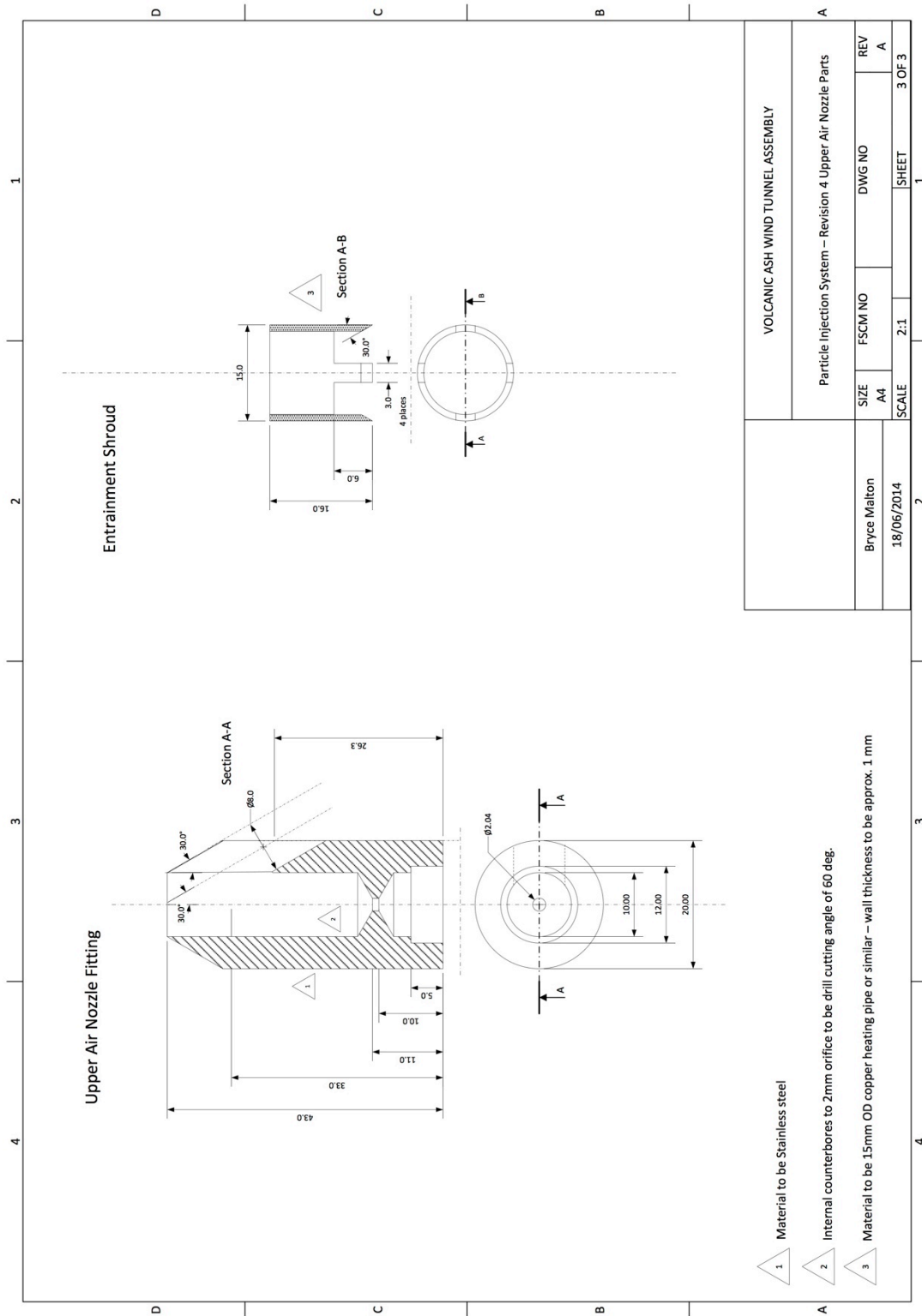


Figure 95 - The revision 4 high-speed airflow nozzle piece parts.

E. Revision 2 side feeder tube assembly – sample cartridge detail.

The tubular cartridge consisted of two parts: an outer plain brass tube sleeve 3 mm OD / 2 mm ID 300 mm long and an inner sample carrier fabricated from 2 mm OD / 1 mm ID brass tube 300 mm long. The inner carrier tube was slotted lengthwise for 200 mm and the slot sealed at each end by solder. The end of the carrier was drilled crosswise 0.75 mm dia. to accept the draw-wire system (Figure 96 and 97). The inner carrier would be loaded with sample material (Figure 14) and slid inside the outer sleeve, leaving the draw-wire connection visible. The opposite end of the sleeve would be sealed with a bung to prevent airflow down the tube. The cartridge assembly would then be located into the mounting in the side feeder tube, with the inner projecting through to be connected to the draw-wire (Figures 16 and 15).

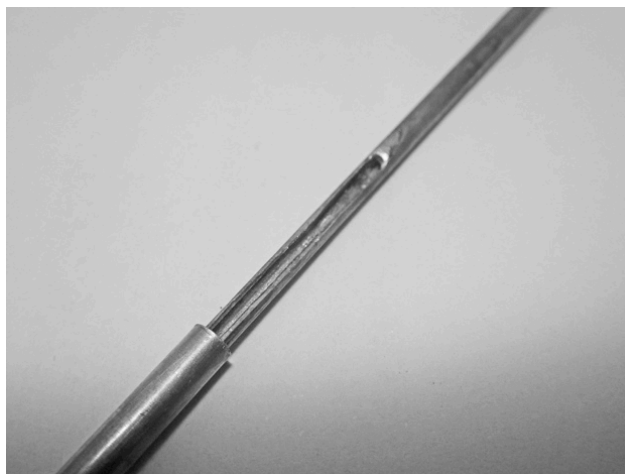
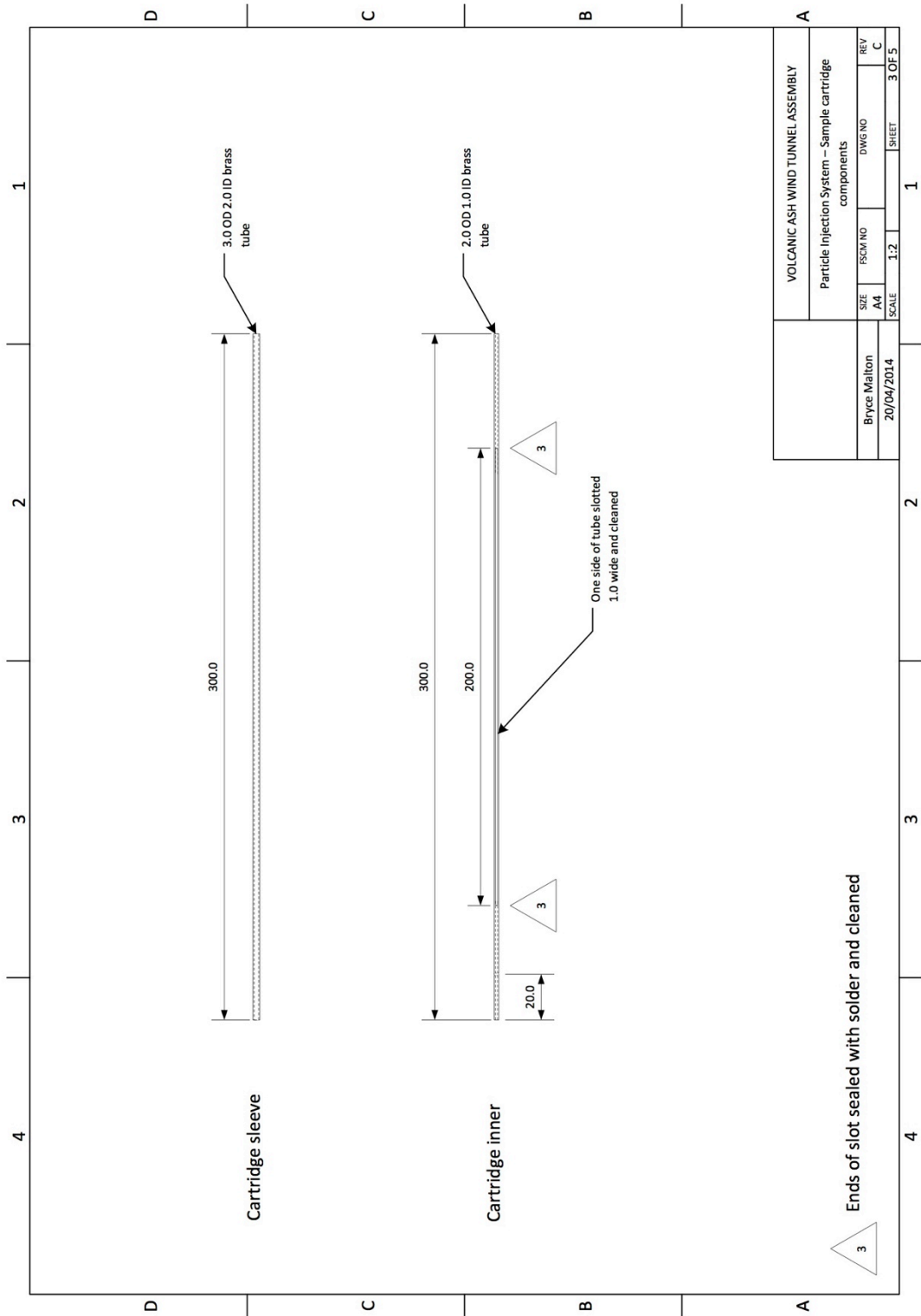


Figure 96 - Detail view of the sample cartridge inner and sleeve.



VOLCANIC ASH WIND TUNNEL ASSEMBLY		1:2		1	
Particle Injection System - Sample cartridge components					
SIZE	FSCM NO	DWG NO	REV		
A4			C		
Bryce Mallon			SCALE	3 OF 5	
20/04/2014					

Ends of slot sealed with solder and cleaned

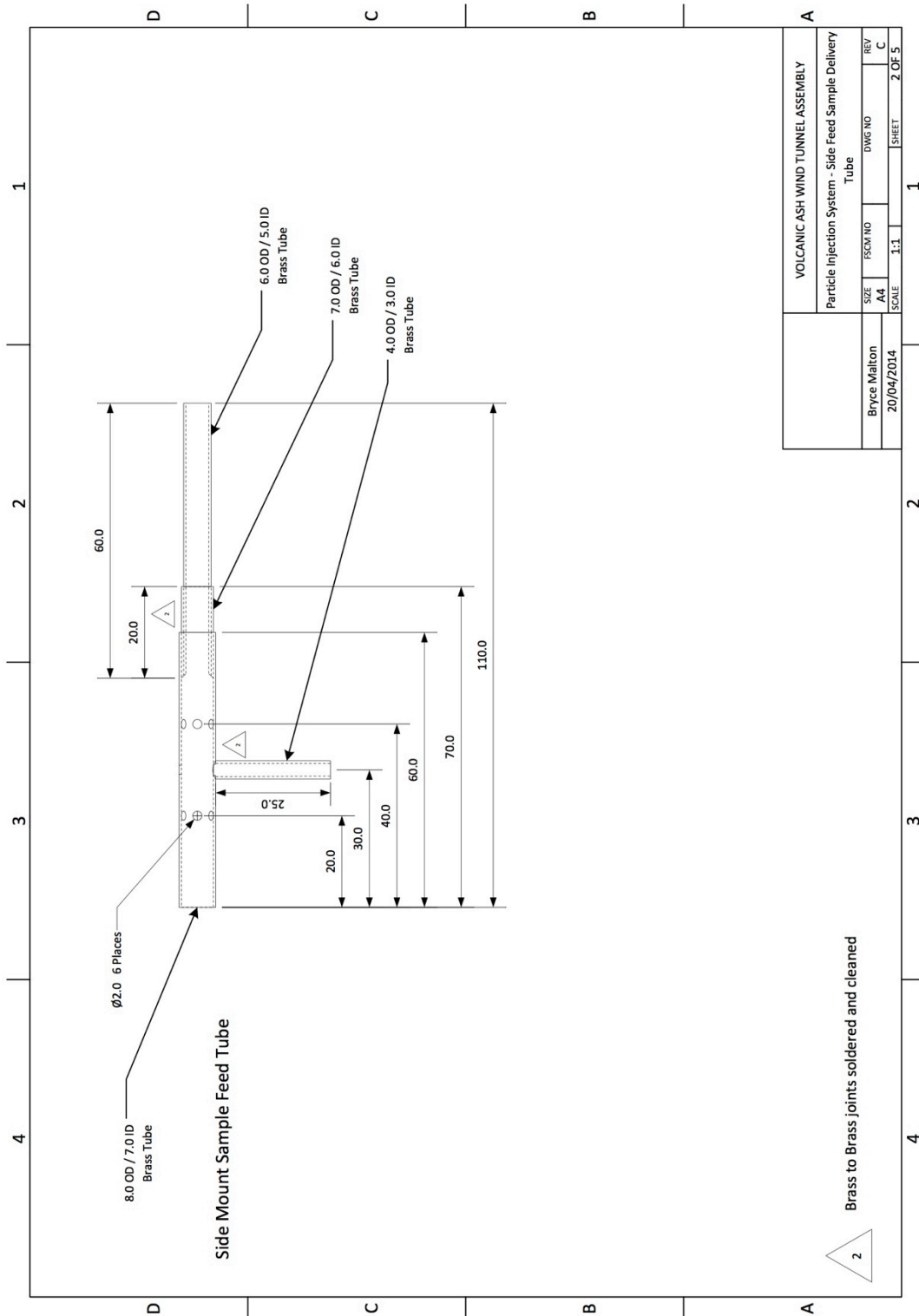
Figure 97 – Sample feed cartridge piece part drawing.

F. Revision 2 side feeder tube assembly – feeder tube detail.

The initial side feeder tube was a simple straight brass tube 6 mm OD / 5 mm ID with a 2 mm cross drill to accept the sample cartridge. However in efforts to reduce the energy of the lofting process, and hence reduce the fracture probability and charging within the feeder system, the side tube was developed to include: a side mounting tube for the cartridge assembly; a stepped design to increase the cross section at the lofting point; radial ventilation holes to aid turbulation upstream and downstream of the lofting point (Figures 98, 99 and 13).



Figure 98 - View of a final revision 2 of particulate sample side feeder tube (Note angled cut off and plastic sleeve are later modifications).



VOLCANIC ASH WIND TUNNEL ASSEMBLY	
Particle Injection System - Side Feed Sample Delivery Tube	
SIZE A4	DWG NO
SCALE 1:1	REV C
Bryce Mailton 20/04/2014	SHEET 2 OF 5

Figure 99 - Revision 2 Side feeder tube detail drawing.

G. Revision 2 side feeder tube assembly – draw wire system.

The draw-wire system was designed around a small DC motor (Igarashi 262-56 geared at a ratio of 1953:1), which has an output shaft speed of 2 RPM at 12 V. A 50 mm dia. aluminium pulley was fixed to the output shaft, around which was wrapped the plastic coated multi-stranded steel draw-wire. A 0-30 V constant voltage, current limited, bench power supply, which was controllable to ± 0.01 V, supplied the power to the motor. The draw wire connected to the cartridge inner using commercial swivels and steel spring clips. The draw wire was electrically isolated from the cartridge by a silicon rubber tube link in the connection (Figures 100 and 101 for detail views).

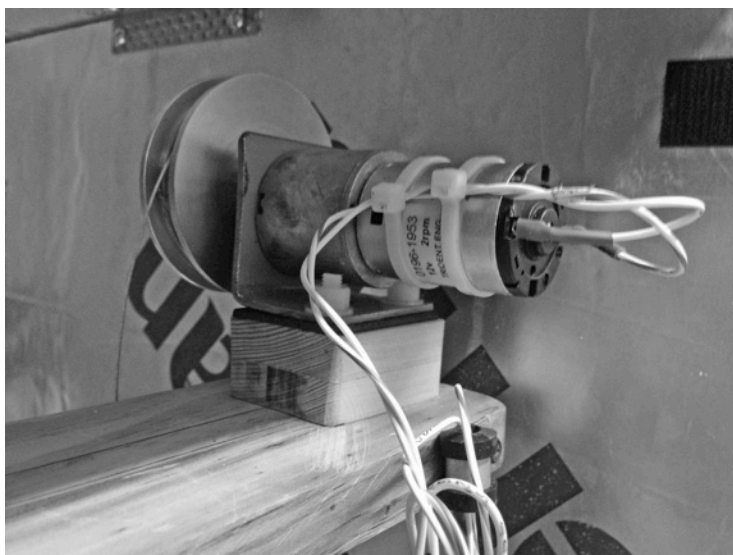


Figure 100 - The DC electric draw-wire motor with attached 50mm pulley.

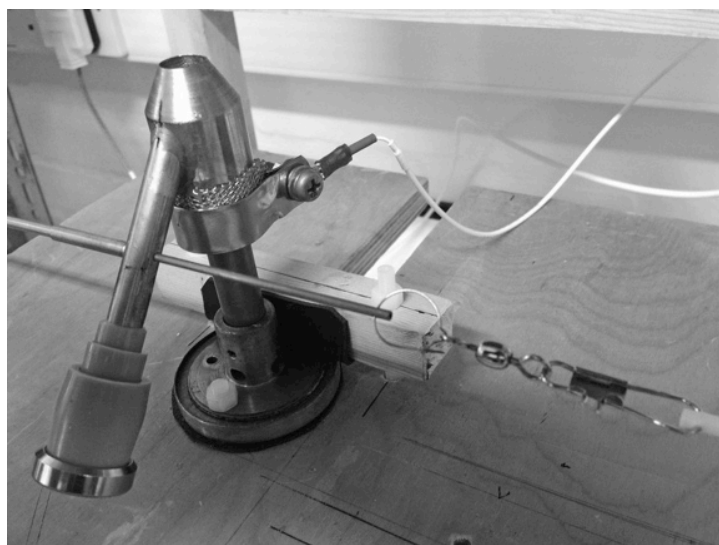
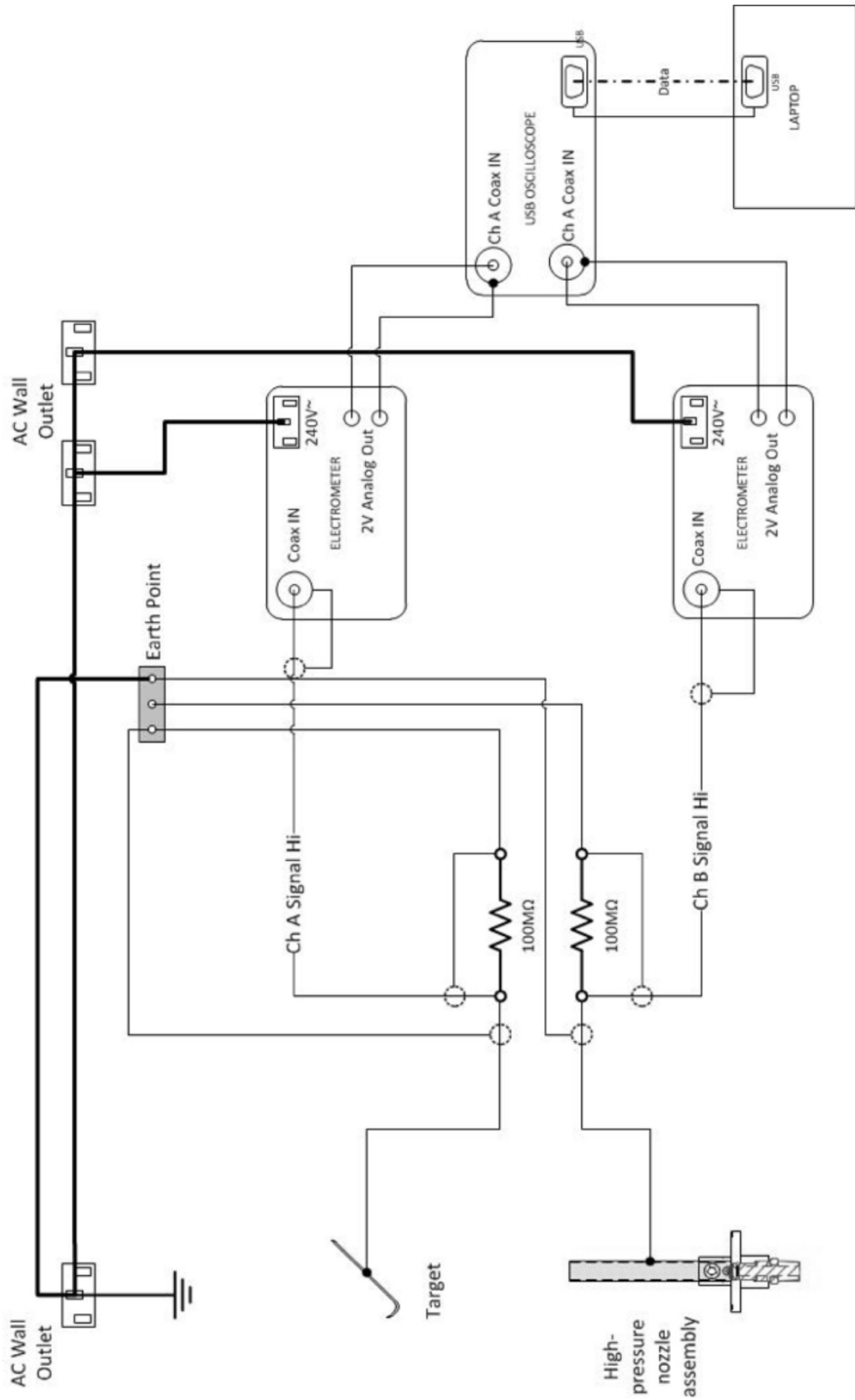
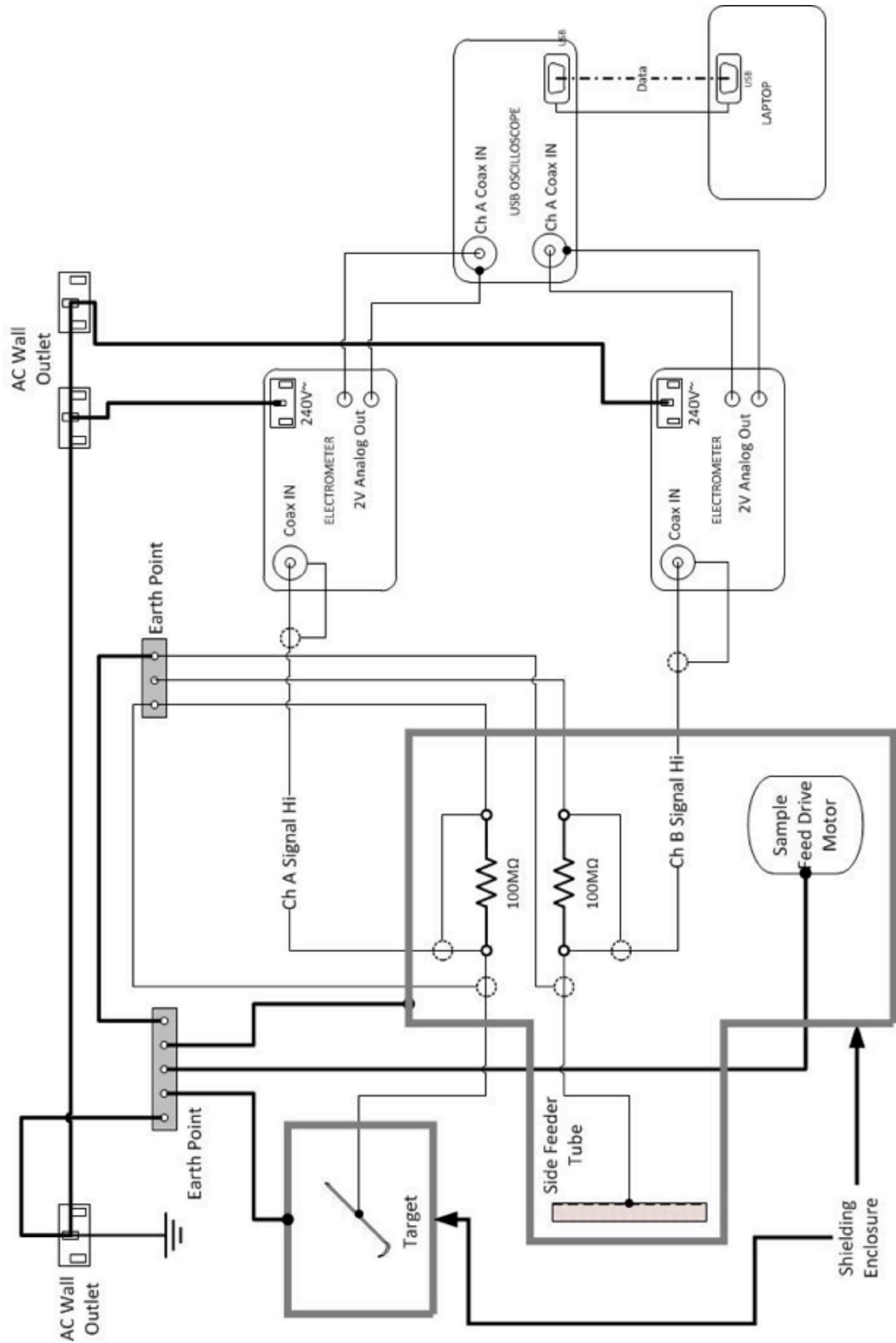


Figure 101 – View showing the connection of the draw-wire to the particulate sample cartridge.

H. Revision 1 Wiring and Earthing Diagram.



I. Revision 2 wiring and earthing diagram.



J. Revision 1 target enclosure detail.

The revision 1 enclosure consisted of a plywood box 300 mm x 300 mm x 150 mm with a central wood pillar to act as the target mounting. A hole was drilled in the base to allow the entry of the high-pressure nozzle. The right side vertical face of the box held the extraction vent for the vacuum extraction, and the opposite vertical face was drilled with multiple holes to allow the entry of external air. The target was mounted with the face angled towards the extraction suction side. The design intent was the extraction system would create a cross flow in the box that would direct the particulate-laden air away from the target after the flow had impacted the face. The rear face of the enclosure was solid and the front face transparent to allow viewing of the target (Figure 83). The interior of the enclosure was painted matt black to give optimum visibility of light coloured particulate.

The enclosure was mounted on a frame with a lower platform to which the high-pressure nozzle and particle feeder system was attached (Figure 102).



Figure 102 - The revision 1 enclosure and mounting frame (with revision 1 particle feed system in place).

K. Revision 2 target enclosure detail.

Revision 2 introduced a hollow square frustrum extraction contraction downstream of the target, and the left side vertical panel was replaced with an aluminium 12.5 mm honeycomb panel (Figures 103 and 104)

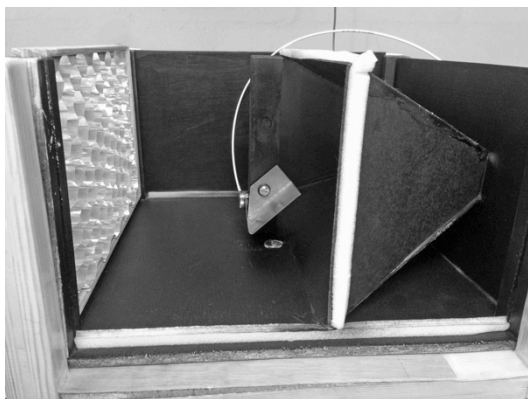


Figure 103 - The revision 2 enclosure with square frustrum extraction contraction and honeycomb air inlet.

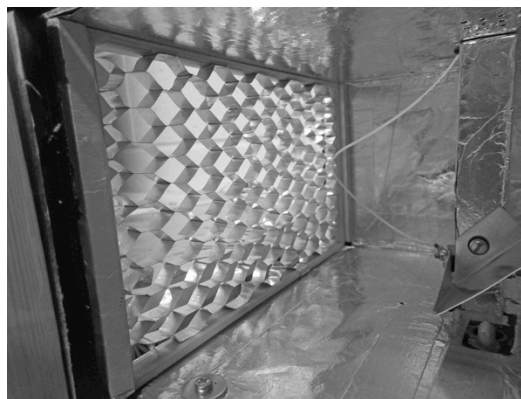


Figure 104 - View of the honeycomb inlet panel.

Revision 2 of the enclosure coincided with incorporation of revision 3 of the high-pressure air nozzle. This resulted in the target being lowered, the enlargement of the hole in the base of the unit, and the bonding in of the entrainment shroud (Figures 92, 11 and 103). Revision 2 also introduced electrical isolation of the enclosure from the mounting frame. This was accomplished by lining all the mating surfaces of the mounting frame with PTFE adhesive tape. The high-pressure nozzle was attached to the lower platform using nylon hardware and a wood clamp block (Figure 94). All joints between the high-pressure nozzle and the mounting frame were insulated with rubber sheet. The sample feeder drive motor was mounted on a wood extension beam. The motor was also electrically isolated from the beam using rubber sheet (Figures 100 and 17).

L. Table of pressure sensor outputs with corresponding inlet pressure expressed as airspeed, calculated from the manufacturer transform function (Freescale Semiconductor, 2012).

Sensor output voltage / V (step = 0.0015 V)	Input pressure expressed as airspeed calculated from the transfer function / m s⁻¹
1.7591	-64.8579
1.7876	-63.6094
1.8161	-62.3350
1.8446	-61.0331
1.8731	-59.7019
1.9016	-58.3393
1.9301	-56.9432
1.9586	-55.5110
1.9871	-54.0399
2.0156	-52.5265
2.0441	-50.9670
2.0726	-49.3572
2.1011	-47.6919
2.1296	-45.9651
2.1581	-44.1695
2.1866	-42.2965
2.2151	-40.3352
2.2436	-38.2720
2.2721	-36.0895
2.3006	-33.7645
2.3291	-31.2654
2.3576	-28.5463
2.3861	-25.5370
2.4146	-22.1196
2.4431	-18.0638
2.4716	-12.7753
2.5001	0.0000

Sensor output voltage / V (step = 0.0015 V)	Input pressure expressed as airspeed calculated from the transfer function / m s⁻¹
2.5286	12.7753
2.5571	18.0638
2.5856	22.1196
2.6141	25.5370
2.6426	28.5463
2.6711	31.2654
2.6996	33.7645
2.7281	36.0895
2.7566	38.2720
2.7851	40.3352
2.8136	42.2965
2.8421	44.1695
2.8706	45.9651
2.8991	47.6919
2.9276	49.3572
2.9561	50.9670
2.9846	52.5265
3.0131	54.0399
3.0416	55.5110
3.0701	56.9432
3.0986	58.3393
3.1271	59.7019
3.1556	61.0331
3.1841	62.3350
3.2126	63.6094
3.2411	64.8579

M. Results of the timed calibration tests of the sample draw-wire system

12 V Motor Input

Distance drawn / mm	Cumulative time / s	Velocity mm s ⁻¹	
50	9.34	5.35	
50	9.59	5.21	
50	9.5	5.26	
100	18.87	5.30	
100	19.06	5.25	
100	18.75	5.33	
150	28.28	5.30	
150	28.65	5.24	
150	27.87	5.38	
200	37.53	5.33	
200	37.5	5.33	
Av. velocity mm s ⁻¹		5.29	
Max / Min velocity mm s ⁻¹		5.38	5.21
Max / Min error / %		1.6	1.6

11 V Motor Input

Distance drawn / mm	Cumulative time / s	Velocity mm s ⁻¹	
50	10.4	4.81	
50	10.3	4.85	
50	10.1	4.96	
100	20.3	4.92	
100	20.5	4.87	
100	20.4	4.91	
150	30.9	4.85	
150	30.6	4.90	

Distance drawn / mm	Cumulative time / s	Velocity mm s ⁻¹	
150	30.4	4.94	
200	41.8	4.79	
200	41.0	4.88	
200	40.8	4.91	
Av. velocity mm s ⁻¹		4.88	
Max / Min velocity mm s ⁻¹ ₁		4.96	4.79
Max / Min error / %		1.5	2.0

10 V Motor Input

Distance drawn / mm	Cumulative time / s	Velocity mm s ⁻¹	
50	11.2	4.47	
50	11.5	4.34	
50	11.3	4.43	
100	23.0	4.35	
100	22.8	4.38	
100	22.8	4.40	
150	34.1	4.40	
150	34.0	4.41	
150	34.1	4.40	
200	46.0	4.34	
200	45.6	4.39	
200	46.1	4.34	
Av. velocity mm s ⁻¹		4.39	
Max / Min velocity mm s ⁻¹		4.43	4.34
Max / Min error / %		1.0	1.1

9 V Motor Input

Distance drawn / mm	Cumulative time / s	Velocity mm s⁻¹	
50	12.6	3.96	
50	12.8	3.89	
50	12.7	3.95	
100	25.2	3.97	
100	26.4	3.79	
100	25.0	4.00	
150	38.1	3.94	
150	38.0	3.95	
150	37.8	3.97	
200	51.3	3.90	
200	51.5	3.89	
200	50.8	3.93	
Av. velocity mm s ⁻¹		3.93	
Max / Min velocity mm s ⁻¹		4.00	3.79
Max / Min error / %		1.8	3.6

8 V Motor Input

Distance drawn / mm	Cumulative time / s	Velocity mm s⁻¹	
50	14.4	3.47	
50	14.5	3.45	
50	14.1	3.54	
100	28.8	3.47	
100	28.9	3.46	
100	28.6	3.49	
150	43.0	3.49	
150	43.5	3.45	
150	43.2	3.48	
200	57.8	3.46	

Distance drawn / mm	Cumulative time / s	Velocity mm s ⁻¹	
200	58.0	3.45	
200	57.8	3.46	
Av. velocity mm s ⁻¹		3.01	
Max / Min velocity mm s ⁻¹		3.03	2.99
Max / Min error / %		0.5	0.7

7 V Motor Input

Distance drawn / mm	Cumulative time / s	Velocity mm s ⁻¹	
50	16.6	3.01	
50			
50	16.7	2.99	
100	33.0	3.03	
100	33.1	3.02	
100	33.1	3.02	
150	50.0	3.00	
150	49.8	3.01	
150	49.6	3.02	
200	66.5	3.01	
200	66.5	3.01	
200	66.3	3.02	
Av. velocity mm s ⁻¹		3.47	
Max / Min velocity mm s ⁻¹		3.54	3.47
Max / Min error / %		2.0	0.8

6 V Motor Input

Distance drawn / mm	Cumulative time / s	Velocity mm s ⁻¹	
50	19.2	2.60	

Distance drawn / mm	Cumulative time / s	Velocity mm s ⁻¹	
50	19.7	2.54	
50	19.8	2.53	
100	38.6	2.59	
100	39.4	2.54	
100	39.3	2.54	
150	57.6	2.61	
150	58.8	2.55	
150	59.1	2.54	
200	77.3	2.59	
200	78.6	2.54	
200	79.7	2.51	
Av. velocity mm s ⁻¹		2.56	
Max / Min velocity mm s ⁻¹		2.61	2.51
Max / Min error / %		1.9	1.8

N. Theoretical maximum charge held per mg of particulate.

Table 13 - Theoretical maximum charge per mg of dispersed E15 ash density 2800 kg m⁻³.

Particle size band Dia. /μm	Number of particles in the band	Total charge of the band.	Total charge of the band.	Total charge of the band.
		Surface charge 10 μC m ⁻² values / C	Surface charge 27 μC m ⁻² values / C	Surface charge i.a.w. Eq (1.7) /C
0.01 - 1	5.09E+10	1.60E-08	4.31E-08	2.03E-06
1 - 2.5	3.86E+07	3.03E-09	8.18E-09	1.68E-07
2.5 - 5	2.25E+06	8.84E-10	2.39E-09	3.86E-08
5 - 7.5	2.42E+05	2.85E-10	7.69E-10	1.05E-08
7.5 - 10	6.11E+04	1.44E-10	3.89E-10	4.80E-09
10 - 12.5	2.26E+04	8.89E-11	2.40E-10	2.75E-09
12.5 - 15	1.05E+04	6.16E-11	1.66E-10	1.79E-09
15 - 17.5	5.56E+03	4.58E-11	1.24E-10	1.27E-09
17.5 - 20	3.23E+03	3.55E-11	9.59E-11	9.40E-10
20 - 22.5	2.00E+03	2.83E-11	7.63E-11	7.20E-10
22.5 - 25	1.29E+03	2.29E-11	6.17E-11	5.63E-10
25 - 27.5	8.66E+02	1.87E-11	5.05E-11	4.47E-10
27.5 - 30	5.94E+02	1.54E-11	4.16E-11	3.58E-10
30 - 32.5	4.17E+02	1.28E-11	3.45E-11	2.90E-10
32.5 - 35	2.97E+02	1.06E-11	2.87E-11	2.35E-10
35 - 37.5	2.15E+02	8.87E-12	2.39E-11	1.92E-10
37.5 - 40	1.58E+02	7.45E-12	2.01E-11	1.58E-10
40 - 42.5	1.17E+02	6.25E-12	1.69E-11	1.30E-10
42.5 - 45	8.80E+01	5.29E-12	1.43E-11	1.08E-10
45 - 47.5	6.60E+01	4.43E-12	1.20E-11	8.94E-11
47.5 - 50	5.00E+01	3.73E-12	1.01E-11	7.41E-11
50 - 52.5	3.80E+01	3.13E-12	8.46E-12	6.13E-11
52.5 - 55	3.00E+01	2.72E-12	7.35E-12	5.25E-11
55 - 57.5	2.30E+01	2.29E-12	6.17E-12	4.35E-11
57.5 - 60	1.80E+01	1.95E-12	5.27E-12	3.66E-11
60 - 62.5	1.40E+01	1.65E-12	4.45E-12	3.06E-11
62.5 - 250	1.20E+01	5.89E-12	1.59E-11	8.81E-11
TOTAL		2.07E-08	5.59E-08	2.26E-06

Table 14 - Theoretical maximum charge per mg of dispersed Sak ash with density
2800 kg m⁻³

Particle size band Dia. /μm	Number of particles in the band	Total charge of the band.	Total charge of the band.	Total charge of the band.
		Surface charge 10 μC m ⁻² values / C	Surface charge 27 μC m ⁻² values / C	Surface charge i.a.w. Eq (1.7) /C
0.01 - 1	4.10E+10	1.29E-08	3.48E-08	1.64E-06
1 - 2.5	2.95E+07	2.32E-09	6.25E-09	1.29E-07
2.5 - 5	1.74E+06	6.83E-10	1.84E-09	2.98E-08
5 - 7.5	1.78E+05	2.09E-10	5.65E-10	7.74E-09
7.5 - 10	4.20E+04	9.90E-11	2.67E-10	3.30E-09
10 - 12.5	1.67E+04	6.55E-11	1.77E-10	2.02E-09
12.5 - 15	8.95E+03	5.27E-11	1.42E-10	1.53E-09
15 - 17.5	5.54E+03	4.57E-11	1.23E-10	1.26E-09
17.5 - 20	3.67E+03	4.03E-11	1.09E-10	1.07E-09
20 - 22.5	2.51E+03	3.55E-11	9.57E-11	9.03E-10
22.5 - 25	1.75E+03	3.10E-11	8.36E-11	7.63E-10
25 - 27.5	1.24E+03	2.68E-11	7.25E-11	6.42E-10
27.5 - 30	8.92E+02	2.31E-11	6.24E-11	5.38E-10
30 - 32.5	6.47E+02	1.98E-11	5.35E-11	4.50E-10
32.5 - 35	4.74E+02	1.69E-11	4.57E-11	3.75E-10
35 - 37.5	3.50E+02	1.44E-11	3.90E-11	3.13E-10
37.5 - 40	2.60E+02	1.23E-11	3.31E-11	2.61E-10
40 - 42.5	1.95E+02	1.04E-11	2.81E-11	2.17E-10
42.5 - 45	1.47E+02	8.83E-12	2.38E-11	1.81E-10
45 - 47.5	1.12E+02	7.52E-12	2.03E-11	1.52E-10
47.5 - 50	8.50E+01	6.34E-12	1.71E-11	1.26E-10
50 - 52.5	6.60E+01	5.44E-12	1.47E-11	1.06E-10
52.5 - 55	5.10E+01	4.63E-12	1.25E-11	8.92E-11
55 - 57.5	3.90E+01	3.87E-12	1.05E-11	7.37E-11
57.5 - 60	3.10E+01	3.36E-12	9.07E-12	6.31E-11
60 - 62.5	2.40E+01	2.83E-12	7.63E-12	5.24E-11
62.5 - 250	2.20E+01	1.08E-11	2.92E-11	1.62E-10
TOTAL		1.66E-08	4.49E-08	1.82E-06

Table 15 - Theoretical maximum charge per mg of dispersed Sand with density 2600 kg m⁻³.

Particle size band Dia. /μm	Number of particles in the band	Total charge of the band.	Total charge of the band.	Total charge of the band.
		Surface charge 10 μC m ⁻² values / C	Surface charge 27 μC m ⁻² values / C	Surface charge i.a.w. Eq (1.7) /C
0.01 - 1	1.28E+11	4.04E-08	1.09E-07	5.13E-06
1 - 2.5	3.40E+07	2.67E-09	7.21E-09	1.48E-07
2.5 - 5	1.21E+06	4.74E-10	1.28E-09	2.07E-08
5 - 7.5	1.50E+05	1.77E-10	4.78E-10	6.54E-09
7.5 - 10	2.86E+04	6.75E-11	1.82E-10	2.25E-09
10 - 12.5	5.92E+03	2.32E-11	6.28E-11	7.18E-10
12.5 - 15	1.70E+03	9.98E-12	2.70E-11	2.90E-10
15 - 17.5	1.04E+03	8.58E-12	2.32E-11	2.37E-10
17.5 - 20	9.74E+02	1.07E-11	2.89E-11	2.83E-10
20 - 22.5	9.27E+02	1.31E-11	3.54E-11	3.34E-10
22.5 - 25	8.40E+02	1.48E-11	4.01E-11	3.66E-10
25 - 27.5	7.25E+02	1.57E-11	4.23E-11	3.74E-10
27.5 - 30	6.09E+02	1.58E-11	4.26E-11	3.67E-10
30 - 32.5	4.99E+02	1.53E-11	4.13E-11	3.47E-10
32.5 - 35	4.06E+02	1.45E-11	3.92E-11	3.22E-10
35 - 37.5	3.27E+02	1.35E-11	3.64E-11	2.93E-10
37.5 - 40	2.62E+02	1.23E-11	3.33E-11	2.63E-10
40 - 42.5	2.10E+02	1.12E-11	3.03E-11	2.34E-10
42.5 - 45	1.68E+02	1.01E-11	2.73E-11	2.07E-10
45 - 47.5	1.35E+02	9.07E-12	2.45E-11	1.83E-10
47.5 - 50	1.08E+02	8.06E-12	2.18E-11	1.60E-10
50 - 52.5	8.70E+01	7.17E-12	1.94E-11	1.40E-10
52.5 - 55	7.00E+01	6.35E-12	1.71E-11	1.22E-10
55 - 57.5	5.60E+01	5.56E-12	1.50E-11	1.06E-10
57.5 - 60	4.50E+01	4.88E-12	1.32E-11	9.15E-11
60 - 62.5	3.60E+01	4.24E-12	1.15E-11	7.86E-11
62.5 - 250	3.90E+01	1.91E-11	5.17E-11	2.86E-10
TOTAL		4.40E-08	1.19E-07	5.31E-06

O. The modelled effect on maximum charge capacity of a mixed grain size particulate.

Table 16 - A modelled example of the effect of breakage on the maximum charge capacity of a mixed grain size particulate. Data are for a particulate mass of 1 mg. The initial grain size distribution is as measured for E15 ash. The distribution after breakage has been based on reduced fraction above 10 μm dia. and increased $<1 \mu\text{m}$.


Size band μm	Number of particles in the band – unbroken initial distribution.	Total charge of the band. Surface charge i.a.w. Eq (1.7) /C	Number of particles in the band after breakage	Total charge of the band after breakage. Surface charge i.a.w. Eq (1.7) /C
0.01 - 1	5.09E+10	2.03E-06	6.82E+10	2.72E-06
1 - 2.5	3.86E+07	1.68E-07	3.86E+07	1.68E-07
2.5 - 5	2.25E+06	3.86E-08	2.25E+06	3.86E-08
5 - 7.5	2.42E+05	1.05E-08	2.42E+05	1.05E-08
7.5 - 10	6.11E+04	4.80E-09	6.11E+04	4.80E-09
10 - 12.5	2.26E+04	2.75E-09	2.13E+04	2.58E-09
12.5 - 15	1.05E+04	1.79E-09	9.82E+03	1.68E-09
15 - 17.5	5.56E+03	1.27E-09	5.22E+03	1.19E-09
17.5 - 20	3.23E+03	9.40E-10	3.03E+03	8.82E-10
20 - 22.5	2.00E+03	7.20E-10	1.88E+03	6.76E-10
22.5 - 25	1.29E+03	5.63E-10	1.21E+03	5.29E-10
25 - 27.5	8.66E+02	4.47E-10	8.13E+02	4.20E-10
27.5 - 30	5.94E+02	3.58E-10	5.58E+02	3.36E-10
30 - 32.5	4.17E+02	2.90E-10	3.91E+02	2.72E-10
32.5 - 35	2.97E+02	2.35E-10	2.79E+02	2.21E-10
35 - 37.5	2.15E+02	1.92E-10	2.02E+02	1.81E-10
37.5 - 40	1.58E+02	1.58E-10	1.48E+02	1.48E-10
40 - 42.5	1.17E+02	1.30E-10	1.10E+02	1.23E-10
42.5 - 45	8.80E+01	1.08E-10	8.20E+01	1.01E-10
45 - 47.5	6.60E+01	8.94E-11	6.20E+01	8.40E-11
47.5 - 50	5.00E+01	7.41E-11	4.70E+01	6.96E-11
50 - 52.5	3.80E+01	6.13E-11	3.60E+01	5.81E-11
52.5 - 55	3.00E+01	5.25E-11	2.80E+01	4.90E-11
55 - 57.5	2.30E+01	4.35E-11	2.20E+01	4.16E-11
57.5 - 60	1.80E+01	3.66E-11	1.70E+01	3.46E-11

60 - 62.5	1.40E+01	3.06E-11	1.30E+01	2.84E-11
62.5 - 250	1.20E+01	8.81E-11	1.10E+01	8.08E-11
<i>TOTAL</i>		<i>2.26E-06</i>		<i>2.96E-06</i>

7 References

- ACSS. 2014. *T³CAS Advanced Surveillance in One Integrated Package* [Online]. Phoenix AZ., USA: ACSS. Available: <http://www.acss.com/products/t3cas/> [Accessed 13 Dec. 2014 2014].
- AIRBUS. 2014. *New Airbus aircraft list prices for 2014* [Online]. Toulouse, France: Airbus. Available: <http://www.airbus.com/presscentre/pressreleases/press-release-detail/detail/new-airbus-aircraft-list-prices-for-2014/> [Accessed 20 Dec 2014 2014].
- AMAN, S., TOMAS, J., MÜLLER, P., KALMAN, H. & ROZENBLAT, Y. 2011. The Investigation of Breakage Probability of Irregularly Shaped Particles by Impact tests. *KONA Powder and Particle Journal*, 29, 224-235.
- ASCEND. 2014. *Flightglobal Fleet Forecast 2014 - 2033* [Online]. London UK. Available: http://img.en25.com/Web/flightglobal/%7B472dc513-dfc6-479d-9eca-1838b66cd7da%7D_FC069_ASCD_201408.pdf?elq=0e94ce836c6240f78ef3affca4a11406.
- AVILA, K., MOXEY, D., DE LOZAR, A., AVILA, M., BARKLEY, D. & HOF, B. 2011. The Onset of Turbulence in Pipe Flow. *Science*, 333, 192-196.
- BAILEY, A. 1993. Charging of solids and powders. *Journal of Electrostatics*, 30, 167-180.
- BAUMGARDNER, D. 2014. *Ice or Ash? Real-time Identification with the Next Generation IAGOS BCP* [Online]. MOZAIC/IAGOS Symposium 2014 Toulouse, France: Droplet Measurement Technologies. Available: http://www.iagos.fr/web/IMG/pdf/session3-3_baumgardner.pdf [Accessed 16 Dec 2014 2014].
- BAUMGARDNER, D. & NEWTON, R. 2014. *Optical particle detector*. USA patent application 14/05,165.
- BLEVINS, R. D. 1977. *Flow Induced Vibration*, New York, Van Nostrand Reinhold Co.
- BLYTHE, A. R. & REDDISH, W. 1979. Charges on powders and bulking effects. In: LOWELL, J. (ed.) *Electrostatics*. Bristol UK: Institute of Physics.
- BOND, J. W. 2008. On the electrical characteristics of latent finger mark corrosion of brass. *Journal of Physics D: Applied Physics*, 41, 125502.
- BRODER, I. 1990. The cost of accidental death: A capital market approach. *Journal of Risk and Uncertainty*, 3, 51-63.
- CAMPO-DEANO, L., GALINDO-ROSALES, F. J., PINHO, F. T., ALVES, M. A. & OLIVEIRA, M. S. N. 2012. Nanogel formation of polymer solutions flowing through porous media. *Soft Matter*, 8, 6445-6453.
- CARANTI, J. M., ILLINGWORTH, A. J. & MARSH, S. J. 1985. The charging of ice by differences in contact potential. *Journal of Geophysical Research: Atmospheres*, 90, 6041-6046.
- COSGROVE, M. 2010. *AF447: What is the price of a human life?* [Online]. Strasbourg, France: Le Figaro. Available: <http://plus.lefigaro.fr/note/af447-what-is-the-price-of-a-human-life-20100319-156039> [Accessed 20 Dec 2014 2014].

- CRESS, G. O., BRADY, B. T. & ROWELL, G. A. 1987. Sources of electromagnetic radiation from fracture of rock samples in the laboratory. *Geophysical Research Letters*, 14, 331-334.
- DERJAGUIN, B. V. & TOPOROV, Y. P. 1984. Comments on " the question of emission of charged particles in failure of solids" . *Journal of Materials Science*, 19, 2423-2426.
- DICKINSON, J., BRÄUNLICH, P., LARSON, L. & MARCEAU, A. 1978. Characteristic emission of negatively charged particles during tensile deformation of oxide-covered aluminum alloys. *Applications of Surface Science*, 1, 515-537.
- DICKINSON, J., JENSEN, L. & JAHAN - LATIBARI, A. 1984. Fracto - emission: The role of charge separation. *Journal of Vacuum Science & Technology A*, 2, 1112-1116.
- DICKINSON, J. T., DONALDSON, E. E. & PARK, M. K. 1981. The emission of electrons and positive ions from fracture of materials. *Journal of Materials Science*, 16, 2897-2908.
- DICKINSON, J. T., JENSON, L. C. & PARK, M. K. 1982. Time-of-flight measurements of the mass-to-charge ratio of positive ion emission accompanying fracture. *Journal of Materials Science*, 17, 3173-3178.
- DILLOW, C. 2010. *WHY CAN'T PLANES FLY THROUGH VOLCANIC ASH?* [Online]. New York , USA.: Popular Science. Available: http://www.popsci.com/sites/popsci.com/files/styles/medium_1x_/public/import/2013/images/2010/04/BA-engine.gif?itok=KER-JVBV [Accessed 4 Dec 2010 2010].
- EASTMENT, R. & MEE, C. 1973. Work function measurements on (100),(110) and (111) surfaces of aluminium. *Journal of Physics F: Metal Physics*, 3, 1738.
- ENOMOTO, Y. & HASHIMOTO, H. 1990. Emission of charged particles from indentation fracture of rocks. *Nature*, 346, 641-643.
- ENOMOTO, Y. & HASHIMOTO, H. 1992. Transient electrical activity accompanying rock under indentation loading. *Tectonophysics*, 211, 337-344.
- ERB, R. 1994. *Pitot-Static Instrument Calibration* [Online]. Experimental Aircraft Association. Available: <http://www.eaa1000.av.org/technical/instcal/instcal.htm> [Accessed 1st July 2014 2014].
- FEUERBACHER, B. & FITTON, B. 1972. Experimental investigation of photoemission from satellite surface materials. *Journal of Applied Physics*, 43, 1563-1572.
- FINLEY, J., WEY, T., KRONFELD, K. M. & KOENIGS, G. J. 2014. *System and method for monitoring hazards associated with static charge*. USA patent application 12/884,040.
- FREESCALE SEMICONDUCTOR. 2005. *Noise Considerations for Integrated Pressure Sensors* [Online]. Freescale Semiconductor. Available: http://cache.freescale.com/files/sensors/doc/app_note/AN1646.pdf [Accessed 15th Sept 2014 2014].
- FREESCALE SEMICONDUCTOR. 2012. *Technical data sheet MPXV7007* [Online]. Freescale Semiconductor. Available: http://cache.freescale.com/files/sensors/doc/data_sheet/MPXV7007.pdf [Accessed 01/04/2014 2014].

- FREUND, F. 2000. Time-resolved study of charge generation and propagation in igneous rocks. *Journal of Geophysical Research: Solid Earth*, 105, 11001-11019.
- FROESCHKE, S., KOHLER, S., P. WEBER, A. & KASPER, G. 2003. Impact fragmentation of nanoparticle agglomerates. *Journal of Aerosol Science*, 34, 275-287.
- GISLASON, S. R., HASSENKAM, T., NEDEL, S., BOVET, N., EIRIKSDOTTIR, E. S., ALFREDSSON, H. A., HEM, C. P., BALOGH, Z. I., K., D., OSKARSSON, N., SIGFUSSON, B., LARSEN, G. & STIPP, S. L. S. 2011. Characterisation of Eyjafjallajökull volcanic ash particles and a protocol for rapid risk assessment. *PNAS*, 108, 7307-7312.
- GRINDLE, T. J., BURCHAM, F. W. & HUGH, L. 2003. *Engine damage to a NASA DC-8-72 airplane from a high-altitude encounter with a diffuse volcanic ash cloud*, National Aeronautics and Space Administration, Dryden Flight Research Center.
- GRUMKOWSKI, M. 19 Dec 2104 2014. *RE: Discussion concerning installation cost of bizjet FLIR*. Type to MATLON, B.
- GUFFANTI, M., CASADEVALL, T. J. & BUDDING, K. 2010. *Encounters of aircraft with volcanic ash clouds: A compilation of known incidents, 1953-2009* [Online]. USGS. Available: <http://pubs.usgs.gov/ds/545/DS545.pdf>.
- HARPER, W. R. 1967. *Contact and frictional electrification*, Laplacian Press.
- HARPER, W. R. 1970. Triboelectrification. *Physics Education*, 5, 87.
- HUFFORD, G. L., SALINAS, L. J., SIMPSON, J. J., BARSKE, E. G. & PIERI, D. C. 1999. Operational implications of airborne volcanic ash. *Bulletin of the American Meteorological Society*, 81, 745-755.
- ILLINGWORTH, A. J. 1984. A laboratory study of aircraft precipitation static charging. Manchester, UK: The University of Manchester Institute of Science and Technology.
- INTERNATIONAL CIVIL AVIATION ORGANISATION 2010. Volcanic Ash Contingency Plan - EUR and NAT regions. *In: EUR/NAT OFFICE (ed.)*. Paris, France: International Civil Aviation Organisation.
- INTERNATIONAL CIVIL AVIATION ORGANISATION 2012. Fourth Meeting of the International Volcanic Ash Task Force (IVATF/4). Montréal, Canada: ICAO.
- IVLEVA, N. P., HUCKELE, S., WEINZIERL, B., NIESSNER, R., HAISCH, C. & BAUMANN, T. 2013. Identification and characterization of individual airborne volcanic ash particles by Raman microspectroscopy. *Analytical and bioanalytical chemistry*, 405, 9071-9084.
- IZBEKOV, P. & SHIPMAN, J. 2009. SEM image of an ash particle erupted by Redoubt volcano on March 22, 2009. Image courtesy of the AVO/UAF-GI. *In: ALASKA VOLCANO OBSERVATORY / UNIVERSITY OF ALASKA FAIRBANKS, G. I. (ed.)*. Fairbanks, Alaska.
- JAMES, M. R., LANE, S. J. & GILBERT, J. S. 2000. Volcanic plume electrification: Experimental investigation of a fracture-charging mechanism. *Journal of Geophysical Research*, 105, 16641-16649.
- JIANG, H. 2013.  Key findings on airplane economic life. Seattle, USA: Boeing Commercial Airplanes.

- JOHN, W. 1995. Particle-surface interactions: charge transfer, energy loss, resuspension, and deagglomeration. *Aerosol science and technology*, 23, 2-24.
- JOHN, W., REISCHL, G. & DEVOR, W. 1980. Charge transfer to metal surfaces from bouncing aerosol particles. *Journal of Aerosol Science*, 11, 115-138.
- JOHN, W. & SETHI, V. 1993. Breakup of latex doublets by impaction. *Aerosol science and technology*, 19, 57-68.
- JONASSEN, N. 2002. Electrostatics. 2nd ed. Dordrecht, The Netherlands: Kluwer Academic Publishers.
- KHIBNIK, A., RAJAMANI, R., BRUCE WOOD, C., AGRAWAL, R. & DONAT, W. 2013. *IDMS signal processing to distinguish inlet particulates*. USA patent application 13/168293.
- KITE-POWELL, H. L. 2001. Benefits of NPOESS for commercial aviation- volcanic ash avoidance. USA: Woods Hole Oceanographic Institution.
- MALTON, B. 2013. The consideration of applying the measurement of electrostatic charging to determine the ambient suspended volcanic ash concentration as an on-board aircraft detection system. Unpublished BSc dissertation: Lancaster University
- MALVERN INSTRUMENTS LTD 1999. MS2000 Operators Guide. *Malvern Instruments*. 2nd ed. Malvern, UK.: Malvern Instruments.
- MARENCO, F., JOHNSON, B., TURNBULL, K., NEWMAN, S., JIM, H., WEBSTER, H. & RICKETTS, H. 2011. Airborne lidar observations of the 2010 Eyjafjallajökull volcanic ash plume. *Journal of Geophysical Research*, 116, 15.
- MATSUSAKA, S., MARUYAMA, H., MATSUYAMA, T. & GHADIRI, M. 2010. Triboelectric charging of powders: A review. *Chemical Engineering Science*, 65, 5781-5807.
- MATSUYAMA, T. & YAMAMOTO, H. 1994. Charge transfer between a polymer particle and a metal plate due to impact. *Industry Applications, IEEE Transactions on*, 30, 602-607.
- MATSUYAMA, T. & YAMAMOTO, H. 1997. Charge-relaxation process dominates contact charging of a particle in atmospheric condition: II. The general model. *Journal of Physics D: Applied Physics*, 30, 2170.
- NEAL, C. A., CASADEVALL, T. J., MILLER, T. P., HENDLEY II, J. W. & STAUFFER, P. H. 1997. *Volcanic Ash—Danger to Aircraft in the North Pacific, U.S. Geological Survey Fact Sheet 030-97* [Online]. Anchorage Alaska: Alaska Volcano Observatory. Available: http://www.avo.alaska.edu/pdfs/usgsfs030_97_ash.pdf [Accessed 17th March 2013 2013].
- NICARNICA AS. 2013. *AVOID - Airborne Volcanic Object Infrared Detector* [Online]. Kjeller, Norway: Nicarnica. Available: <http://nicarnicaaviation.com/technology/avoid/> [Accessed 15 Dec 2014 2014].
- NICHOLLS, J. R., NDAMKA, N. & WELLMAN, R. G. 2013. Erosion of compressor materials due to volcanic ash ingestion. Aviation safety in volcanic ash clouds: progress since E15, 14 Nov 2013 2013 BAe System, Bristol, UK. Institution of Mechanical Engineers.
- PERGOLA, N., TRAMUTOLI, V., MARCHESE, F., SCAFFIDI, I. & LACAVA, T. 2004. Improving volcanic ash cloud detection by a robust satellite technique. *Remote Sensing of Environment*, 90, 1-22.

- POTTERS BEADS LLC. 2011. *Glass Bead Facts* [Online]. Malvern, PA, USA: Potters Beads LLC. Available: <http://www.pottersbeads.com/egm/NorthAmerica/Products/SolidGlassMicrospheres/BALLOTINImpactbeads/GlassBeadFacts.aspx> [Accessed 28 Dec 2014 2014].
- POWRIE, H. & NOVIS, A. Gas path debris monitoring for F-35 joint strike fighter propulsion system PHM. Aerospace Conference, 2006 IEEE, 2006. IEEE, 8 pp.
- PRATA, A. J. 2008. Satellite detection of hazardous volcanic clouds and the risk to global air traffic. *Natural Hazards*, 51, 303-324.
- PRATA, A. J. & BARTON, I. J. 1997. For monitoring infrared radiation. Google Patents.
- RAYMETRICS S. A. 2014. *Raman Depolarization LIDAR* [Online]. Athens, Greece: Raymetrics S. A.,. Available: <http://www.raymetrics.com/#!/raman-depolarization-lidar/c11a5> [Accessed 19 Dec 2014 2014].
- RENVIER, J. 25 Nov 2010 2010. *RE: Re. Request for information*. Type to MALTON, B.
- ROBINSON, R. 2007. *Airborne Differential Absorption Lidar* [Online]. Tedington UK: National Physical Laboratory. Available: <http://www.npl.co.uk/environmental-measurement/research/airborne-differential-absorption-lidar> [Accessed 19 Dec 2014 2014].
- SAMIMI, A., GHADIRI, M., BOEREFIJN, R., GROOT, A. & KOHLUS, R. 2003. Effect of structural characteristics on impact breakage of agglomerates. *Powder Technology*, 130, 428-435.
- SIMPSON, J. J., HUFFORD, G., PIERI, D. & BERG, J. 2000. Failures in detecting volcanic ash from a satellite-based technique. *Remote Sensing of Environment*, 72, 191-217.
- STERNOVSKY, Z., ROBERTSON, S., SICKAFOOSE, A., COLWELL, J. & HORÁNYI, M. 2002. Contact charging of lunar and Martian dust simulants. *Journal of Geophysical Research: Planets*, 107, 5105.
- TAKANO, T., MAEDA, T., MIKI, Y., AKATSUKA, S., HATTORI, K., NISHIHASHI, M., KAIDA, D. & HIRANO, T. 2013. Detection of microwave emission due to rock fracture as a new tool for geophysics: A field test at a volcano in Miyake Island, Japan. *Journal of Applied Geophysics*, 94, 1-14.
- THE UNIVERISTY OF AUKLAND. 2014. *Scanning Electron Microscope (SEM)* [Online]. Auckland NZ: The Univeristy of Auckland. Available: <http://www.engineering.auckland.ac.nz/en/about/our-research/iande-research-theme/turbidity-current-processes.html> [Accessed 01 Jan 2015 2014].
- TILLOTSON, B. J. 2013. *Detecting volcanic ash in jet engine exhaust*. USA patent application 13/270,286.
- TILLOTSON, B. J. 2014. *Volcanic Assh detection by optical backscatter using standard aircraft lights*. USA patent application 12/949,873.
- TRIGWELL, S., CAPTAIN, J. G., ARENS, E. E., QUINN, J. W. & CALLE, C. I. 2009. The Use of Tribocharging in the Electrostatic Beneficiation of Lunar Simulant. *Industry Applications, IEEE Transactions on*, 45, 1060-1067.
- TUPPER, A., CARN, S., DAVEY, J., KAMADA, Y., POTTS, R., PRATA, F. & TOKUNO, M. 2004. An evaluation of volcanic cloud detection techniques

during recent significant eruptions in the western 'Ring of Fire'. *Remote Sensing of Environment*, 91, 27-46.

- UK CAA. 2014. *All Weather Operations - Application and guidance information associated with All Weather Operations (AWOPS)* [Online]. London UK: UK CAA. Available:
<http://www.caa.co.uk/default.aspx?catid=1428&pagetype=90&pageid=8196> [Accessed 20 Dec 2014 2014].
- UK MET OFFICE. 2014. *Volcanic ash - getting a clearer picture* [Online]. London UK: UK Met Office. Available:
<http://www.metoffice.gov.uk/news/releases/archive/2014/zeus> [Accessed 5 Dec 2014 2014].
- WEINZIERL, B., SAUER, D., MINIKIN, A., REITEBUCH, O., DAHLKÖTTER, F., MAYER, B., EMDE, C., TEGEN, I., GASTEIGER, J., PETZOLD, A., VEIRA, A., KUEPPERS, U. & SCHUMANN, U. 2012. On the visibility of airborne volcanic ash and mineral dust from the pilot's perspective in flight. *Physics and Chemistry of the Earth, Parts A/B/C*, 45–46, 87-102.
- WELLAND, M. E., AZIZ, A. & GANNEY, I. J. 2013. *Sensing systems*. UK patent application PCT/GB2012/051890.
- WIKIPEDIA. 2014. *British Airways* [Online]. Wikipedia. Available:
http://en.wikipedia.org/wiki/British_Airways [Accessed 20 Dec 2014 2014].
- WILLIAMS, K. 2010. *British Airways 2009/10 Annual report and accounts* [Online]. London, UK: British Airways. Available:
http://www.britishairways.com/cms/global/microsites/ba_reports0910/overview/cfo4.html [Accessed 20 Dec 2014 2014].
- WOOD, S. E., BAKER, M. B. & SWANSON, B. D. 2002. Instrument for studies of homogeneous and heterogeneous ice nucleation in free-falling supercooled water droplets. *Review of Scientific Instruments*, 73, 3988.
- WOOLLEY, A., MOBBS, S. & HAYWOOD, J. M. 2013. *Aerosol detection*. USA patent application 13/821,873.
- XIE, Y., RAGHAVAN, V. & RANGWALA, A. S. 2011. Naturally entraining solid particle injector. *Powder Technology*, 213, 199-201.